



Evaluation atraumatique de modèles murins de maladies musculaires génétiques

Aurea Beatriz Martins Martins Bach

► To cite this version:

Aurea Beatriz Martins Martins Bach. Evaluation atraumatique de modèles murins de maladies musculaires génétiques. Medical Physics [physics.med-ph]. Université Paris Sud - Paris XI; Universidade de São Paulo (Brésil), 2015. English. NNT : 2015PA112064 . tel-01166034

HAL Id: tel-01166034

<https://theses.hal.science/tel-01166034>

Submitted on 22 Jun 2015

HAL is a multi-disciplinary open access archive for the deposit and dissemination of scientific research documents, whether they are published or not. The documents may come from teaching and research institutions in France or abroad, or from public or private research centers.

L'archive ouverte pluridisciplinaire **HAL**, est destinée au dépôt et à la diffusion de documents scientifiques de niveau recherche, publiés ou non, émanant des établissements d'enseignement et de recherche français ou étrangers, des laboratoires publics ou privés.



Comprendre le monde,
construire l'avenir®



UNIVERSITE PARIS-SUD

ÉCOLE DOCTORALE : STITS

Laboratoire de Résonance Magnétique Nucléaire
DISCIPLINE PHYSIQUE

THÈSE DE DOCTORAT

préparée en co-tutelle avec l'Universidade de São Paulo

soutenue le 12 / 05 /2015

par

Aurea Beatriz MARTINS BACH

Non-invasive evaluation of murine models for genetic muscle diseases

Directeurs de thèse : Pierre G. CARLIER
Mariz VAINZOF

Directeur de Recherche - NMR Laboratory AIM-CEA
Professor - Universidade de São Paulo

Composition du jury :

Président du jury : Edson AMARO JR

Professor - Universidade de São Paulo

Rapporteurs : Jeanine J. PROMPERS
Luciene COVOLAN

Professor - Eindhoven University of Technology
Professor - Universidade Federal de São Paulo

Examineurs : Edson AMARO JR
Emmanuel DURAND

Professor - Universidade de São Paulo
Professor - Université Paris Sud



Aurea Beatriz MARTINS BACH

Non-invasive evaluation of murine models for genetic muscle diseases

Universidade de São Paulo · Université Paris-Sud

São Paulo

2015

Aurea Beatriz MARTINS BACH

Non-invasive evaluation of murine models for genetic muscle diseases

Avaliação não invasiva de modelos murinos para doenças musculares
genéticas

Evaluation atraumatique de modèles murins de maladies musculaires
génétiques

Tese apresentada ao Instituto de Biociências
da Universidade de São Paulo, para a obtenção
de Título de Doutor em Ciências, Programa:
Ciências Biológicas (Biologia Genética) –
Área de Concentração: Biologia (Genética).
Doutorado realizado em co-tutela
internacional com Université Paris-Sud,
França.

Orientadores: Mariz Vainzof
Pierre Carlier

São Paulo

2015

Ficha Catalográfica

Martins-Bach, Aurea Beatriz
Non-invasive evaluation of murine
models for genetic muscle diseases
Número de páginas 176

Tese (Doutorado) - Instituto de
Biociências da Universidade de São Paulo.
Departamento de Genética e Biologia
Evolutiva, em co-tutela internacional com
Université Paris-Sud, França.

1. NMR 2. Muscle dystrophy 3.
Congenital myopahty 4. Murine models
I. Universidade de São Paulo. Instituto de
Biociências. Departamento de Genética e
Biologia Evolutiva.

Comissão Julgadora:

Dr. Edson AMARO JR.

Presidente da Banca Examinadora

Dr. Emmanuel Durand

Avaliador

Dra. Jeanine PROMPERS

Revisora da tese

Dra. Luciene COVOLAN

Revisora da tese

Dr(a). Mariz Vainzof

Orientadora

Dr. Pierre CARLIER

Orientador

Acknowledgements

I would like to express my sincere appreciation and gratitude to my supervisors in both sides of the Atlantic Ocean, Dr. Mariz Vainzof and Dr. Pierre Carlier. Thank you both for the scientific guidance, for all the confidence you deposited in me, for the patience, knowledge, enthusiasm, exigency, and for the examples of posture face to life and science I could learn with you.

A special thanks to Béatrice Matot for the all time support: her friendship, patience, endeavor, criticisms, suggestions and happiness are invaluable. I must also thank to Claire Wary, for the immense knowledge and countless lessons you transmitted, with your solid example of professional and person.

I would like to thank those who opened their labs for collaboration: Dr. Marc Bitoun, Dr. Alberto Tannús, Dr. Edson Amaro and Dr. Alberto Ribeiro, thank you for all the scientific and technical support you made available. Thanks also to those from these laboratories, who were always so receptive and helpful, in special: Jackeline Malheiros, Waldir Caldeira, Khallil Chaim and Maria Concepcion Otaduy.

My sincere thanks to Claire Latroche and Gregory Jouvion, for the collaboration and results shared, but also for the patience, character and incomparable good mood.

In both laboratories, I could experience friendly and cheerfull conviviality. I thank to all my colleagues in Brazil and France, for all the help, the stimulating discussions, and for all the fun we have had in the last years. A special thanks to Antonio Ribeiro Fernandes, for the dedicated help; to Noura Azzabou, Ericky Caldas, Paula Onofre-Oliveira, André dos Santos, Camila Almeida, Renata Ishiba, Poliana Martins, Luciane Capelo and Simone Ferreira for the scientific support, discussions and friendship; and to Marta Canovas and Leticia Nogueira Feitosa for the meticulous work and all your help.

My sincere acknowledgements to all those who were present and guided me in the non-conventional administrative issues we faced in this joint-supervision thesis. In special, I would like to thank Julie Vandenheede, Laurence Stephen and Erika Harumi Takamoto, for the limitless patience and for the sympathy always present.

Thanks to the Human Genome Research Center and the Institute of Myology for providing all the support needed for doing this thesis. My acknowledgements to CNPq, CAPES, COFECUB and FAPESP for the financial support.

I must express all my gratitude to my family and friends, for the incentive, the patience with my absence and all the love.

Finally, my deepest thanks to Eduardo, my partner for all moments, always there to support me and to make me grow up. Thank you for sharing with me this and all the achievements and challenges we have faced together.

Summary

ABSTRACT	11
RESUMO	13
RESUME	15
GENERAL INTRODUCTION	18
LIST OF PUBLICATIONS	24
CHAPTER 1. BIBLIOGRAPHIC REVIEW: NON-INVASIVE STUDY OF GENETIC MUSCLE DISORDERS.....	27
<i>MUSCULAR DYSTROPHIES</i>	<i>27</i>
<i>Vascular alterations in Duchenne muscle dystrophy</i>	<i>30</i>
<i>CONGENITAL MYOPATHIES</i>	<i>33</i>
<i>ANIMAL MODELS FOR GENETIC MUSCLE DISEASES</i>	<i>35</i>
<i>Animal models for Muscular Dystrophies.....</i>	<i>35</i>
<i>Animal models for congenital myopathies</i>	<i>38</i>
<i>NON-INVASIVE EVALUATION OF GENETIC MUSCLE DISEASES</i>	<i>39</i>
<i>NMR IN THE STUDY OF ANIMAL MODELS FOR GENETIC MUSCLE DISEASES</i>	<i>41</i>
CHAPTER 2. QUANTITATIVE T2 COMBINED WITH TEXTURE ANALYSIS OF NUCLEAR MAGNETIC RESONANCE IMAGES IDENTIFY DIFFERENT DEGREES OF MUSCLE INVOLVEMENT IN THREE MOUSE MODELS OF MUSCLE DYSTROPHY: MDX, LARGE^{MYD} AND MDX/LARGE^{MYD}	44
<i>ABSTRACT</i>	<i>45</i>
<i>INTRODUCTION.....</i>	<i>46</i>
<i>MATERIALS AND METHODS</i>	<i>49</i>
<i>Ethics Statement.....</i>	<i>49</i>
<i>Animals</i>	<i>49</i>
<i>Magnetic Resonance Imaging acquisition and analysis</i>	<i>50</i>
<i>Histological analysis.....</i>	<i>51</i>
<i>Statistic analysis.....</i>	<i>52</i>
<i>RESULTS.....</i>	<i>53</i>
<i>Muscle T2.....</i>	<i>54</i>
<i>Muscle texture analysis.....</i>	<i>56</i>
<i>Histological analysis.....</i>	<i>57</i>
<i>DISCUSSION</i>	<i>60</i>
<i>CONCLUSIONS</i>	<i>65</i>
<i>SUPPORTING INFORMATION</i>	<i>66</i>
<i>S2.1. T2 calculation from two images at different echo times</i>	<i>66</i>
<i>S2.2. Features selected for Texture Analysis</i>	<i>67</i>
<i>COMPLEMENTS TO THE MANUSCRIPT.....</i>	<i>68</i>
<i>Validation of the 2 points T2 measurements with a multiecho sequence</i>	<i>68</i>
<i>Post-mortem changes in the T2 values</i>	<i>69</i>
CHAPTER 3. STRUCTURAL AND FUNCTIONAL ALTERATIONS OF SKELETAL MUSCLE MICROVASCULAR NETWORK IN DYSTROPHIN-DEFICIENT MDX MICE.....	72
<i>ABSTRACT</i>	<i>73</i>
<i>INTRODUCTION.....</i>	<i>74</i>
<i>MATERIALS AND METHODS</i>	<i>76</i>
<i>Mice</i>	<i>76</i>

<i>Microvascular network organisation in three dimensions</i>	76
<i>Histology</i>	77
<i>Morphometric analysis</i>	77
<i>Nuclear Magnetic Resonance analysis</i>	78
<i>Statistics</i>	79
RESULTS	80
<i>Normal microvascular network organisation in young-adult Flk1^{GFP/+}:mdx mouse</i>	80
<i>Muscle blood perfusion is modified in young-adult mdx mice</i>	84
<i>Muscle bioenergetics in young-adult mice (Table 3.1)</i>	86
<i>Alteration of microvascular network organisation in old Flk1^{GFP/+}:mdx mouse</i>	88
<i>Alteration of muscle perfusion in old mdx mice</i>	92
<i>Muscle bioenergetics in 12 month-old mice (Table 3.2)</i>	93
DISCUSSION	94
CONCLUSION	98
SUPPLEMENTARY INFORMATION	99
<i>S3.1. Nuclear Magnetic Resonance analysis</i>	99
CHAPTER 4. NON-INVASIVE NMR STUDY OF THE MOUSE MODEL FOR CENTRONUCLEAR MYOPATHY WITH MUTATION IN THE DYNAMIN-2 GENE	103
INTRODUCTION	103
MATERIALS AND METHODS	105
<i>Animals</i>	105
<i>Nuclear Magnetic Resonance (NMR)</i>	105
<i>Data analysis</i>	106
<i>Histological analysis</i>	108
<i>Statistical analysis</i>	108
RESULTS	108
<i>Morphometrical evaluation</i>	108
<i>T1 measurements</i>	110
<i>T2 measurements</i>	111
<i>Histological analysis</i>	113
DISCUSSION	115
CHAPTER 5. PILOT FUNCTIONAL AND METABOLIC EVALUATION OF THE KI-DNM2^{R465W} MICE	119
INTRODUCTION	119
PILOT STUDY 1. EXERCISE AS THE PARADIGM OF MUSCLE STRESS IN KI-DNM2R465W MICE	120
<i>Materials and methods</i>	120
<i>Results</i>	123
<i>Discussion</i>	129
PILOT STUDY 2. PROLONGED ISCHEMIA AS THE PARADIGM OF MUSCLE STRESS	130
<i>Materials and Methods</i>	130
<i>Results</i>	131
<i>Discusssion</i>	134
PILOT STUDY 3. REGENERATION IN THE DNM2 MICE: T1, T2 AND FUNCTIONAL ANALYSIS AFTER INJURY	135
<i>Materials and Methods</i>	135
<i>Results</i>	136
<i>Discussion</i>	140
CHAPTER 6. EVALUATION OF THE POTENTIAL USE OF MICRO-COMPUTED TOMOGRAPHY IN THE STUDY OF MUSCLES FROM MURINE MODELS FOR MUSCLE DYSTROPHIES	142
INTRODUCTION	142
MATERIALS AND METHODS	143
<i>Animals</i>	143
<i>Muscle injury with electroporation</i>	144

<i>Micro-CT</i>	145
<i>Data Analysis</i>	145
<i>Statistical Analysis</i>	146
RESULTS	146
<i>Phenotypical characterization of the dystrophic muscle with micro-CT</i>	146
<i>Evaluation of injured muscle with micro-CT</i>	147
DISCUSSION	148
GENERAL CONCLUSIONS AND PERSPECTIVES	152
BIBLIOGRAPHY	155

Abstract

Non-invasive evaluation of murine models for genetic muscle diseases

Novel therapeutic approaches are being introduced for genetic muscle diseases such as muscle dystrophies and congenital myopathies, all of them having remained without cure so far. These recent developments have motivated a renewed and augmented interest in non-invasive methods for muscle characterization and monitoring, particularly during and after therapeutic intervention. In this context, animal models are essential to better understand the disease mechanisms and to test new therapies. Recently, significant advances in the non-invasive evaluation of mouse models for genetic muscle diseases have been achieved. Nevertheless, there were still several mouse strains not characterized non-invasively, and it was necessary to develop sensitive methods to identify subtle alterations in the murine affected muscle. The purpose of this thesis was to apply non-invasive techniques in the study of murine models for genetic muscle diseases with variable phenotypes. Three mouse models for muscle dystrophy (*mdx*, *Large^{myd}*, *mdx/Large^{myd}*) and one mouse model for congenital myopathy (*KI-Dnm2^{R465W}*) were studied with Nuclear Magnetic Resonance (NMR) methods. Two dystrophic strains (*Large^{myd}*, *mdx/Large^{myd}*) and normal mice after injury were studied through micro-Computed Tomography (micro-CT). On NMR, all affected mouse strains presented increased muscle T2, which could be related to variable features in the histological evaluation, including necrosis and inflammation, but also to clusters of fibers under regeneration or with altered cytoarchitecture. The combination of NMR and texture analyses allowed the unambiguous differential identification of all the dystrophic strains, although it was not feasible when comparing the muscle T2 measurements only. *Mdx* mice showed functional and morphological alterations of vascular network. In the *KI-Dnm2^{R465W}* mice, a pilot study revealed tendencies of functional impairment. Finally, micro-CT images were unable to detect differences in muscle's content in dystrophic mice. Altogether, these results not only increased the number of murine models for genetic muscle diseases non-invasively characterized, it also demonstrated some degree of

specificity of the imaging anomalies, as revealed by texture analysis. It also showed that non-invasive NMR methods can be sensitive enough to identify subtle alterations in murine muscle phenotype, even in early stages. This thesis was developed under an international joint supervision between France and Brazil, and comprised an important transfer of technology, with the first non-invasive studies of murine muscles performed in Brazil.

Resumo

Avaliação não invasiva de modelos murinos para doenças musculares genéticas

Novas abordagens terapêuticas vêm sendo introduzidas para doenças musculares genéticas como distrofias musculares e miopatias congênitas, distúrbios que permanecem sem cura até o momento. Estes recentes avanços motivaram um interesse renovado e crescente por métodos não invasivos para a caracterização e monitoramento do músculo afetado, particularmente durante e após intervenções terapêuticas. Neste contexto, modelos animais são essenciais para uma melhor compreensão dos mecanismos das doenças e para testar novas terapias. Recentemente, avanços significativos na avaliação não invasiva de modelos murinos para doenças musculares genéticas foram alcançados. Entretanto, diversas linhagens de camundongos ainda não foram caracterizadas de maneira não invasiva, e ainda é necessário o desenvolvimento de métodos sensíveis para a identificação precoce de alterações sutis no músculo de camundongos afetados. A proposta desta tese é aplicar técnicas não invasivas inovadoras no estudo do músculo de modelos murinos para doenças musculares genéticas com fenótipos variados. Três modelos murinos para distrofias musculares (*mdx*, *Large^{myd}*, *mdx/Large^{myd}*) e um modelo murino para miopatia congênita (*KI-Dnm2^{R465W}*) foram estudados com métodos de Ressonância Magnética Nuclear (RMN). Duas linhagens distróficas (*Large^{myd}*, *mdx/Large^{myd}*) e camundongos normais após injúria foram estudados através de micro-Tomografia Computadorizada (micro-CT). Em RMN, todas as linhagens de camundongos afetados apresentaram aumento de T2 muscular, o que foi relacionado a diversas anomalias na análise histológica, como necrose e inflamação, mas também a conjuntos de fibras em regeneração ou a fibras com citoarquitetura alterada. A combinação de RMN com análise de textura permitiu a identificação não ambígua de todas as linhagens distróficas, sendo que apenas a comparação dos valores de T2 muscular não permitiu esta diferenciação. Camundongos *mdx* mostraram alterações funcionais e morfológicas na rede vascular do músculo. Estudo piloto em camundongos *KI-Dnm2^{R465W}* revelou tendências de comprometimento da função

muscular. Por fim, imagens de micro-CT não permitiram a detecção de diferenças na composição muscular em camundongos distróficos. Este conjunto de resultados não apenas enriquece o painel de modelos murinos para doenças musculares genéticas caracterizados de maneira não invasiva, mas também demonstra um certo grau de especificidade nas anomalias observadas nas imagens, como revelado pela análise de textura. Estes resultados também mostraram que métodos não invasivos de RMN podem ser suficientemente sensíveis para identificar alterações sutis no fenótipo muscular murino, mesmo em estágios precoces. Esta tese foi desenvolvida sob acordo de co-tutela internacional entre a França e o Brasil, e compreendeu uma importante transferência de conhecimento, com os primeiros estudos não invasivos de músculo murino realizados no Brasil.

Résumé

Evaluation atraumatique de modèles murins de maladies musculaires génétiques

De nouvelles options thérapeutiques sont en cours d'introduction pour les maladies musculaires génétiques telles que les dystrophies musculaires et les myopathies congénitales, maladies jusque là sans traitement causal. Ces développements récents ont suscité un intérêt renouvelé et croissant pour les méthodes atraumatiques en vue de caractériser et de suivre les muscles atteints, en particulier pendant et après une intervention thérapeutique. Dans ce contexte, les modèles animaux sont essentiels pour mieux comprendre les mécanismes des maladies et pour tester des nouvelles thérapies. Récemment, il y a eu des avancées significatives dans l'évaluation atraumatique de modèles murins de maladies musculaires génétiques. Néanmoins, nombre de lignées de souris n'ont pas encore été caractérisées de façon atraumatique et il reste à mettre au point des méthodes plus sensibles pour identifier précocement des altérations subtiles dans le muscle des souris malades. L'objectif de cette thèse est d'appliquer des techniques atraumatiques innovantes à l'étude du muscle de modèles murins de maladies musculaires génétiques avec des phénotypes variés. Trois lignées de souris modèles de dystrophies musculaires (*mdx*, *Large^{myd}* et *mdx/Large^{myd}*) et une lignée de souris modèle de la myopathie congénitale (*KI-Dnm2^{R465W}*) ont été étudiées par des méthodes de Résonance Magnétique Nucléaire (RMN). Deux lignées dystrophiques (*Large^{myd}* et *mdx/Large^{myd}*) plus des souris normaux après une blessure ont été étudiées par microtomographie (micro-CT). En RMN, toutes les souches de souris affectées ont présenté un T2 musculaire augmenté, en relation avec une gamme d'anomalies histologiques, y comprises nécrose et inflammation, mais aussi des groupes de fibres en régénération ou des fibres avec altérations de l'architecture. Avec la combinaison de la RMN et de l'analyse de la texture, il a été possible d'identifier sans ambiguïté toutes les lignées dystrophiques, alors que la seule mesure du T2 ne permettait pas de les différencier. Les souris *mdx* ont présenté des altérations fonctionnelles et morphologiques du réseau vasculaire musculaire. Pour les souris *KI-Dnm2^{R465W}*, des études préliminaires ont révélé une tendance à développer des altérations fonctionnelles musculaires.

Finalement, les images de micro-CT n'ont pas pu détecter des différences du contenu musculaire dans les souris dystrophiques. L'ensemble des résultats non seulement enrichit le panel de modèles murins de maladies génétiques musculaires caractérisés de manière atraumatique, il révèle également un certain degré de spécificité des anomalies dans l'imagerie, comme l'a montré l'analyse de texture. Les résultats démontrent aussi que des méthodes de RMN non-invasives peuvent être assez sensibles pour identifier des altérations subtiles dans le phénotype musculaire murin, même à des stades précoces. Cette thèse a été développée dans le cadre d'une co-tutelle internationale entre la France et le Brésil, et elle a comporté un important transfert de compétence, qui a permis de réaliser les premières explorations atraumatiques du muscle murin effectuées au Brésil.

General Introduction

General Introduction

Muscles are contractile organs essential for life, being responsible for functions such as breathing, locomotion (skeletal muscles), blood circulation (cardiac/smooth muscle) and food propulsion in the digestive system (smooth muscle). Only skeletal muscles are under voluntary control, and attached to bones they compose the locomotor system.

Muscle dysfunctions can be caused by influences like injury, cancer and infections, but can also be originated by genetic defects. Among the genetic disorders affecting primarily skeletal muscles, there are the muscle dystrophies and the congenital myopathies. Muscle dystrophies are caused by alterations in proteins present at the sarcolemma, the sarcoplasm, the basal lamina and even at the nucleus of muscle cells. Muscle dystrophy patients have progressive loss of muscle cells, with consequent weakness. The histopathological pattern includes variation in fiber size, necrosis, infiltration by inflammatory cells, and substitution by connective and adipose tissue (Emery, 2002). Congenital myopathies are caused by alterations in proteins from the contractile filaments, the sarcolemma or the sarcoplasm. Patients with congenital myopathies present weakness generally at birth, and disease progress is less accentuated than in muscle dystrophies. Histopathological analysis of myopathic muscles shows structural alterations such as the presence of rods, cores, or altered positioning of nucleus and other organelles (Nance et al., 2012). There is no cure for genetic muscle diseases, but several therapeutic protocols are in development, from pharmacological to cellular and genetic approaches.

Animal models for genetic muscle disorders play a crucial role in studies aiming to understand genetic, clinical and histopathological processes related to the disease, and are necessary also to test therapeutic protocols. Several animals with molecular, clinical or histological alterations similar to those observed in patients have been identified in nature or generated in laboratory. There are models for muscular diseases from different species, like dogs, cats, hamsters, fishes and pigs, but the murine models are the most commonly studied (Vainzof et al., 2008).

Clinical evaluation, muscle proteins dosage in blood, electromyography, genetic studies and muscle biopsy are the most frequent procedures in diagnostic and follow up of muscle diseases. Imaging methods, including computed tomography (CT), ultrasound, radioisotopes based methods (scintigraphy, PET and SPECT) and nuclear magnetic resonance (NMR), are gaining space on the muscle diseases field. Among them, NMR has optimum qualities for soft tissue evaluation, allowing the tri-dimensional visualization of deep structures without involving the use of ionizing radiation. CT images can also be used for the evaluation of patients with muscle diseases, but with less contrast for soft tissues than NMR, and with the use of ionizing radiation (Mercuri et al., 2007).

NMR allows image acquisition with different contrasts: T1, T2 and proton density weighted images can give different information about the same anatomical region. Apart of the morphological information, NMR allows metabolic and functional measurements. NMR spectroscopy gives information about the chemical composition of the tissue. ^1H and ^{31}P are the most common nuclei for *in vivo* spectroscopy studies, but different atomic nuclei can be evaluated (^{19}P , ^{13}C , ^{23}Na , ^{15}N , etc). ^{31}P spectroscopy allows the evaluation of tissue pH and of phosphate molecules, being particularly interesting to study the energetic metabolism. ^1H spectroscopy can give information about metabolites such as lactate, creatine and lipids. Finally, functional NMR can give information about muscle blood perfusion and oxygen consumption, for example.

In the literature, NMR has been used to evaluate dystrophic patients' muscles (Finanger et al., 2012; Mercuri et al., 2007; Poliachik et al., 2012), heart (Verhaert et al., 2011) and brain (Rae et al., 1998; Razek et al., 2009), with morphological, functional and metabolic analysis. Patients with non dystrophic congenital myopathies have been also evaluated by NMR (Jungbluth et al., 2008; Quijano-Roy et al., 2011), in studies specially focused on morphological alterations such as muscle atrophy and fat replacement. The study of different genetic muscle diseases by CT and NMR images allowed the identification of unique patterns of muscle involvement depending on the primary mutation (Wattjes et al., 2010).

NMR studies from animal models for neuromuscular diseases face the challenge of reducing scale: it is necessary to increase the spatial resolution,

especially when considering mice, the most frequent animal for modeling genetic diseases. Despite of it, there is already a considerable amount of NMR data of animal models for neuromuscular disorders. The *mdx* mouse, model of the most frequent muscle dystrophy, Duchenne Muscular Dystrophy (DMD), has been exhaustively studied by NMR. Muscle morphology and metabolism were evaluated in *mdx* mouse by *in vivo*, *ex vivo* and *in vitro* MR imaging and spectroscopy (Amthor et al., 2004; Dunn and Zaim-Wadghiri, 1999; Dunn et al., 1991; Griffin et al., 2001; Heier et al., 2014; Mathur et al., 2011; McIntosh et al., 1998a, 1998b; Pratt et al., 2013; Straub et al., 2000; Walter et al., 2005).

In a less extensive amount, different mouse models for muscle dystrophies were studied by NMR (Cole et al., 2002; Pacak et al., 2007; Schmidt et al., 2009; Tardif-de Géry et al., 2000; Walter et al., 2005), as the golden retriever muscular dystrophy dog (Claire et al., 2012; Fan et al., 2014; Thibaud et al., 2007, 2012; Yokota et al., 2009). In addition to the variable NMR methods capable to identify changes in the affected muscles, the use of mathematical tools for image texture analysis is gaining space, since it can identify subtle differences in the pattern of distribution of muscle lesions (Mahmoud-Ghoneim et al., 2006; Nketiah et al., 2014; Pratt et al., 2013; Škoch et al., 2004; Wang et al., 2013). A deeper bibliographic review of genetic muscle disorders and non-invasive muscle evaluation, for both human patients and animal models, is presented in **Chapter 1**.

Even with an increasing amount of noninvasive data showing differences between affected and normal mice, the use of NMR as an outcome measure depends on the reliability of the technique to track also subtle differences in the muscles. In this context, the **Chapter 2** of this thesis aims to evaluate the potential of combining NMR and texture analysis in the comparison of dystrophic muscles under different gene mutations. Three mouse models for muscle dystrophies, covering a wide range of phenotypes, were evaluated by NMR T2 relaxometry: the *mdx* mouse, with a mild phenotype; the *Large^{myd}* mouse, model of the congenital muscular dystrophy 1D, with altered glycosylation of the protein alpha-dystroglycan; and the recently generated double mutant *mdx/Large^{myd}* mouse, with both mutations and a very severe phenotype (Martins et al., 2013).

It is known that the dystrophic muscle presents microvascular alteration both in patients (Leinonen et al., 1979), dogs (Nguyen et al., 2005) and mice (Bagher et al., 2011; Burch et al., 1981; Palladino et al., 2013). How these microvascular alterations affect the muscle metabolism and function *in vivo* is yet unexplored. The **Chapter 3** of this thesis aims to evaluate *in vivo* the possible functional and metabolic effects of the microvascular alterations in the mdx mouse muscle. A multimodal approach was used to allow simultaneous measures of muscle perfusion and ³¹P spectroscopy for the energetic metabolism inference after hypoxic stress. Hypothetical functional or metabolic alterations would take place before muscle degeneration and substitution by connective and adipose tissues, being possible early markers of the disease, and possibly helping to elucidate the mechanisms of the disease.

While dystrophic muscles are characterized by tissue alterations, including inflammation, necrosis, and infiltration by adipose and by connective tissue, congenital myopathies are characterized by structural and functional alterations inside the muscle fibers, which are followed by metabolic and/or functional impairment. The versatility of NMR measures can be helpful in the observation of the impact of these alterations in myopathic muscles.

Animal models for congenital myopathies have been identified in dogs (Beggs et al., 2010; Pelé et al., 2005) and engineered in mice (Buj-Bello et al., 2002; Durieux et al., 2010; Ottenheijm et al., 2013; Pierson et al., 2012; Ravenscroft et al., 2011). Gineste and collaborators published in 2013 three papers characterizing different murine models for nemaline myopathy with noninvasive methods, including NMR (Gineste et al., 2013a, 2013b, 2013c). To our knowledge, these are the only NMR descriptions of myopathic alterations in murine models of congenital myopathies. The **Chapter 4** of this thesis aims to describe with *in vivo* NMR the *KI-Dnm2^{R465W}* mouse, model of autosomal dominant centronuclear myopathy. This murine model presents the most frequent mutation in the dynamin-2 gene in centronuclear myopathy patients. Its phenotype includes muscle weakness, atrophy, and the presence of histological features observed in patients, like the concentration of oxidative activity at the center of the muscle fibers (Durieux et al., 2010). Nevertheless, the high percentage of centronucleated fibers observed in patients is not present on the mouse model. In these mice, it is not observed infiltration by connective or adipose tissue in the

muscle, nor signals of inflammation or necrosis. In the search of additive information about the muscle commitment in this disease, *in vivo* morphological and relaxometry measures were acquired in this mouse model at two different ages, 3 and 6 months. Additionally, **Chapter 5** describes pilot functional and metabolic studies with this mouse model, for the phenotypical characterization and for an initial evaluation of the regeneration process after acute injury. *In vivo* multiparametric functional NMR, with measurements of muscle blood perfusion, oxygen consumption and energetic metabolism, were carried out.

CT images from patients with muscle diseases can also reveal morphological alterations such as muscle atrophy and fat infiltration (Nakayama et al., 2013a). The muscular X-ray attenuation is reduced in patients with muscle dystrophies (Rickards et al., 1982; Swash et al., 1995), while it is not affected by bed rest (Rittweger et al., 2013), indicating that alterations in the muscle content, like fibrotic or adipose infiltration, would affect its radiodensity. In the recent years, with the development of micro-CT equipments with micrometric resolution, the number of *in vivo* micro-CT studies with small animals has increased. Nevertheless, the great majority of them are focused on skeletal alterations (Gray et al., 2012; Manske et al., 2012), including studies on dystrophic mice bones (Novotny et al., 2011, 2012). In the literature, there are essays involving micro-ct studies of mouse heart (Detombe et al., 2012), lungs (Lederlin et al., 2012; Paik et al., 2014), and even muscles (Manske et al., 2010; Weber et al., 2012). Nevertheless, these micro-CT muscle studies are focused on muscle volume changes. The possible radiodensity alterations on dystrophic muscle from mouse models are still unknown. In this context, the major objective of **Chapter 6** of this thesis is the evaluation of the potential use of X-ray micro tomography in the study of dystrophic muscle. The severe dystrophic mouse model *mdx/Large^{myd}* and the parental lineage *Large^{myd}* were selected for this essay due to the progressive muscle degeneration and the intense infiltration of the muscle by connective tissue.

List of Publications

List of Publications

Publications in international journals

- Latroche C, Matot B, Martins-Bach A, Briand D, Chazaud B, Wary C, Carlier P, Chrétien F, Jouvion G. Structural and functional alterations of skeletal muscle microvascular network in dystrophin-deficient mdx mice. *The American Journal of Pathology*. In press (2015).
- Martins-Bach AB, Malheiros J, Matot B, Martins PCM, Almeida CF, Caldeira W, Ribeiro AF, Loureiro de Sousa P, Azzabou N, Tannús A, Carlier PG, Vainzof M (2015). Quantitative T2 combined with Texture Analysis of Nuclear Magnetic Resonance Images identify different degrees of muscle involvement in three mouse models of muscle dystrophy: mdx, Largemyd and mdx/Largemyd. *Plos One*; 24; 10(2):e0117835.
- Zatz M, Vieira NM, Zucconi E, Pelatti M, Gomes J, Vainzof M, Martins-Bach A, Garcia Otaduy MC, Bento dos Santos G, Amaro Jr. E, Landini V, Gomes T (2015). Case Report: A normal life without muscle dystrophin. *Neuromuscular Disorders*; 25(5):371-4.
- Martins PCM, Ayub-Guerrieri D, Martins-Bach AB, Onofre-Oliveira P, Malheiros JM, Tannus A, de Sousa PL, Carlier PG, Vainzof M (2013). Dmdmdx/Largemyd: a new mouse model of neuromuscular diseases useful for studying physiopathological mechanisms and testing therapies. *Dis Model Mech*; 6(5):1167-74.
- Martins-Bach AB, Bloise AC., Vainzof M, Rabbani SR (2012). Metabolic profile of dystrophic mdx mouse muscles analyzed with in vitro magnetic resonance spectroscopy (MRS). *Magnetic resonance imaging*, 30(8), 1167-1176.

Written communications in international congresses

- M. Vainzof, C.F. Almeida, R. Ishiba, A. Martins-Bach, A.L.F. Santos, L. Nogueira (2014). 2871T. Using electroporation as a model of degeneration/regeneration to investigate the regenerative potential in neuromuscular disorders (NMD). 64 th Annual Meeting of the American Society of Human Genetics, 2014, San Diego, CA, United States.
- Martins-Bach AB, Malheiros J, Melo Machado PC, Almeida CF, Matot B, de Sousa PL, Tannús A, Carlier PG, Vainzof M (2013). P.1.18 NMR imaging comparison of dystrophic mouse models: mdx, Large, mdx/Large. 18th International Congress of the World Muscle Society, 2013, Asilomar, CA, United States. *Neuromuscular Disorders*, 23(9), 747.
- Vainzof M, Calyjur P, Otaduy MCG, Almeida CF, Martins-Bach A, Carlier RY, Gurgel-Giannetti J, Amaro E, Carlier PG (2013). P.4.5 Muscle NMR imaging in the rare E650K mutation in the DNM2 gene in a centronuclear myopathy patient. 17th International Congress of the World Muscle Society, 2013, Perth, Western Australia. *Neuromuscular Disorders*, 23(9), 761.
- Matot B, Jouvion G, Martins-Bach AB, Wary C, Carlier PG (2012). D.P. 16 Metabolic and hemodynamic alterations in the mdx skeletal muscle revisited using multi-parametric functional NMR. 17th International Congress of the World Muscle Society, 2013, Perth, Western Australia. *Neuromuscular Disorders*, 22(9), 822-823.
- Martins-Bach AB, Bloise AC, Rabbani SR, Vainzof M (2011). P.1.45 Application of NMR spectroscopy in the study of mdx mouse. 16th International Congress of the World Muscle Society, 2011, Algarve, Portugal. *Neuromuscular Disorders*, 21(9), 655.

Chapter 1

Bibliographic Review: Non-invasive study of genetic muscle disorders

Chapter 1. Bibliographic Review: Non-invasive study of genetic muscle disorders

Muscular Dystrophies

Muscular dystrophies are an extensive group of progressive genetic diseases where skeletal muscles are primarily affected. Mutations in genes coding for sarcomeric, sarcolemmal, sarcoplasmatic/cytosolic, nuclear or extracellular matrix proteins can cause muscular dystrophies. The absence or altered function of one of these proteins is responsible for a cascade of events that ends in muscle fibers degeneration and necrosis, with substitution of muscle by connective and adipose tissue. Histological analysis of dystrophic muscle reveals fibrosis, muscle fiber size variation, internalization of the nuclei, infiltration by inflammatory and adipose cells, necrosis and muscle fiber degeneration (Dubowitz et al., 2013; Shieh, 2013). Patients present progressive weakness, starting at different ages depending on the disease. More than 30 different forms of muscular dystrophy have been described, being divided in three major groups: dystrophinopathies; limb girdle muscular dystrophy (LGMD) and congenital muscular dystrophies (CMD) (Dalkilic and Kunkel, 2003).

Dystrophinopathies are characterized by mutations in the dystrophin gene, located at Xp21 (Hoffman et al., 1987). There are two forms of dystrophinopathies, Duchenne muscular dystrophy (DMD) and Becker muscular dystrophy (BMD). DMD is the most common muscular dystrophy by incidence, affecting up to 1:3000 boys at birth. In DMD, the gene mutation leads to the absence of the protein dystrophin in muscle and to a severe phenotype. In BMD, the dystrophin protein is present but in less quantity and with abnormal function, leading to a milder phenotype (Emery, 2002). In dystrophinopathies, the skeletal muscle is the major impacted tissue, but additional alterations can be present: cardiomyopathy is observed in DMD patients and heterozygous females (Mirabella et al., 1993; Nigro et al., 1990), slower gastric and intestinal flow are present in DMD patients (Borrelli et al., 2005), and more than 30% of DMD patients have cognitive impairment in a variable degree (Bresolin et al., 1994).

Dystrophin is normally expressed not only in skeletal muscle cells, but also in cardiac muscle, central nervous system and smooth muscle cells (Love et al., 1993). In skeletal muscle, the protein dystrophin is located under the sarcolemma, in association with glycosylated proteins, composing the dystrophin-glycoprotein complex (DGC) (Ervasti and Campbell, 1991, 1993). The DGC is responsible for the link between the actin cytoskeleton and the extracellular matrix, acting also on cellular and membrane signaling pathways (Rando, 2001a) and on calcium homeostasis regulation (Gumerson and Michele, 2011). Apart of dystrophin, DGC is composed by the dystroglycan and sarcoglycan complexes, dystrobrevin, syntrophins and sarcospan, which interact with other intra and extracellular proteins (Figure 1.1). Dystrophin interacts by its N-terminal portion with actin filaments in the cytoplasm, while the C-terminal portion interacts with syntrobrevin in the cytoplasm and β -dystroglycan (β -DG) in the sarcolemma. β -DG by its turn is linked to the peripheral membrane protein α -dystroglycan (α -DG), which is responsible for the connection of the DGC with the extracellular matrix protein α -2 laminin. This link occurs through sugar chains in the glycosylated extension of α -DG, with high affinity to Laminin G (LG)-like domains present in various extracellular matrix proteins, such as laminins, perlecan and agrin in muscle, and neuexin in brain (Barresi and Campbell, 2006; Ervasti and Campbell, 1993; Straub and Campbell, 1997).

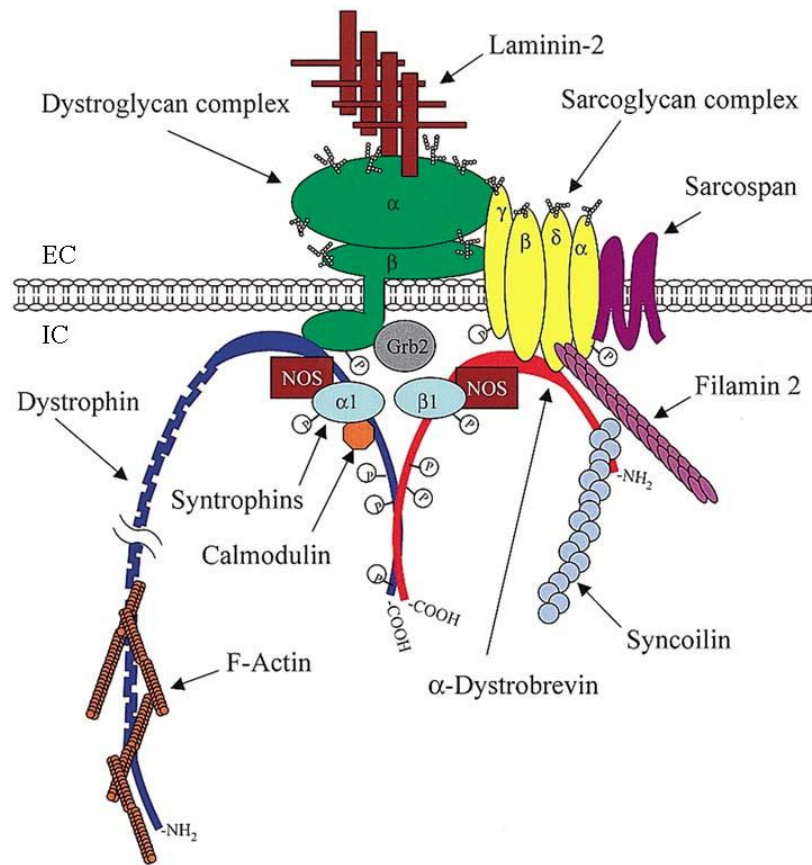


Figure 1.1: Schematic representation of the dystrophin-glycoprotein complex (DGC), showing its components: dystrophin, dystroglycan complex, sarcoglycan complex, α -dystrobrevin, syntrophins and sarcospan. The extracellular (EC) matrix protein laminin-2 binds to the complex through α -dystroglycan, while F-actin, syncoilin and filamin-2 are intracellular (IC) ligands. Calmodulin, Grb2 and nNOS are also associated to the DGC as signaling molecules. The post-traductional modifications are shown: glycosylation in dystroglycans and sarcoglycans, and phosphorylation sites (P) in dystrophin, α -dystrobrevin, β -dystroglycan, syntrophins, α - and γ -sarcoglycans (Rando, 2001a).

Mutations in genes coding for DGC proteins or proteins involved in posttranslational modifications of the DGC components can lead to different forms of muscular dystrophies. Among these, mutations in genes coding for the sarcoglycans are related to LGMD, while alterations in the glycosylation of the protein α -DG are related to LGMD and CMD (Dalkilic and Kunkel, 2003).

LGMDs are the more heterogeneous subgroup of muscular dystrophies, including more than 20 different forms. In LGMD, muscles from pelvic and shoulder girdle are those initially affected. The phenotype is highly variable, from severe forms with early onset and rapid progression, to milder presentations, with first symptoms appearing after the 4th decade of life and with slow progression. LGMDs are classified according to the pattern of inheritance (autosomal dominant or recessive) and the causative genes. Mutations in genes related to LGMD can also cause different diseases, such as myofibrillar myopathy, Miyoshi myopathy and CMD (Mitsuhashi and Kang, 2012).

Patients affected by the third subgroup of muscle dystrophies, CMD, present weakness and hypotonia at birth or in the first months of life. Progressive dystrophic alterations are observed in histological analysis, and patients often show involvement in the brain and other organs. The list of genes associated with CMDs is still expanding, but the great majority of them are related to the interaction of the DCG with the extracellular matrix (Emery, 2002; Mercuri and Muntoni, 2012). This interaction is mediated by the α -DG linkage to the extracellular matrix protein laminin. Posttranslational modifications in these two proteins, specifically glycosylation, are essential to maintain and regulate this link. Mutations in the gene coding for dystroglycans are very rare, but alterations in genes coding for proteins that participate in the glycosylation of α -DG, such as *POMT1*, *POMGnT1*, *FKTN*, *FKRP* and *LARGE*, are related to different forms of LGMD and CMD (Moore and Winder, 2012; Muntoni et al., 2008).

Vascular alterations in Duchenne muscle dystrophy

DMD is the most studied muscle dystrophy, due to the high incidence and severity. The current hypothesis for the pathophysiology of DMD is that the absence of dystrophin fragilizes the sarcoplasm, which would suffer from micro-lesions due to mechanically induced damage from muscle contractions. Sarcoplasm rupture alters calcium homeostasis, which would result in cell death. Satellite cells would try to regenerate the muscle, but after several rounds of degeneration and regeneration, the

satellite cells pool would be exhausted and muscle degeneration would predominate. Processes such as inflammation, fibrosis and impaired vascular adaptation would take place secondarily, even worsening the disease manifestation (Deconinck and Dan, 2007).

Recently, the so-called “two-hit” hypothesis for the disease mechanism in DMD has gained space. According to this hypothesis, dystrophin absence cause not only increased susceptibility to mechanical stress, but also vascular and metabolic alterations that when combined lead to the dystrophic phenotype (Ennen et al., 2013; Rando, 2001b).

Despite of the general lack of dystrophin in the muscle of DMD patients, in initial stages of the disease muscle lesions present in small and random clusters of degenerating fibers, usually surrounded by normal muscle fibers (Engel, 1967; Miike, 1983). This pattern of focal lesions is observed also in healthy muscle when submitted to infarction (Hathaway et al., 1970; Mendell et al., 1971). The hypothesis that muscle vascular insufficiency could be related to the disease manifestation has prompted several studies. In the 70 and 80 decades, optical and electronical microscopy of muscle blood vessels of DMD patients identified only very few nonspecific anomalies. DMD muscle was described as presenting replication of the capillaries’ basement membrane, degenerating and regenerating capillary cells, and platelet aggregation in small blood vessels (Fidziańska et al., 1986; Koehler, 1977; Miike et al., 1987). Nevertheless, no alterations in muscle blood flow at rest could be observed in DMD patients (Bradley et al., 1975; Gudrun et al., 1975; Leinonen et al., 1979).

Even if the recent studies are notably focused on muscle fibers and satellite cells as the major players in muscular dystrophies, it is accepted that alterations in the vascular system may play an important role in the disease manifestation. Skeletal muscle is highly vascularized, and endothelial cells are essential to muscle regeneration. Dystrophin is expressed also in smooth muscle cells, including endothelial cells, but it is absent in DMD patients and *mdx* mice (Miyatake et al., 1989). The dystrophin absence in endothelial cells reduces its ability to react to shear stress due to blood flow (Loufrani et al., 2001). Since this is a mechanical stimulus for angiogenesis (Ichioka et al., 1997), the dystrophin absence could impair the formation of new vessels in dystrophic muscle (Ennen et al., 2013).

Apart of morphological alterations in the vascular network, dystrophin absence may impact on the vascular function as well. Dystrophin protein links to neuronal NO-synthase (n-NOS) in the sarcolemma of normal muscle cells. The enzyme n-NOS is responsible for the muscular production of the local vasodilator nitric oxide (NO), which acts on relaxing smooth muscle in response to increased metabolic demands (Ennen et al., 2013; Kobzik et al., 1994). Apart from vasodilation function, NO has been related to myofiber differentiation, modulation of the contractile force and regulation of exercise-induced glucose uptake in health muscles (Lee et al., 1994; Roberts et al., 1997). In the absence of dystrophin, n-NOS is present in a reduced amount and is not properly anchored to the sarcolemma (Brenman et al., 1995; Crosbie et al., 2002). The reduced and misplaced n-NOS in the dystrophin absent muscle is considered to increase the damage in the disease (Deconinck and Dan, 2007; Rando, 2001b; Wehling et al., 2001). Indeed, DMD and BMD patients have altered vasoconstriction regulation under exercise, which results in functional ischemia (Sander et al., 2000; Thomas, 2013).

The fibrosis intensely present in muscles from DMD patients has also been related to alterations in blood vessels, due to increased myofiber-capillary distances, which can affect muscle function and gas exchanges (Desguerre et al., 2009). It is known that endothelial cells secrete several soluble factors, which act on the muscle regeneration process, and that satellite cells are preferentially present around vessels. An increased distance between capillaries and myofibers may have an impact on muscle regeneration (Arsic et al., 2004; Christov et al., 2007).

In the recent years, studies aiming to develop new therapeutic approaches for DMD with focus on the vascular network have gained space. It is believed that the attenuation of abnormal microcirculation would reduce muscle damage, increase tissue perfusion and reduce the cardiac workload (Ennen et al., 2013). Increasing the NO available in dystrophic muscle has been efficient to ameliorate the dystrophic phenotype in *mdx* mice, by reducing the post-contraction damage, reducing inflammation, and preserving the number and function of satellite cells (Asai et al., 2007; Brunelli et al., 2007; Voisin et al., 2005). Modulation of vascular endothelial growth factor (VEGF) and its receptor (VEGFR) have also shown benefits in *mdx* mice (Messina et al., 2007). These results indicate that increasing the microvascular

network in muscle could improve the microvascular control and lead to clinical benefits in the dystrophic muscle (Ennen et al., 2013; Shimizu-Motohashi and Asakura, 2014).

Congenital myopathies

Congenital myopathies are a group of genetic muscle diseases with non-dystrophic characteristics in the histological analysis. Nevertheless, clinical presentation in congenital myopathies can be very similar to what is observed in muscular dystrophy patients. Generally, congenital myopathies are characterized by the presence of morphological alterations in the muscle fiber, such as the presence of regions with protein accumulation (rods), regions with altered organelles' distribution (cores), and altered positioning of the nucleus. Despite of these observations in histological analysis, dystrophic characteristics such as inflammation, degeneration, necrosis, extensive fibrosis and regeneration are not observed in general. Creatine kinase level in blood serum is normal or slightly increased in congenital myopathies, while it is highly increased in muscular dystrophies. Additionally, congenital myopathies are not progressive or have very slow progression, in opposition to the progressive pattern of muscle dystrophies (Sewry et al., 2008; Tubridy et al., 2001).

The three major categories of congenital myopathies are nemaline myopathies, core myopathies and centronuclear myopathies. Nemaline myopathies are characterized by the presence of sarcoplasmic or intranuclear rod structures formed by Z-disk derived material. Mutations in the genes alpha-actin (*ACTA1*), nebulin (*NEB*), alpha and beta tropomyosin (*TPM3* and *TPM2* respectively), troponin T1 (*TNNT1*), cofilin (*CLF2*), and a protein of the BTB/Kelch family (*KBTBD13*) can be related to nemaline myopathies. Patients show proximal weakness, respiratory insufficiency and facial weakness. The symptoms can be present at birth or have childhood- and even adult-onset. In general, patients with intranuclear rods have a more severe phenotype than those with sarcoplasmic rods (Jungbluth et al., 2008; Nance et al., 2012; Romero and Clarke, 2012).

Core myopathies are characterized by the presence of areas without any oxidative or glycolytic enzymatic activity, reflecting the absence of mitochondria in that region. One or more core structures can be present in the muscle fiber, with variable size and distributions. Cores can be characterized as central cores or minicores. Central cores run over all length of muscle fibers, while minicores are smaller areas of disorganized myofibrillar material that are wider than longer in longitudinal histological sections. Based on the histological characteristics, patients are classified as having central core disease or multiminicore disease. Mutations in the ryanodine receptor I (*RYR1*) or in the selenoprotein N1 (*SEPN1*) genes can be related to core myopathies. Patients present with proximal muscle weakness, congenital or with early onset, possibly affecting facial muscles. Even if clinical symptoms are present at early age, histological features may not be present, which brings difficulties to the diagnosis (Jungbluth et al., 2008; Nance et al., 2012).

Centronuclear myopathies are characterized by the presence of muscle fibres with internalized or centralized nuclei, in opposition to the peripheral positioning observed in normal muscle fibers. Histopathological characteristics can include abnormal NADH-TR staining, but do not involve extensive muscle degeneration and regeneration. Centronuclear myopathies can be related to mutations in the gene coding for the protein myotubularin (*MTM1*), which leads to the X-linked recessive myotubular myopathy; mutations in the gene coding for amphiphysin 2 (*BINI*), leading to autosomal recessive centronuclear myopathy; mutations in the gene coding for dyanmin-2 (*DNM2*), with autosomal dominant heritage; or to mutations in the *RYR1*, *hJUMPY* and *MTMR14* genes in sporadic cases (Bitoun et al., 2005, 2007; Jungbluth et al., 2008; Tosch et al., 2006; Wilmshurst et al., 2010). A mutation in the *PTPLA* gene was related to centronuclear myopathy in labrador dogs, but until now, there is no report of mutations in this gene causing centronuclear myopathy in humans (Pelé et al., 2005). Clinically, centronuclear myopathies are highly variably regarding the age of onset and pattern of weakness, ranging from severe congenital forms to adult-onset forms with slow progression and mild phenotype (Nance et al., 2012).

Animal Models for Genetic Muscle Diseases

There is no established cure for muscular dystrophies and congenital myopathies, which prompted the search for innovative therapeutic protocols, including cellular and genetic therapies. In this context, animal models for these genetic muscle diseases have an essential role in the elucidation of disease pathomechanisms and in the development of new therapeutic strategies. Several animal models for genetic muscle diseases have been described in the literature, including natural and genetically engineered models. These animals mimic the genetic, molecular and/or clinical aspects of the disease, providing information about the pathogenesis of these disorders and allowing tests for therapeutic strategies (Vainzof et al., 2008).

Animal models for Muscular Dystrophies

The *Dmd*^{*mdx*} mouse (hereafter called simply *mdx*) is the most frequently studied mouse model for DMD. This mouse has a stop codon in exon 23 of the murine dystrophin gene, which leads to total absence of this protein in muscle, as observed in DMD patients (Bulfield et al., 1984; Sicinski et al., 1989). The absence of the protein dystrophin leads to an associated reduction of other DGC proteins (Ohlendieck and Campbell, 1991), with consequent progressive muscle deterioration and weakness (Pastoret and Sebillé, 1995). Histological analysis shows dystrophic changes such as variation in the caliber of muscle fibers, presence of muscle fibers with centralized nuclei, clusters of degenerating and regenerating fibers, infiltration by inflammatory cells and by connective tissue (Bulfield et al., 1984). As observed in human patients, different skeletal muscles are not identically affected. Diaphragm presents accentuated and earlier dystrophic characteristics, while masseter muscle is partially spared and limb muscles like gastrocnemius have an intermediary phenotype (Muller et al., 2001; Stedman et al., 1991). Nevertheless, differently from human patients, the *mdx* mouse can continuously regenerate its muscles and has a mild

phenotype, which makes the analysis of functional benefits in therapeutic protocols very difficult (Dangain and Vrbova, 1984; Dubowitz, 2004; Tanabe et al., 1986).

Dog models for dystrophinopathies in general have the phenotype closer to that observed in human patients. Spontaneous mutations in the dystrophin gene were observed in Golden Retriever (Valentine et al., 1992), Rotweiler (Winand et al., 1994) and German Shorthaired Pointer dogs (Schatzberg et al., 1999). The Golden Retriever Muscular Dystrophy dog (GRMD) is the more frequently studied canine model to DMD. GRMD dogs have a mutation in the dystrophin gene, leading to absence of the protein in muscle. Histopathological evaluation shows progressive dystrophic alterations in skeletal and cardiac muscles, and the phenotype is very severe. GRMD dogs mimic the molecular, histopathological and phenotypical aspects of DMD, being frequently used in the last step of therapeutic trials before tests in human patients (Shelton and Engvall, 2005). Recently, the GRMD mutation has been transferred to Beagle dogs, a smaller canine strain widely used in research (Shimatsu et al., 2003).

The animal models for LGMD include mutations in the respective genes, with special attention to the sarcoglycans genes. Absence of δ -sarcoglycan was observed as the primary molecular defect in BIO14.6 hamsters. This hamster has a spontaneous mutation in the gene coding for the protein δ -sarcoglycan, leading to its absence in muscle (Straub et al., 1998). Mouse models have been generated with null mutation in each of the four sarcoglycans genes (Araishi et al., 1999; Duclos et al., 1998; Hack et al., 1998). Animal models of sarcoglycanopathies present progressive muscular dystrophy with variable degree of severity, in some cases including cardiomyopathy. In all these models, there is a secondary reduction in the expression of the other components of the sarcoglycans/sarcospan complex, and loss of membrane integrity (Allamand and Campbell, 2000).

There are interesting mouse models of congenital muscular dystrophies, with alterations in the link between the DGC complex and the extracellular matrix. Among them, dy/dy and dy^{2J}/dy^{2J} mice were identified in Jackson Laboratories (<http://www.jax.org/>), presenting total and partial deficiency of the protein α -2 laminin, muscular dystrophy and dysmyelination of the peripheral nervous system. These mouse lineages model merosin-deficient congenital muscular dystrophy

(CMD1A), but dy^{2J}/dy^{2J} mice have a milder phenotype than the dy/dy lineage (Vainzof et al., 2008). Two α -2 laminin knock-out strains have been generated, with complete absence of this protein: $dy3K$ and dyW . These mouse strains show severe phenotype, similar to that observed in the dy/dy mouse (Kuang et al., 1998; Miyagoe et al., 1997).

The $Large^{myd}$ mouse is the murine model for CMD-1D. It has a mutation in the *Large* gene, which codes for the glycosyltransferase LARGE protein. The mutation leads to a reduced glycosylation of α -DG, and a consequent reduction in its binding to α -2 laminin in the extracellular matrix (Moore and Winder, 2012). Patients with CMD-1D have a very severe phenotype, with muscular and cognitive impairment (Muntoni et al., 2008). $Large^{myd}$ mice have also a severe phenotype, with accentuated muscle degeneration and substitution by connective tissue. Mice have a shortened lifespan, reduced size and neurological impairment (Grewal and Hewitt, 2002).

Double mutant mice with the *mdx* background have been created in the attempt to approach the severe phenotype observed in DMD patients, such as the double knockout $mdx:utrnl/-$, with absence of both dystrophin and utrophin. It has been proposed that the protein utrophin, a homolog of dystrophin, could partially compensate for the absence of this protein in the *mdx* mice, being responsible for its mild phenotype. Double mutant mice with both utrophin and dystrophin absence have a much more severe muscular and cardiac phenotype than *mdx* mice, closer to that observed in DMD patients (Deconinck et al., 1997; Grady et al., 1997).

Recently, the double mutant $Dmd^{mdx}/Large^{myd}$ mouse (hereafter-called $mdx/Large^{myd}$) has been generated in our laboratory by crossbreeding of *mdx* and $Large^{myd}$ lineages. Homozygous mice for both mutations present a very severe phenotype, worse than both parental lineages. Lifespan is reduced and the degree of muscle degeneration and infiltration by connective tissue is increased when compared to the parental lineages. These mice have a partial deficiency of the enzyme LARGE, and a complete absence of the protein dystrophin. It has special interest in testing cellular or genetic therapeutic protocols, since it allows the evaluation of the dystrophin expression as a marker of therapeutic success (Martins et al., 2013).

Animal models for congenital myopathies

There are several mouse models for nemaline myopathy, including mouse models with mutation in the α -actin gene *Acta1* (Ravenscroft et al., 2011), the nebulin gene (Ottenheijm et al., 2013; Yamamoto et al., 2013), the muscular troponin T gene (Wei et al., 2014) and the cofilin2 gene (Gurniak et al., 2014). All these mouse models have phenotype very similar to what is observed in human patients. Mouse models for core myopathies include the *Sepn1* knockout mouse, which do not present weakness and histopathological features as observed in humans (Rederstorff et al., 2011), and the knock-in models with mutation in *Ryr1*, which model the clinical and histological alterations observed in patients (Boncompagni et al., 2009; Zvaritch et al., 2009).

The myotubular myopathy murine models include the *Mtm1* knock-out (Buj-Bello et al., 2002) and the *Mtm1* p.R69C knock-in mice (Pierson et al., 2012), which model the myotubular myopathy with similar clinical and histological features as observed in patients. Fugier and collaborators have developed a mouse with altered splicing in the *Bin1* gene and muscle weakness, possibly modeling the autosomal recessive form of centronuclear myopathy (Fugier et al., 2011). Finally, the most frequent mutation in patients with centronuclear myopathy related to dynamin-2 has been inserted in the knock-in *KI-Dnm2^{R465W}* mouse. Heterozygous mice have only a small proportion of centronucleated fibers, in opposition to what is observed in humans. Muscle atrophy and force reduction are progressive and start at 2 months of age (Durieux et al., 2010).

Dog models for congenital myopathies include the Labrador retriever with mutation in the *PTPLA* gene (Pelé et al., 2005), the Labrador retriever with mutation in the *MTM1* gene (Beggs et al., 2010) and dogs with canine Inherited Myopathy of Great Danes (IMGD), with mutation in the *BINI* gene (Böhm et al., 2013). Similar to the dog models for muscular dystrophies, canine models for congenital myopathies have phenotype similar as the observed in human patients. Mutations in the *RYR1* gene have been described in pigs (Fujii et al., 1991), dogs (Roberts et al., 2001) and horses (Aleman et al., 2004), but the major clinical manifestation observed in these animals is the malignant hyperthermia phenotype instead of core myopathy. These

animal models have spontaneous mutations, in opposition to the engineered mouse models.

Recently, Childers and collaborators could correct the muscle pathology and prolong the lifespan in murine and canine models for myotubular myopathy with mutation in the *MTM1* gene. Treatment was efficient when used both in initial and late stages of the disease, raising hope to patients and researchers in this field (Childers et al., 2014). Noninvasive methods to follow the possible benefits of these new therapeutic strategies in clinical trials are highly desirable. In this context, NMR studies in patients and animal models for muscle diseases have been developed, in a first moment to better describe the muscle involvement in these disorders, but with potential use as an outcome measure in clinical trials.

Non-invasive evaluation of genetic muscle diseases

The diagnostic of genetic muscle diseases is based on clinical evaluation, quantification of muscle proteins in serum, electromyography, muscle biopsy and molecular analysis. Due to the large spectrum of genes related to muscle disorders, genetic testing can be a difficult task, especially while next generation sequencing is not widely used. In this way, imaging methods such as Computed Tomography (CT) and Magnetic Resonance Imaging (MRI) can allow the identification of the pattern of muscle involvement, orienting the genetic testing and helping in the differential diagnosis. Muscle MRI and CT from patients with genetic muscle disorders allowed the identification of the pattern of muscle involvement in these diseases, with strong correlation with genotype. The pattern of affected and spared skeletal muscles varies among muscular dystrophies, congenital myopathies and also between other muscle pathologies, such as inflammatory myopathies (Lamminen, 1990; Mercuri et al., 2007; Quijano-Roy et al., 2011, 2012; Wattjes et al., 2010). Early and correct diagnosis can affect the management of muscular dystrophy and congenital myopathy patients, since some of these diseases may involve cardiac and pulmonary complications that require early intervention (Shieh, 2013).

Besides of its importance in helping diagnosis, nuclear magnetic resonance (NMR) imaging (MRI), spectroscopy (MRS) and functional analysis (fMRI) have been used to study muscle morphology, metabolism and function in genetic muscle diseases. The non-invasive character of NMR, the use of non-ionizing radiation, the good contrast between fat and muscle tissue, and the possibility of studying muscle metabolism and function makes NMR a very interesting tool in the follow up of the natural history and of the effects of therapeutic trials in muscle disorders.

It has been shown that muscle MRI correlates with clinical evaluation in DMD patients (Liu et al., 1993), but it allows additionally the identification of muscle impairment before the evidence of clinical signs, like in mild BMD patients and DMD female carriers (Tasca et al., 2012a, 2012b). MRI methods that can identify fat infiltration in muscles, presence of edema related to inflammation or necrosis, and that quantify fat and water content in muscles have been extensively applied in the study of DMD patients (Fischmann et al., 2012, 2013; Gaeta et al., 2012; Leroy-Willig et al., 1997; Marden et al., 2005; Pichiecchio et al., 2002; Wren et al., 2008). Quantitative NMR (T1 and T2 measurements) also correlates with clinical parameters and with qualitative evaluation of the fat content in muscle MRI from DMD patients, raising the interest on its use in disease and therapy monitoring (Arpan et al., 2013; Huang et al., 1994; Kim et al., 2010; Mavrogeni et al., 2009; Willcocks et al., 2014).

When applied to different muscle dystrophies, NMR still gives interesting results. It has been shown that muscle and brain NMR correlate with clinical and genetics in myotonic dystrophy (Bachmann et al., 1996) and dysferlinopathies (Paradas et al., 2010). Oculopharyngeal muscular dystrophy patients, who present a very mild phenotype with slow progression, present MRI alterations that correlate with the disease progression, and that can be detected in a more sensitive way with MRI than with clinical evaluation (Fischmann et al., 2012).

Metabolic and functional NMR evaluation of dystrophic muscle have shown impaired metabolism in DMD patients, with changes in pH and altered metabolite ratios in ^{31}P (Newman et al., 1982; Torriani et al., 2012) and ^1H MRS (Hsieh et al., 2009). DMD patients also showed higher intracellular Na^+ levels in ^{23}Na MRS (Weber et al., 2011). ^{31}P MRS alterations were also observed in milder dystrophies at rest or in exercise protocols, such as in BMD (Lodi et al., 1999; Tosetti et al., 2011)

and LGMD (Lodi et al., 1997). MRI has been additionally used to track cell injected in DMD patients (Odintsov et al., 2013).

NMR in the study of animal models for genetic muscle diseases

When applied to small animals, NMR faces the challenge of reducing dimensions and increasing resolution. Additionally, while in human patients with muscle disorders the muscle degeneration is followed by fat infiltration, mouse models for muscle diseases present low to zero fat infiltration in muscles (Carnwath and Shotton, 1987; McIntosh et al., 1998b). MRI analysis of intramuscular fat infiltration is therefore not as informative in mice as it is in patients, which raises the interest in other NMR approaches to non-invasively evaluate murine models, such as quantitative T1 and T2 measurements, in vivo spectroscopy and functional NMR.

It has been shown that *mdx* mice have increased muscle T2 values, at rest and after exercise (Mathur et al., 2011). Muscle heterogeneity in T2-weighted MRI also changes in *mdx* mice with the disease evolution (Pratt et al., 2013), indicating that not only T2 values but also quantitative measures of the distribution of muscle alterations can correlate with the phenotype in dystrophic mice. Muscle T2 has already been used to follow dystrophic muscle after gene therapy in a murine model for LGMD-2D (Pacak et al., 2007).

While all these studies compared dystrophic murine models to wild-type or control mice with the same background, Tardif-de-Géry and collaborators have compared muscle T2 values from two mouse models with deficiency in the protein laminin, the very severely affected *dy/dy* mouse and the dystrophic, but less severely affected, *dy^{2J}/dy^{2J}* mouse. Both models have increased T2 when compared to wild-type mice at least in one stage of the disease, but no difference was observed between the two dystrophic mouse strains (Tardif-de Géry et al., 2000).

MRI can also be informative in the evaluation of sarcoplasmic membrane integrity in murine models for muscle dystrophies. Mutations in the DGC components can lead to alterations in the sarcoplasmic membrane, increasing its permeability. This can be accessed by injection of contrast agents that will be internalized in muscle

fibers in a different manner if there are membrane alterations. In addition, this approach can reveal which muscles have more membrane damage. In this way, it was possible to reveal muscle membrane alterations *in vivo* in *mdx* (Amthor et al., 2004; Straub et al., 2000), *scga*-null (Straub et al., 2000) and dysferlin-deficient mice (Schmidt et al., 2009).

Metabolic alterations have also been accessed *in vivo* by ¹H and ³¹P MRS in *mdx:utrn*^{-/-} mice (Cole et al., 2002) and *in vitro* by ¹H MRS in different tissues of *mdx* mice (Griffin et al., 2001; McIntosh et al., 1998a). Finally, alterations in muscle MRI have been tracked after gene therapy in the murine model for LGMD-2D (Pacak et al., 2007), highlighting the value of NMR in the non-invasive tracking of therapeutic benefices in mouse models for muscle dystrophies.

There are still very few NMR studies with animal models for congenital myopathy. Gineste and collaborators have developed a series of NMR studies in three different mouse models for nemaline myopathy. The heterozygous nebulin knock-out mouse was studied by ³¹P NMR and MRI, combined with force measures, protein and gene expression analysis. Force reduction and altered proteomic profile were observed (Gineste et al., 2013c). The H40Y mouse, with mutation in the actin α -1 gene, showed reduced force but no changes in subcutaneous or intermuscular fat, neither in ³¹P spectroscopy. The similar energetic consumption with a decreased muscle force indicated that the energetic metabolism is altered in H40Y mice, with increased energetic cost for muscle contraction (Gineste et al., 2013a). Finally, the transgenic *Tg(ACTA1)Asp286Gly* mouse, also with mutation in actin α -1, was evaluated with NMR and force measures. These mice showed muscle atrophy, force reduction and increased muscle T2, without fat infiltration and no differences in the ³¹P MRS, indicating higher energetic cost for the muscular activity (Gineste et al., 2013b).

Chapter 2

Quantitative T2 combined with texture analysis of nuclear magnetic resonance images identify different degrees of muscle involvement in three mouse models of muscle dystrophy: *mdx*, *Large^{myd}* and *mdx/Large^{myd}*

Chapter 2. Quantitative T2 combined with texture analysis of nuclear magnetic resonance images identify different degrees of muscle involvement in three mouse models of muscle dystrophy: *mdx*, *Large^{myd}* and *mdx/Large^{myd}*

This chapter has been submitted and accepted for publication in the journal Plos One. DOI: 10.1371/journal.pone.0117835. In Press (January 2015).

Authors: Aurea B. Martins-Bach, Jackeline Malheiros, Béatrice Matot, Poliana C. M. Martins, Camila F. Almeida, Waldir Caldeira, Alberto F. Ribeiro, Paulo Loureiro de Sousa, Noura Azzabou, Alberto Tannús, Pierre G. Carlier, Mariz Vainzof.

Abstract

Quantitative nuclear magnetic resonance imaging (MRI) has been considered a promising non-invasive tool for monitoring therapeutic essays in small size mouse models of muscular dystrophies. Here, we combined MRI (anatomical images and transverse relaxation time constant - T2 - measurements) to texture analyses in the study of four mouse strains covering a wide range of dystrophic phenotypes. Two still unexplored mouse models of muscular dystrophies were analyzed: the severely affected *Large^{myd}* mouse and the recently generated and worst double mutant *mdx/Large^{myd}* mouse, as compared to the mildly affected *mdx* and normal mice. The results were compared to histopathological findings. MRI showed increased intermuscular fat and higher muscle T2 in the three dystrophic mouse models when compared to the wild-type mice (T2: *mdx/Large^{myd}*: 37.6 ± 2.8 ms; *mdx*: 35.2 ± 4.5 ms; *Large^{myd}*: 36.6 ± 4.0 ms; wild-type: 29.1 ± 1.8 ms, $p < 0.05$), in addition to higher muscle T2 in the *mdx/Large^{myd}* mice when compared to *mdx* ($p < 0.05$). The areas with increased muscle T2 in the MRI correlated spatially with the identified histopathological alterations such as necrosis, inflammation, degeneration and regeneration foci. Nevertheless, muscle T2 values were not correlated with the severity of the phenotype in the 3 dystrophic mouse strains, since the severely affected *Large^{myd}* showed similar values than both the mild *mdx* and worst *mdx/Large^{myd}* lineages. On the other hand, all studied mouse strains could be unambiguously identified with texture analysis, which reflected the observed differences in the distribution of signals in muscle MRI. Thus, combined T2 intensity maps and texture analysis is a powerful approach for the characterization and differentiation of dystrophic muscles with diverse genotypes and phenotypes. These new findings provide important noninvasive tools in the evaluation of the efficacy of new therapies, and most importantly, can be directly applied in human translational research.

Introduction

The muscular dystrophies are an extensive group of genetic diseases where the major characteristic is the progressive muscle degeneration, caused by mutations in genes coding for sarcolemmal, sarcomeric, cytosolic, nuclear or extracellular matrix proteins. The absence or altered function of one of these proteins is responsible for a cascade of events, which ends in the muscle fibers degeneration and substitution by connective and adipose tissue. The patients present progressive weakness, starting at different ages depending on the mutation. Up to now, there is no effective cure for this group of diseases, and several therapeutic protocols are in development (Buckland and Gaspar, 2014; Emery, 2002).

The most frequent form of muscular dystrophy is Duchenne Muscular Dystrophy (DMD), caused by mutations in the dystrophin gene and with an incidence of 1 in 3300 live male births (Deconinck and Dan, 2007; Hoffman et al., 1987). The dystrophin protein is part of the dystrophin-glycoprotein complex (DCG), which links the cytoskeleton from muscle fibers to the extracellular matrix. This connection is mediated by the dystroglycan complex, composed by the sarcolemmal beta-dystroglycan (β -DG) subunit and the peripheral membrane alpha-dystroglycan (α -DG). While β -DG links to the subsarcolemmal protein dystrophin, α -DG is responsible for the connection with the extracellular matrix protein α -2 laminin. This link occurs via the sugar chains in the glycosylated extension of α -DG, which have high affinity to Laminin G (LG)-like domains present in various extracellular matrix proteins, such as laminins, perlecan and agrin in muscle, and neurexin in brain (Barresi and Campbell, 2006; Ervasti and Campbell, 1993; Straub and Campbell, 1997). Mutations in the gene coding for dystroglycans are very rare, but alterations in α -DG glycosylation are related to several forms of myopathy, such as limb girdle muscular dystrophies and congenital muscular dystrophies (Muntoni et al., 2008).

The study of animal models for neuromuscular disorders has an essential role in understanding the pathogenetic mechanisms of the muscular diseases and in the development of therapeutic strategies. There are several natural or created animal models for the different forms of muscle dystrophy, which can model the genetic, molecular and/or clinical aspects of the disease. The *Dmd*^{mdx} mouse (hereafter called

simply *mdx*) is the most frequently used mouse model for DMD. This mouse has a stop codon in exon 23 of the murine dystrophin gene, which leads to the total absence of this protein in the muscle, as observed in DMD patients (Bulfield et al., 1984; Hoffman et al., 1987; Sicinski et al., 1989). Nevertheless, differently from the human patients, the *mdx* mouse can continuously regenerate its muscles and has a mild phenotype, which makes the analysis of functional benefices in therapeutic protocols very difficult (Dangain and Vrbova, 1984; Dubowitz, 2004).

Double mutant mice with the *mdx* background have been created in the attempt to approach the severe phenotype observed in DMD patients, such as the double knockout *mdx:utrn*^{-/-}, with absence of both dystrophin and utrophin (Deconinck et al., 1997; Grady et al., 1997); the *mdx/mTR* mouse, with impaired telomerase activity (Sacco et al., 2010); and the *Dmd*^{*mdx*}-*Large*^{*myd*} mouse (hereafter called *mdx/Large*^{*myd*}), recently generated in our laboratory by crossing *mdx* and *Large*^{*myd*} murine lineages (Martins et al., 2013). The *Large*^{*myd*} myodystrophy mouse has a mutation in the glycosyltransferase *Large* gene, which leads to reduced glycosylation of α -DG and a severe and progressive myodystrophy. Mutations in the human gene *LARGE* are related to congenital muscular dystrophy 1D (CMD1D), with severe muscle and central nervous system involvement. The double mutant *mdx/Large*^{*myd*} mouse presents deficiency of both dystrophin and *LARGE* proteins, and a very severe phenotype, worse than both parental lineages. The lifespan is reduced and the degree of muscle degeneration and infiltration by connective tissue is increased when compared to the parental lineages. The *mdx/Large*^{*myd*} mouse gives clues of the interplay between α -DG glycosylation and dystrophin deficiency and is useful for testing therapies due to the functional, genetic and protein alterations (Martins et al., 2013).

Different therapeutic strategies for muscular dystrophies are in development, including genetic and cellular approaches. The gold standard to evaluate the dystrophic muscle is still the histological analysis, but non-invasive methods are highly desirable. Nuclear magnetic resonance (NMR), and more specifically magnetic resonance imaging (MRI), have a great potential in the study of skeletal muscle due to its flexibility in generating images from soft tissues with different contrasts, additionally enabling metabolic and functional studies. MRI studies in dystrophic

patients have revealed different patterns of muscle involvement depending on the mutation, which can be used to orient the molecular testing in the differential diagnosis (Quijano-Roy et al., 2012; Wattjes et al., 2010). Human DMD clinical evolution and muscle metabolism alterations can be non-invasively tracked by NMR, with a good correlation between quantitative NMR parameters and the clinical evaluation (Arpan et al., 2013; Fischmann et al., 2013; Gaeta et al., 2012; Hsieh et al., 2009; Torriani et al., 2012; Tosetti et al., 2011; Willcocks et al., 2014; Wren et al., 2008).

When applied to small animals, MRI faces the challenge of reducing dimensions and increasing resolution. Additionally, differently from human patients, mouse models of muscular dystrophies present low to zero fat infiltration in the muscle (Carnwath and Shotton, 1987; McIntosh et al., 1998b). The MRI analysis of intra-muscular fat infiltration is therefore not as informative in mice as it is in patients, which prompted the search for other MRI approaches to non-invasively evaluate mouse models, such as transverse relaxation time constant (T2) measurements and muscle texture analysis.

T2 is an NMR value intrinsic for each type of tissue, reflecting the motility of its water protons. When the examined tissue presents pathologic processes such as necrosis, inflammation or edema, this dynamic is altered, which results in changes in the tissue T2. Previous studies have reported abnormal muscle T2 in some dystrophic models, such as *mdx* (McIntosh et al., 1998; Walter et al., 2005; Mathur et al., 2011), γ -sarcoglycan knock-out *ysg*^{-/-} (Walter et al., 2005), α -sarcoglycan knock-out *sgca*^{-/-} (Pacak et al., 2007), and α -2 laminin deficient *dy/dy* and *dy*^{2J}/*dy*^{2J} mouse models (Tardif-de G ry et al., 2000), as compared to normal controls. Texture analysis is an emerging approach that includes several techniques to quantify variations in the image intensity or patterns. When applied to muscle MRI, texture analysis has demonstrated to be a potential tool to evaluate subtle differences in the pattern of distribution of muscle lesions (Mahmoud-Ghoneim et al., 2006; Nketiah et al., 2014; Škoch et al., 2004). In the *mdx* mouse (Pratt et al., 2013) and the GRMD dystrophic dog (Fan et al., 2014), longitudinal studies were able to correlate texture parameters with age and progression of the disease.

Considering this, we hypothesized that T2 measurements combined to muscle MRI texture analysis would be sensitive enough to characterize and differentiate dystrophic muscle phenotypes caused by different gene mutations. Here, we used this approach to evaluate two still unexplored mouse models of muscular dystrophies, the recently generated *mdx/Large^{myd}* mouse and the *Large^{myd}* parental lineage, in addition to *mdx* and C57Bl mice. These mouse strains cover a wide range of dystrophic phenotypes, with variable degrees of muscle necrosis and inflammation, and could be unambiguously identified with quantitative muscle T2 and texture analysis. The new findings will have important applications to noninvasive follow of potential therapeutic protocols.

Materials and Methods

Ethics Statement

All the experiments were approved by the Research Ethics Committee of the Biosciences Institute, University of São Paulo, protocol 176/2013.

Animals

Four mouse strains were evaluated: the dystrophic *mdx*, *Large^{myd}* and *mdx/Large^{myd}*, in addition to C57Bl/6 mice as normal controls (wild-type). 47 mice, aged between 2 and 4 months (8-19 weeks), both male and female, were studied: 9 double mutants *mdx/Large^{myd}*, 13 *mdx*, 12 *Large^{myd}* and 13 wild-type. As the two models with a weaker phenotype, in particular *mdx/Large^{myd}* mice, are difficult to obtain (25% of affected sibling and high degree of perinatal death, (Martins et al., 2013)), a more flexible range of ages was adopted. To homogenize the groups, the accepted age range was allowed to vary between 8 and 18 weeks for all mouse strains. At this stage, muscle dystrophy is patent in all mouse strains. This age range is posterior to the critical period in *mdx* mice, when a peak of myofiber necrosis, muscle

weakness and regeneration is observed between the 2nd and the 5th weeks of life (Muntoni et al., 1993). All the animals were from the Human Genome Research Center animal house, Bioscience Institute (Sao Paulo). The mice were kept in controlled environment, with water and food at libidum.

Magnetic Resonance Imaging acquisition and analysis

The mice were anesthetized with intraperitoneal injection of ketamine:xylazine (2:1, 1.5-2.5 μ l/g according to the lineage) and symmetrically positioned for the MRI acquisitions. The images were acquired in a 2 tesla/30 cm bore superconducting magnet (Oxford Instruments 85310HR, Abingdon, United Kingdom), interfaced to a Bruker Avance AVIII console (Bruker-Biospin, Inc., Billerica, MA, U.S.A.) running PARAVISION 5.0. A crossed-saddle radiofrequency coil projected for small animals (Papoti, 2006) was used to image the mice's posterior limbs.

Four scans were performed in each mouse, with the same geometry (4 slices, 1.5 mm slice thickness, 4 mm inter-slice distance and spatial resolution 0.176X0.176 mm²/pixel): two scans for anatomical images with the same parameters (repetition time - TR=1800 ms, echo time - TE=52.5 ms), with and without fat suppression for qualitative evaluation of possible fat infiltration in the muscles (with fat suppression:16 averages; without fat suppression: 4 averages); and two scans for the calculation of the T2 maps, each one using a different echo time (to avoid the contribution of stimulated echoes): TE₁=12.1 ms and TE₂=40 ms (TR=1500 ms, 1 average when TE₁=12.1 ms, 4 averages when TE₂=40 ms, spatial resolution: 0.176X0.176 mm²/pixel). The T2 value for each pixel was calculated using the Bloch equation for the spin-spin relaxation time (Supporting Information S2.1), and T2 maps were generated using a routine developed in the MATLAB software (The MathWorks, Inc., Natick, Massachusetts, USA). The total acquisition time was 51 minutes. The examination time never exceeded 1 hour and 30 minutes.

In the T2 maps, two slices were selected for analysis: one positioned at the lower leg and one at the thigh. One slice was considered representative of thigh and

leg muscles since injured fibers would present anomalies along all its length. Nevertheless, this limits the analysis to the muscles observed in a defined anatomical position.

Four Regions of Interest (ROI) were evaluated: two in the lower leg T2 map, at the posterior and anterior compartment muscles, and two in the thigh T2 maps, covering the medial and lateral muscles. The ROIs were drawn to exclude any non-muscle tissue. For each ROI, the mean T2 value and the standard deviation were analyzed.

The muscle texture in MRI was evaluated with the softwares MaZda 4.6 and B11 3.3 (Strzelecki et al., 2013; Szczypinski et al., 2007; Szczypiński et al., 2009), using the T2-weighted images acquired with TE=40 ms and TR=1500 ms. The lower leg image was selected and one ROI was drawn in the left lower leg of each mouse, including all muscle groups but excluding subcutaneous fat, bones and skin. All the 371 texture features offered by the Mazda software were calculated. The co-occurrence matrices parameters contrast and entropy were selected due to their significance for the identification of our studied groups, and resulted in the reduction of the 371 features to 40. Among them, Mazda software automatically selected 30 features, by combining the maximization of the Fischer coefficients, the maximization of the mutual information between two selected features, the minimization of the classification error probability and minimization of the average correlation coefficients (F+PA+MI). The 30 selected features (listed in Supporting Information S2.2) were then used as input to Linear Discriminant Analysis (LDA) in the software B11.

Histological analysis

Two days after the NMR session, the mice were euthanized in a CO₂ chamber. The whole left leg was collected and preserved in formaldehyde solution (4% in Phosphate Buffer Saline - PBS). The right leg was dissected and the lower leg posterior compartment (gastrocnemius and soleus) was imbedded in Tissue-tek OCT

freezing medium (Optimal Cutting Temperature, Sakura Finetek USA, Torrance, CA, USA) and frozen in liquid nitrogen.

The histological qualitative evaluation was performed on at least 2 mice for each lineage. The formaldehyde-preserved samples were decalcified and embedded in plastic resin according to the manufacturer procedure (HistoResin, Leica, Wetzlar, Germany). Resin embedded samples were cut in 5 μm slices and frozen samples were cut in 8 μm slices. Both frozen and resin embedded histological sections were stained with Hematoxylin and Eosin (H&E). Additional Gomori trichrome and sirius red staining were done in the frozen sections.

Statistic analysis

The T2 mean values for each ROI were analyzed with a three-factors ANOVA, followed by the Bonferroni muticomparison test when ANOVA detected differences ($p < 0.05$). The three considered factors were: presence of the mutation in the dystrophin gene ($Dmd^{+/+}$ =no mutation/ $Dmd^{-/-}$ =with mutation); presence of the mutation in the gene *Large* ($Large^{+/+}$ =no mutation/ $Large^{-/-}$ =with mutation); and muscle group (1: lower leg posterior, 2: lower leg anterior, 3: thigh lateral, 4: thigh medial). The lineage was split in two factors to evaluate a possible cumulative effect of both mutations in the double mutant *mdx/Large^{myd}* mouse, and the muscle groups were studied separately to evaluate a possible different pattern of muscle involvement in the dystrophic mouse strains. The differences were considered significant when $p < 0.05$. This level of significance was achieved in ANOVA when $F(1,164) > 3.90$ for the comparison of mice from different genetic background and when $F(3,164) > 2.66$ for the comparison of different muscle groups. Analyses were performed with NCSS 2001 software (Kaysville, Utah, USA).

Results

The three dystrophic mouse strains showed increased amount of fat between the muscles when compared to the wild-type mice (Figure 2.1). However, no intra-muscular fat could be detected in any of the mouse strains with MRI: the muscle hyperintensities present in the images without fat suppression (Figure 2.1, *NFS*) were identically observed in the images with fat suppression (Figure 2.1, *FS*), indicating that these areas were not related to fat infiltration.

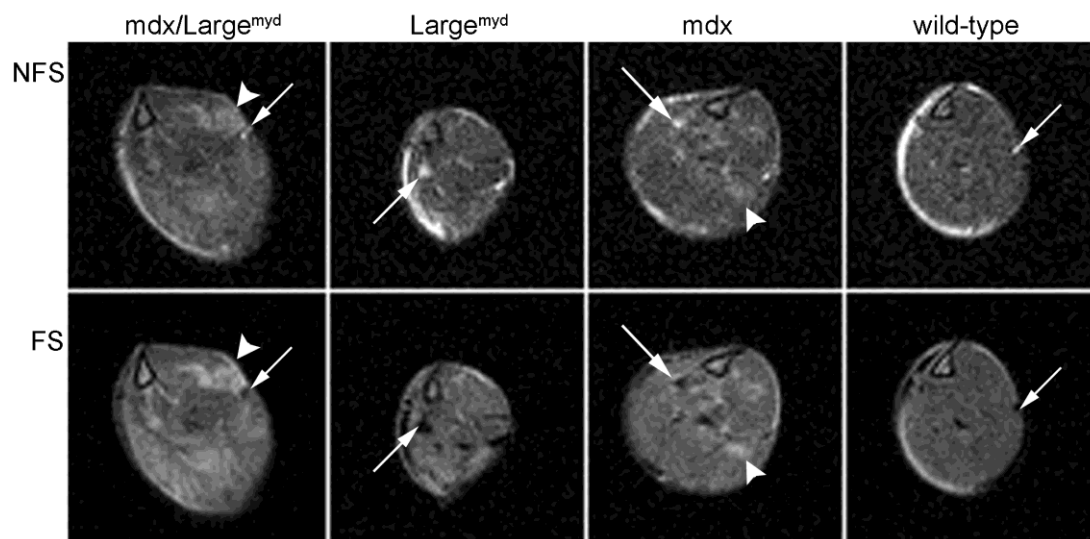


Figure 2.1: Intermuscular fat in dystrophic mice. MRI of the four mouse strains (lower leg), showing intermuscular fat but no visible fat infiltration in the muscles in the three dystrophic strains. The arrows indicate the presence of fat between the muscles, as bright areas in the non fat-suppressed images (NFS) and dark areas in the images with fat suppression (FS). The arrowheads indicate hyperintense areas present in the images with and without FS, which are therefore not related to fat infiltration. TE=52.5 ms, TR=1800 ms.

Muscle T2

In the individual comparison between muscle groups for each lineage, only the wild-type mice showed differences: thigh medial muscles have higher muscle T2 than the lower leg muscles ($p<0.01$). In the three dystrophic strains no differences were observed between the muscle groups. Therefore, all muscles were grouped in one unique T2 value for each animal for the comparison between the mouse strains (Table 2.1).

Table 2.1. T2 per muscle group in milliseconds for the four mouse strains studied.

	<i>mdx/Large^{myd}</i>	<i>mdx</i>	<i>Large^{myd}</i>	<i>wild-type</i>
N	9	13	12	13
Lower leg -				
posterior	36.96 ± 2.84	34.95 ± 3.70	35.48 ± 2.15	28.34 ± 1.71
Lower leg -				
anterior	37.15 ± 3.77	33.43 ± 2.85	33.95 ± 3.59	28.05 ± 1.28
Thigh - lateral	37.70 ± 3.07	36.41 ± 7.20	37.79 ± 5.38	29.69 ± 1.36
Thigh - medial	38.34 ± 1.66	36.31 ± 3.00	38.48 ± 2.54	30.36 ± 1.93
Comparison				
between muscles	p=0.76	p=0.32	p=0.025	p<0.01
All muscles	37.56 ± 2.82	35.23 ± 4.53	36.58 ± 4.00	29.11 ± 1.82

No differences were observed between the muscle groups in the three dystrophic mouse strains. p-values are for the comparisons between muscle groups for each mouse strain. Since four individual comparisons were done, the Bonferroni correction was applied and the differences were considered significant if $p<0.0125$.

Considering the mouse strains individually, muscle T2 was markedly increased in the three dystrophic mouse models when compared to the wild-type mice

($p < 0.05$). Additionally, *mdx/Large^{myd}* mice had significantly higher muscle T2 than *mdx* mice ($p < 0.05$, Table 2.1, Figure 2.2).

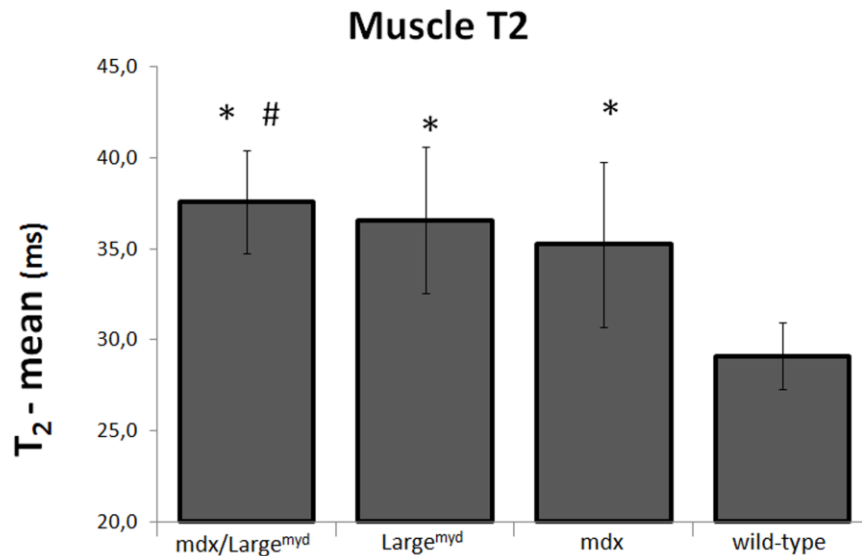


Figure 2.2: Muscle T2 for *mdx/Large^{myd}*, *Large^{myd}*, *mdx* and wild-type mice. Muscle T2 in milliseconds for the four mouse strains evaluated. *: Muscle T2 different from wild-type mice; #: muscle T2 different from *mdx* mice.

When considering the effect of each gene mutation separately in muscle T2 values, ANOVA showed that there was a significant interaction between the absence of dystrophin and the defective glycosylation of α -DG ($p < 0.001$). The presence of both mutations lead to an increase in muscle T2 when compared to the *mdx* mice, but this increase was lower than the simple sum of the effects of each mutation (Figure 2.3).

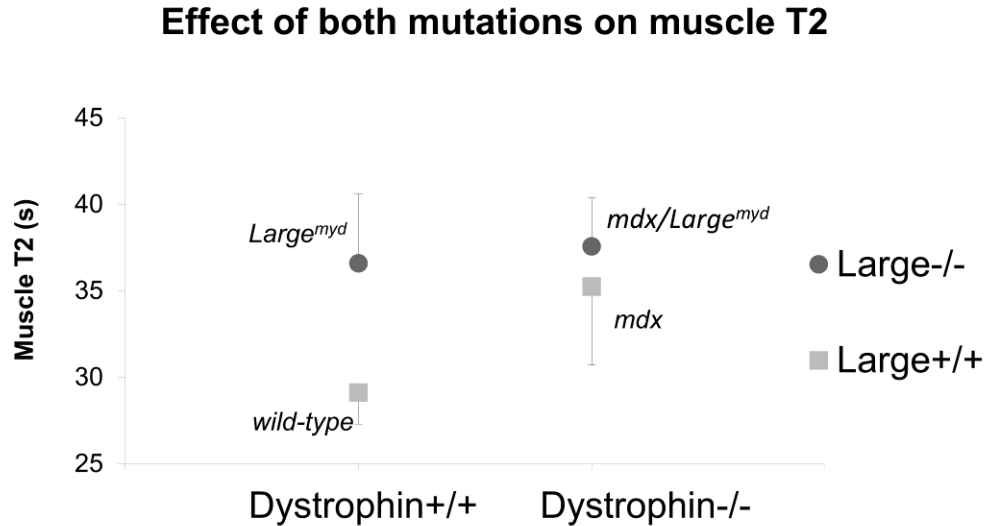


Figure 2.3: Effect of each mutation on muscle T2. Both the dystrophin absence and the α -DG glycosylation defect increase muscle T2, but the combination of both does not produce an additive effect.

Muscle texture analysis

Despite similar values of T2, it was possible to observe differences in the distribution of hyperintense regions in muscle MRI: while *mdx* mice presented focal areas with hyperintense signal randomly distributed in the muscles (patchy), *Large^{myd}* mice presented a global increase in muscle signal, distributed homogeneously in all muscles (waxy). The double mutant *mdx/Large^{myd}* presented a waxy aspect in muscle images, with a few focal hyperintense areas, as a mixture of the patterns observed in the parental strains. The differences in global appearance observed visually in the muscle images from the dystrophic mice were then quantified using texture analysis algorithms. The four groups were properly distinguished with the constructed model, and all the individuals were correctly classified by it. The linear separability was 0.91 and 3 dimensions could model 97% of the original data. Plotting the data over the three dimensions of the model nicely visualized the clustering of the mice into four groups according to the mutation (Figure 2.4).

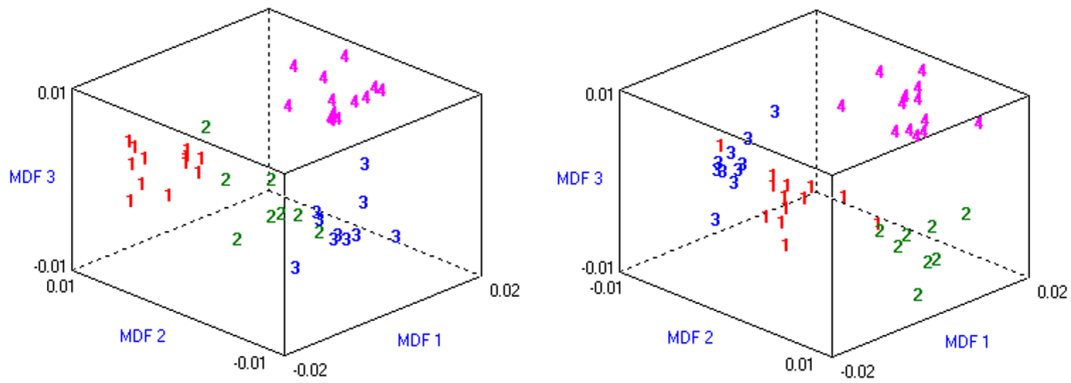


Figure 2.4: Texture analysis differentiates the four mouse strains. Two views of the same plot showing the clustering of mice groups after texture analysis from lower leg MRI. 1: wild-type, 2: *mdx/Large^{myd}*, 3: *Large^{myd}*, 4: *mdx* mice. MDF: Most Discriminant Features.

Histological analysis

The histological analysis was based on qualitative comparison of dystrophic pathologic features, such as the presence of degenerating and regenerating cells foci, necrosis, and infiltration by connective and adipose tissues. Homogeneous and pale eosinophilic sarcoplasm was related to degenerating and necrotic fiber, while basophilic sarcoplasm and central nuclei were related to regenerating fibers (Figure 2.5) (Dubowitz et al., 2013; Salimena et al., 2000).

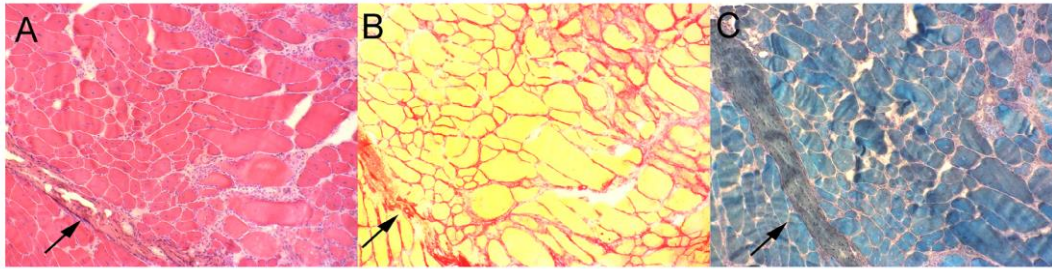


Figure 2.5: Identification of dystrophic pathological structures. Histological sections of a 3 month-old *mdx/Large^{myd}* mouse (frozen sample), approximately at the same position, stained with (A) Hematoxylin-Eosin, (B) Sirius Red, and (C) Gomori trichrome, magnification X 100. The arrows indicate thick areas of connective tissue.

Histological sections from the resin embedded samples, which preserved the anatomical organization of the muscle groups, were chosen to represent the MRI slices (Figure 2.6).

The *mdx* mice showed a patchy pattern in the MRI (Figure 2.6 C), and the hyper-signal areas in MRI corresponded spatially to foci of dystrophic alterations, such as clusters of degenerating and regenerating cells, infiltration by inflammatory cells and spots of adipose tissue in the periphery of the muscles (Figure 2.6 G, K). It was also possible to observe variation in the fibers caliber, high proportion of centronucleated muscle fibers and increased amount of connective tissue in all the lower leg muscles, but these alterations did not necessarily correlate with hyperintense areas in the MRI.

The *Large^{myd}* mice presented dystrophic histological characteristics distributed in a more diffuse pattern through the muscles, in accordance with the waxy pattern observed in the MRI (Figure 2.6 B, F). The histological analysis revealed the presence of degenerating and regenerating muscle cells, inflammatory infiltrates and fibrosis in a diffuse distribution, with occasional small clusters of degenerating and regenerating fibers. The muscles were generally more compromised than in the *mdx* mice (Figure 2.6 J).

The *mdx/Large^{myd}* mice showed infiltration by inflammatory cells, fibrosis and degenerating fibers diffusely distributed across the muscles, such as the *Large^{myd}*

mice, especially in the posterior compartment muscles of the leg. Additionally, there were few big clusters of degenerating and regenerating fibers, which co-localized with hyper-signal areas in the MRI, but in a less accentuated proportion than in the *mdx* mice (Figure 2.6 A, E). In general, the *mdx/Large^{myd}* mice presented a more severe degree of dystrophic lesions in the histological analysis than both parental mouse strains (Figure 2.6 I).

The wild-type mice showed polygonal fibers with regular size and peripheral nuclei. There was no fat accumulation inside the muscles, and between the muscles the amount of fat was reduced in comparison to the three dystrophic mouse strains. The endomysial and perimysial connective tissue were thinner than in the three dystrophic mouse strain (Figure 2.6 H, L). The normal histological pattern was compatible with the homogeneous and low intensity signal in muscle MRI (Figure 2.6 D).

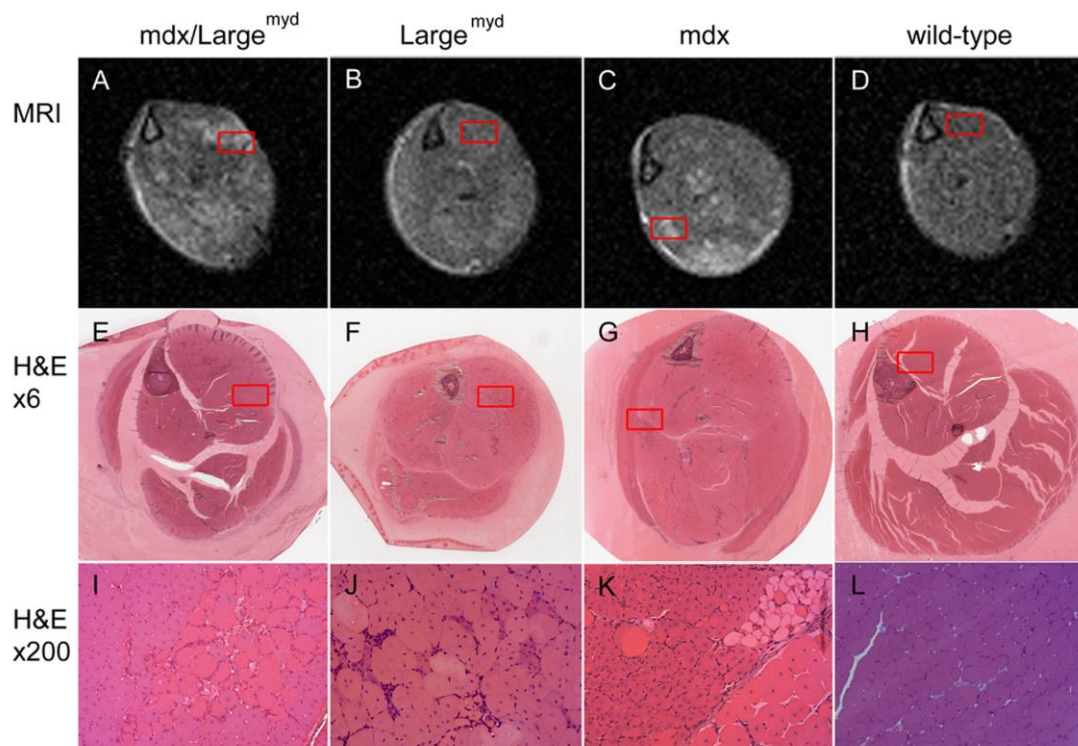


Figure 2.6: MRI versus histological analysis. MRI (A-D; TE=40 ms, TR=1500 ms) and histological images (H&E, magnification X6: E-H; magnification X200: I-L) of the left lower leg from *mdx/Large^{myd}* (A, E, I), *Large^{myd}* (B, F, J), *mdx* (C, G, K) and wild-type mice (D, H, L). The regions highlighted in the MRI (first row) and in the

whole lower leg histological image (second row) are presented in a higher magnification in the third row. Different histological processes could be related to the hyperintensities regions in the MRI, such as clusters of degenerating cells (I), regenerating and adipose cells (K), and regions with mixed dystrophic characteristics (J).

Discussion

Noninvasive tools for muscle evaluation have an immediate application in therapeutic protocols, to follow possible benefits in longitudinal studies with minimal impact on the subjects. For this purpose, it is essential that the selected tool could not only detect differences between dystrophic and normal muscle, but that it could also detect more subtle differences between various degrees of muscle involvement, both in patients and in animal models. In this MRI study, we have evaluated for the first time the muscle MRI pattern in the *Large^{myd}* and the double mutant *mdx/Large^{myd}* mouse models of muscular dystrophy, as compared to *mdx* and C57Bl/wild-type mice. These mouse strains cover a wide range of dystrophic phenotypes, from the mildly affected *mdx* mouse to the severely compromised *mdx/Large^{myd}* mouse. Using a combined approach including qualitative MRI evaluation, muscle T2 relaxometry and texture analysis, in comparison to the standard histological analysis, we have shown that noninvasive MRI can successfully discriminate muscles from these four mouse strains.

MRI acquired with and without fat saturation revealed no identifiable fat infiltration in the muscles of any of the mouse strains, but an increased fat accumulation between the muscles in the MRI could be observed in the dystrophic mice when compared to the wild-type. This observation was confirmed by the histological analysis, where it was possible to identify bigger fat deposits between the muscles in the dystrophic mouse strains. Our results extend to the more severely dystrophic *Large^{myd}* and *mdx/Large^{myd}* models the previously described MRI findings in the *mdx* mouse, of no fat infiltration in skeletal muscles visible with MRI (McIntosh et al., 1998b; Pratt et al., 2013; Walter et al., 2005).

In addition to the increased intermuscular fat, the histological analysis revealed sporadic adipose cells in the muscles of the three dystrophic mouse strains, notably in the *mdx* mice, where small clusters of adipose cells were present especially along the fascia. This is in accordance with previous MRI observation in DMD patients, where increased fat signal along the fascia in young DMD boys was present even when the intramuscular fat replacement was minimal (Marden et al., 2005). Although no fat infiltration could be observed in the mice MRI, we believe that the presence of only sporadic and isolated adipose cells in the muscle would not be visually detected in the MRI in the resolution used in this study. It is possible though that this punctual presence of fat in the muscle can lead to changes in the muscle T1 and T2 measurements, in addition to alterations in the MRI muscle texture.

The quantitative evaluation of the mean muscles T2 showed increased values for the three dystrophic mouse strains when compared to the wild-type mice. An increased but not cumulative effect of the dystrophin absence and the α -DG glycosylation defect was observed in the double mutant *mdx/Large^{myd}* mouse: its muscle T2 was higher than the value observed in the *mdx* mouse, but it was not different from the *Large^{myd}* mouse. The increased muscle T2 in the dystrophic mice is in accordance with previous studies showing higher muscle T2 in the *mdx* mouse (Mathur et al., 2011; Walter et al., 2005), and in other mouse models of muscular dystrophies such as laminin-deficient mice (Tardif-de G ry et al., 2000) and the γ -sarcoglycan-null mice (Walter et al., 2005). Our NMR study in *Large^{myd}* and *mdx/Large^{myd}* mice extend the number of dystrophic mouse models where increased muscle T2 is observed, corroborating the hypothesis that even if no significant fat infiltration is observed in the MRI of murine models of muscle dystrophy, increased muscle T2 would be a common feature of the dystrophic muscle, both in patients and animal models with variable phenotype.

Muscle water T2 reflects the mobility of water molecules in the tissue. The loss of muscle proteins, the presence of infiltrated adipose and inflammatory cells, and the edema originated by inflammation and necrosis in the dystrophic muscle lead to alterations in the mobility of water molecules, and consequently can contribute to the T2 alterations (Kim et al., 2010). The absence of the dystrophin protein destabilizes the DGC and leads to increased membrane damage in the *mdx* mouse.

Sarcolemma disruption and increased cell permeability cause edema and extravasation of the sarcoplasmic content (Straub et al., 1997), with consequent altered mobility of water molecules and increased T2. Even if the *mdx* mouse has a mild phenotype, the membrane disruptions are present in higher proportion when compared to the more severely affected α -2 laminin-deficient mice, *dy/dy* and *dy^{2J}/dy^{2J}* (Straub et al., 1997). The same pathological disruption of the sarcolemma is observed in cardiac muscle cells from *Large^{myd}* mice (Kabaeva et al., 2011), and is possibly present also in the skeletal muscles from *Large^{myd}* and the double mutant *mdx/Large^{myd}* mice. Thus, sarcolemma disruption, in addition to the consequent necrosis and inflammatory infiltrates observed in areas with hyperintense signal in the MRI, could be more related to the increased muscle T2 in the three dystrophic mouse strains, than the overall phenotype.

The T2 determination based on two echoes at two different TEs has long been dismissed as inadequate and imprecise. This needs to be revised and our data bring more evidence pointing into that direction. When image signal-to-noise ratio is high, two-point determination is accurate, often more than CPMG echo trains. In practice, scanner imperfections but also RF propagation through tissues create B1 field deviations that are responsible for the generation of stimulated echoes that bias the T2 decay. Most often, the measured mono-exponential T2 with this sequence is longer than the true T2. The single echo collection as was performed here prevents the introduction of stimulated echos. While obsolete at first glance, the method used here is in reality as valid as and probably more accurate than more popular methods.

We are here dealing with mono-exponential T2, which is classically used to characterize global water T2 dynamics in a given tissue. Muscle T2 decay is in reality multi-exponential and can be exploited to determine tissue water compartments and exchanges, as shown by the work by Saab (Saab et al., 1999) and more recently by Araujo (Araujo et al., 2014). It requires different and very demanding experimental approaches, which are seldom used in practice. In that respect, standard multi-echo sequences do not allow better than the 2 echoes method to tackle this multi-compartment organization of tissue.

In the comparison between MRI and the histological analysis, appropriate co-localization of the distribution of alterations was observed in the three dystrophic

mouse strains, which is essential to validate the use of MRI as an outcome measure. In humans, a correlation between the degree of muscle involvement in MRI and the progression of dystrophic alterations in histological analysis was observed in DMD patients, but with MRI and muscle biopsy done in different muscles (Kinali et al., 2011). In the *mdx* mouse, our data comparing the histological analysis with the MRI in the same muscles showed that high intensity areas in muscle MRI were co-localized with variable dystrophic characteristics in the histological analysis, in accordance with the previous studies in this model (McIntosh et al., 1998b). Additionally, we extended for the first time this characterization for *Large^{myd}* and *mdx/Large^{myd}* dystrophic murine models, which showed a similar co-localization of alterations in the MRI versus the histological analysis. In all these dystrophic models the areas with increased muscle T2 in the MRI correlated spatially with several different histopathological alterations such as necrosis, inflammation, degeneration or regeneration foci. Thus, even if the increased muscle T2 could not differentiate individually each one of these pathological findings, the T2 maps reveal a disease process at a tissue level. Apart of the non-invasive nature, this MRI approach allows the evaluation of the dystrophic process along several muscles in the same exam, which is methodologically difficult considering the use of standard histological techniques.

Muscle T2 values were not correlated with the severity of the phenotype in the 3 dystrophic mouse strains, since the severely affected *Large^{myd}* mice showed similar values than both the mild *mdx* and severe *mdx/Large^{myd}* lineages. Notably, the major histological difference between these strains is fibrosis, which was not detectable with the MRI sequences used in this study. Connective tissue presents very short T2 values, being visualized only with appropriated pulse sequences such as Ultra Short Echo-time sequences (UTE) (Gatehouse and Bydder, 2003), which could not be used due to technical limitations. On the other hand, the MRI images showed clear different patterns of muscle signals. The muscle MRI was patchy in *mdx* mice, with delimited regions of increased MR signal distributed through the posterior limb muscles, both in the lower leg and in the calf images. The *Large^{myd}* mice, by its turn, showed a waxy pattern in the muscle MRI, with a general increase in the MR signal distributed homogeneously through the lower leg and thigh muscles. Finally, the

mdx/Large^{myd} mice showed generally a diffuse increase in the MR signal, like the *Large^{myd}* mice, but there were also hyperintense regions in the lower leg muscles, similar to what was observed in the *mdx* mice. After refining the muscle texture analysis with the evaluation of the co-occurrence matrix parameters entropy and contrast, it was possible to cluster the mice from different groups.

Changes in the muscle texture in small animals have already been reported in rats when comparing atrophic, regenerating and normal muscles (Mahmoud-Ghoneim et al., 2006). In the *mdx* model, a heterogeneous muscle signal was also observed in a variable degree according mouse's age, with a peak between the age of 5 and 17 weeks (Pratt et al., 2013). Additionally, texture parameters have been considered reliable biomarkers of disease progression in the GRMD dystrophic dog (Fan et al., 2014; Wang et al., 2013). Here we show the possibility of classifying murine models of muscle dystrophies with different phenotypes using quantitative NMR and texture analysis with prior knowledge. It is possible that the differences observed with our texture analysis were more evident due to the mice's age, since it was close to the described peak of muscle heterogeneity in the *mdx* model (Pratt et al., 2013). Even though, these results indicate that MRI when combined to texture analysis can provide a refined noninvasive identification of muscle alterations, not only between drastically different conditions but also when more subtle differences are present. This approach can be potentially transferred to human applications. In this case, a preliminary step would be to select the most discriminant combination of texture indices in muscle MRI from patients with known diagnosis. Then, the model could be validated by investigating in which category new patients would be classified in confront with genetic analysis.

Conclusions

While muscle mean T2 values were abnormal in all dystrophic muscle, and reflected the spatial distribution of different histopathological changes, they did not clearly distinguish the three different genotypes, nor were correlated to severity of the phenotype. On the other hand, texture analysis algorithms unambiguously separated muscles from *mdx*, *Large^{myd}* and *mdx/Large^{myd}* mice, reflecting the waxy versus patchy distribution of lesions in the different strains. Combined T2 maps and texture analysis provide a powerful non-invasive characterization of dystrophic muscles, even when performed at 2 tesla and derived from two single TEs measurements. Our findings have important implications to validate the use of MRI as an outcome measure in therapeutic protocols applied to mouse models of muscle dystrophies, with the possibility of direct applications in human translational research.

Supporting Information

S2.1. T2 calculation from two images at different echo times

The Bloch Equation for the spin-spin relaxation time (Equation 2.1) express the exponential decay of the sample magnetization as a function of the initial magnetization (M_0), the echo time (TE), and the spin-spin relaxation time of the sample (T2):

$$(2.1) \quad M = M_0 \exp\left(-\frac{TE}{T2}\right)$$

If two images are collected at different echo times, TE_1 and TE_2 , the ratio M_1/M_2 is given by:

$$(2.2) \quad \frac{M_1}{M_2} = \exp\left(-\frac{TE_1 - TE_2}{T2}\right)$$

The signal to noise ratio (SNR), corrected by the number of excitations used to compose the image (NEX), is proportional to the sample magnetization:

$$(2.3) \quad M \propto \frac{Signal}{Noise\sqrt{NEX}}$$

Combining The Equations 2.2 and 2.3, the T2 value can be estimated by (2.4):

$$(2.4) \quad T2 = \frac{\Delta TE}{\ln\left(\frac{SNR_1}{SNR_2}\right)}$$

The equation (2.4) was the basis of the MatLab routine designed to calculate the T2 maps. The noise was estimated by measuring the mean signal in a region of interest (ROI) placed in an empty area from the images.

S2.2. Features selected for Texture Analysis

Two parameters related to the co-occurrence matrix, contrast and entropy, were manually selected. The co-occurrence matrix is the second order histogram of the image, with the estimate of the joint probability $pdT(i,j)$ of two pixels, at distance d along a direction T , to have particular values i and j . MaZda calculates the co-occurrence matrix for up to 5 pixels of distance, and considering 4 directions (0° , 45° , 90° and 135°). The co-occurrence matrix parameters are therefore computed for $(d,0)$, $(0,d)$, (d,d) and $(d,-d)$, where d points to the distance between two pixels, which can take integer values from 1 to 5.

In the sequence (Table 2.2), 30 features were automatically selected by combining the maximization of the Fischer coefficients, the maximization of the mutual information between two selected features, the minimization of the classification error probability and minimization of the average correlation coefficients (F+PA+MI). The selected features are listed below, and they were used as input to Linear Discriminant Analysis (LDA).

Table 2.2. Features selected for texture analysis (F+PA+MI).

	Feature		Feature		Feature
1	S(0,4)Contrast	11	S(5,-5)Contrast	21	S(0,3)Entropy
2	S(4,0)Contrast	12	S(4,4)Entropy	22	S(2,2)Entropy
3	S(2,0)Entropy	13	S(4,4)Contrast	23	S(0,2)Entropy
4	S(2,-2)Entropy	14	S(5,0)Entropy	24	S(3,3)Entropy
5	S(5,-5)Entropy	15	S(0,5)Entropy	25	S(1,-1)Entropy
6	S(3,-3)Entropy	16	S(1,0)Contrast	26	S(1,1)Entropy
7	S(4,-4)Entropy	17	S(5,0)Contrast	27	S(0,1)Entropy
8	S(3,0)Entropy	18	S(5,5)Entropy	28	S(1,0)Entropy
9	S(0,3)Contrast	19	S(5,5)Contrast	29	S(0,2)Contrast
10	S(4,0)Entropy	20	S(0,4)Entropy	30	S(2,-2)Contrast

Complements to the manuscript

In addition to the measurements described in the manuscript, two verification steps were done to ensure the reliability of the results: (i) the validation of the 2-points T2 measurement by the comparison with results acquired with a standard multiecho sequence for T2 measurement; and (ii) the evaluation of post-mortem alterations on muscle T2.

Validation of the 2 points T2 measurements with a multiecho sequence

While usually the T2 values are estimated using multi-echo sequences, here, to avoid the influence of stimulated echoes, we proposed the estimation of muscle T2 with only 2 echo times. To validate this methodology, the muscle T2 values from 2 *C57Black/6* (wild-type) and 3 *mdx/Large^{myd}* mice were measured using a multiecho sequence, and the results were compared with the T2 values estimated with 2 echo-times.

The mice were scanned in a 3.0T MRI system (Intera Achieva, Philips Healthcare, Best, The Netherlands), with a 1H quadrature mouse volume coil (RAPID Biomedical GmbH, Germany), at LIM44, Faculty of Medicine, University of Sao Paulo. The sequence parameters were: TR= 1000 ms, 20 echo times, from 7.8 ms to 156 ms ($TE = 7.8 \cdot n$ ms, $n=1, \dots, 20$). The geometry parameters were: slice thickness 2 mm; resolution 0.2 x 0.2 mm/pixel; 4 slices; interslice space: 3 mm. The acquisition time was 24 minutes, and the total exam never exceeded 1 hour.

ROIs were designed in the gastrocnemius (Gastr) and tibialis anterior (TA) muscles in the slice corresponding to the lower leg. The T2 values were estimated fitting the exponential decay of the signal with the increase of the echo time. The first image ($TE = 7.8$ ms) was excluded from the fitting since it is not affected by stimulated echoes as the consecutive images. The last five echo times were excluded from the fitting, due to low signal to noise ratio observed for muscle.

The T2 values obtained were similar to those measured from the 2 echo-times T2 calculation, as shown in Table 2.3.

Table 2.3: Comparison of multiecho and 2 points T2 measurements in wild-type and dystrophic *mdx/Large^{myd}* mice.

Multi Echo T2 measurement (14 TEs)			2 points T2 measurement (2 TEs)		
wild-type N=2	TA	29.27 ± 1.33	wild-type N=13	TA	28.14 ± 1.28
	Gastr	30.63 ± 2.13		Gastr	28.43 ± 1.71
<i>mdx/Large^{myd}</i> N=3	TA	37.24 ± 1.87	<i>mdx/Large^{myd}</i> N=9	TA	37.26 ± 3.77
	Gastr	40.62 ± 1.98		Gastr	37.09 ± 2.84

The values obtained with the two methods were similar, indicating that the estimative of the T2 values from two images acquired at different echo times is a reliable measurement in living mice.

Post-mortem changes in the T2 values

The double mutant *mdx/Large^{myd}* mice were very sensitive to the anesthetic: from 16 *mdx/Large^{myd}* mice analyzed, 6 died during the measurements due to the anesthesia. 2 *Large^{myd}*, 1 *mdx* and 1 *C57Bl/6* (wild-type) mice also died during the measurements, under anesthesia. The T2 values obtained from the mice that died during the experiments tended to be higher than the values obtained from living mice from the same lineage. To evaluate the muscle T2 changes after death, 2 *mdx* and 1 wild-type mice were imaged under anesthesia. Immediately after the end of the acquisition, mice were killed by cervical dislocation and MRI was repeated. Table 2.4 shows the results of these measurements.

The post-mortem T2 values were increased for the three mice and all muscle groups, with T2 values increasing from 6 to 31%. The T2 standard deviation was increased for the three mice for the calf muscles, from 7 to 60%. Nevertheless, for the thigh muscles, the T2 standard deviation was increased in the wild-type and in one *mdx* (*Mdx*#71) mouse, from 6 to 37 %, while it decreased around 10% for one *mdx*

mouse (*Mdx*#70). The high variability observed in the post-mortem T2 measurements could be related to osmotic changes due to the stopped activity of ionic pumps. Thus, the exams from mice that died during the image acquisition were discarded from muscle T2 and texture analyses in the manuscript.

Table 2.4: Post-mortem muscle T2 changes values from 1 *C57Bl/6-WT* and 2 *mdx* mice.

Mouse		Lower Leg		Thigh	
		Posterior	Anterior	Lateral	Medial
wild-type	Alive	29.91 \pm 5.86	30.03 \pm 6.90	30.97 \pm 5.28	31.84 \pm 6.34
	Dead	34.89 \pm 7.18	34.80 \pm 7.78	34.12 \pm 6.87	33.85 \pm 6.74
	Dead/Alive	1.17 \pm 1.23	1.16 \pm 1.28	1.10 \pm 1.30	1.06 \pm 1.06
Mdx #70	Alive	33.36 \pm 7.97	31.05 \pm 8.86	43.05 \pm 17.88	35.27 \pm 8.27
	Dead	36.71 \pm 8.75	37.96 \pm 9.47	46.91 \pm 15.83	38.16 \pm 7.43
	Dead/Alive	1.10 \pm 1.10	1.22 \pm 1.07	1.09 \pm 0.89	1.08 \pm 0.90
Mdx #71	Alive	31.24 \pm 7.39	30.51 \pm 6.02	30.75 \pm 5.98	31.57 \pm 5.73
	Dead	37.36 \pm 8.19	39.93 \pm 9.63	37.07 \pm 7.40	39.03 \pm 7.82
	Dead/Alive	1.20 \pm 1.11	1.31 \pm 1.60	1.21 \pm 1.24	1.24 \pm 1.37

Chapter 3

Structural and functional alterations of
skeletal muscle microvascular network in
dystrophin-deficient *mdx* mice

Chapter 3. Structural and functional alterations of skeletal muscle microvascular network in dystrophin-deficient *mdx* mice

This NMR study is shared with the PhD thesis of Claire Latroche, under the supervision of Gregory Jouvion, Fabrice Chrétien (Institut Pasteur, Human histopathology and animal models, Infection and epidemiology Department, Paris, France) and Bénédicte Chazaud (INSERM U1016, Institut Cochin, Paris, France). NMR study was done at the NMR Laboratory of the Myology Institute, Paris, France, and is shared between this thesis and Claire Latroche's thesis. All the additional analyses presented here were done by Claire Latroche, and are presented to support the discussion of the NMR results.

This chapter has been submitted for publication in the American Journal of Pathology in November 2014, and accepted for publication after revision in May 2015.

Authors: Claire Latroche, Béatrice Matot, Aurea Martins-Bach, David Briand, Bénédicte Chazaud, Claire Wary, Pierre G. Carlier, Fabrice Chrétien & Gregory Jouvion

List of abbreviations:

ADP: Adenosine diphosphate, ASL: Arterial spin labelling, ATP: Adenosine triphosphate, CFPE: capillary to fiber perimeter exchange, DMD: Duchenne muscular dystrophy, GFP: green fluorescent protein, HE: haematoxylin and eosin, NMR: nuclear magnetic resonance, NOS: nitric oxide synthase, PCr: Phosphocreatine, Pi: phosphate inorganic, SATIR: SATuration-Inversion Recovery, VEGF/R: vascular endothelial growth factor/Receptor

Abstract

Duchenne Muscular Dystrophy (DMD) is a progressive neuromuscular disease, caused by an absence of dystrophin, inevitably leading to death. Although muscle lesions are well characterised, blood vessel alterations that would have major impact on muscle regeneration remain poorly understood. Our aim was to elucidate alterations of the vascular network organisation, taking advantage of Flk1^{GFP/+} crossed with *mdx* mice (model for human DMD where all blood vessels express GFP), and functional repercussions using *in vivo* nuclear magnetic resonance (NMR), combining arterial spin labelling imaging of perfusion, and ³¹P-spectroscopy of phosphocreatine kinetics. For the first time, our study focused on old (12 month-old) *mdx* mice, displaying marked chronic muscle lesions, very similar to the lesions observed in human DMD, in comparison to young-adult (3 month-old) *mdx* mice displaying only mild muscle lesions with no fibrosis. Using an original approach combining specific animal model, state of the art histology/morphometry techniques, and functional NMR, we demonstrated (i) that the microvascular system is normal in young-adult in contrast to old *mdx* mice, displaying marked capillary alterations, and (ii) functional repercussions on muscle perfusion and bioenergetics after a hypoxic stress, that vary depending on stage of pathology. This original approach clarifies disease evolution and paves the way for setting up new diagnostic markers or therapeutic strategies.

Introduction

Duchenne muscular dystrophy (DMD) is the most frequent genetic neuromuscular disorder affecting 1:3500 school-age boys worldwide. This X-linked muscle disease is characterised by progressive skeletal muscle weakness and cardiomyopathy, leading to premature death generally because of respiratory and/or cardiac failure. The cause of DMD is the absence of dystrophin, a key component of the dystrophin-associated protein complex involved in the linkage between myofiber cytoskeleton and extracellular matrix. When linkage is disrupted, muscle fibers develop normally but are more susceptible to damage due to mechanical stretch. Despite presence of satellite cells and successive regeneration attempts, myofibers undergo necrosis and are eventually replaced by connective and adipose tissue (De Paepe and De Bleecker, 2013).

Muscle lesions in DMD have been widely investigated, with studies focussing principally on myofibers and/or satellite cells. Although (i) skeletal muscle is one of the most vascularised tissues, (ii) endothelial cells are essential in muscle regeneration process, and (iii) dystrophin is expressed in endothelial/smooth muscle cells, disease impact on blood vessels and effect of blood vessel alteration in disease expression remain poorly understood. In recent years, interest in DMD vascular network has increased with primary focus on vasculature-related therapeutic strategies (Ennen et al., 2013) such as methods to increase vasculature by modulating VEGF/VEGFR pathways (Shimizu-Motohashi and Asakura, 2014). These strategies were initially based on: (i) observation of “grouped necrosis” in muscles of DMD patients, *i.e.* simultaneous necrosis of contiguous myofibers, suggesting local failure in capillary blood supply and muscle ischemic necrosis (Engel and Hawley, 1977), and (ii) membrane-associated nitric oxide synthase (NOS) deficiency in dystrophin-deficient muscle (Rando, 2001b). The hypothesis of an ischemic process has been strongly discussed, as other studies could not detect any vascular bed abnormality in DMD either morphologically using electron microscopy (Koehler, 1977) or physiologically by studying muscle blood flow (Bradley et al., 1975; Gudrun et al., 1975; Leinonen et al., 1979). More recent studies carried out in DMD patients confronted blood vessel alteration with tissue fibrosis. They suggested that endomysial fibrosis plays an

essential role, causing an increase in capillary-to-myofiber distances, which impairs both muscle fiber mechanical function and gas exchanges (Desguerre et al., 2009). Moreover, increased distances between capillaries and myofibers could potentially impede their reciprocal stimulation by soluble factors secreted during muscle repair (Christov et al., 2007).

Rare studies addressed the relevance of muscle vascular network in dystrophinopathy pathophysiology in animal models, focusing on muscle vascular density and characterisation of a possible hypoxic condition in dystrophic muscle. Part of these studies pointed to a decreased vascular density and an impaired angiogenesis in 6 week- to 6 month-old *mdx* mice (Landisch et al., 2008; Loufrani et al., 2004; Matsakas et al., 2013), the dystrophin-deficient murine model of human DMD. However, contradictory results were also published in *mdx* mice, showing a higher hindlimb perfusion one week after femoral artery dissection and significant increase in arteriole length density in 2 month-old animals (Straino et al., 2004). These discrepancies could be related in part to the effect of aging in disease progression; age appears to be an important parameter to consider when studying vascular changes (Shimizu-Motohashi and Asakura, 2014). Thus, involvement of blood vessels in the pathogenesis of dystrophy is still not completely understood.

In the present study, we investigated both structural organisation and *in vivo* function of vascular system in young-adult (3 month-old) *mdx* mice, displaying only moderate subacute muscle lesions with no fibrosis, and old (12 month-old) *mdx* mice, displaying marked muscle lesions with persistent inflammation and fibrosis (Grounds et al., 2008), more relevant for the study of DMD pathophysiology in human. We used complementary morphological approaches based on genetically-modified mice that allowed for the first time to reconstruct the 3-dimensional microvascular network in *mdx* mouse. These were confronted to innovative histological techniques and dynamic and non-invasive multiparametric and functional nuclear magnetic resonance (NMR).

Materials and Methods

Mice

C57Bl/6J control mice were obtained from Charles River Laboratory (l'Arbresle, France), *mdx-4Cv* mice, model for human DMD, were kindly provided by Pr. Gherardi (Hôpital Henri Mondor, France), Flk-1^{GFP/+} mice, in which green fluorescent protein (GFP) is targeted in vascular endothelial growth factor (VEGF) receptor-2 gene locus, exhibiting a bright GFP signal in all endothelial cells, were kindly provided by A. Medvinsky (Institute for Stem Cell Research, University of Edinburgh, UK), and *mdx-4Cv::Flk-1^{GFP/+}* mice were obtained by crossing *mdx-4Cv* with Flk-1^{GFP/+} mice. Male animals were used: young-adult (3 month-old) or old (12 month-old).

Animals were housed in animal facilities of the Institut Pasteur licensed by the French Ministry of Agriculture and complying with European Union regulations. Protocols were approved by the Institut Pasteur Animal Experimentation Ethics Committee (01332.01).

Microvascular network organisation in three dimensions

Young and old Flk-1^{GFP/+} and *mdx-4Cv::Flk-1^{GFP/+}* mice were anesthetised with isoflurane inhalation (Forene, Abbott, Rungis, France) and killed by cervical dislocation. *Gastrocnemius* muscles were removed and imaging of vascular network was carried out in two conditions: thick cryo-sections or whole muscle. *Gastrocnemius* muscle was snap frozen in liquid nitrogen-cooled isopentane before cryosectioning (100µm-thick sections). Confocal acquisitions were performed using a spinning disk microscope (Leica, Wetzlar, Germany), laser femto-second was used: Chameleon Ultra, 20x/0.7 and 40x/0.75 objectives and a CoolSnap HQ2 camera. Optical slices were taken every 0.5 or 0.3µm interval along the z-axis (80µm). For whole muscle conditions, images of *Gastrocnemius* blood vessels were obtained from

the entire muscle using multi-photon scanner resonant confocal Leica TCS-SP5 with 20x/0.95 objective. Optical slices were taken every 0.5 μ m along the z-axis.

Histology

Gastrocnemius muscles were collected from mice after NMR experiments, snap frozen in liquid nitrogen-cooled isopentane and kept at -80°C . Six different levels of 7 μ m-thick sections were cut and stained with hematoxylin-eosin (HE) to describe histopathological modifications of muscle tissue, and Sirius red for visualisation of collagen. For immunohistochemistry analyses, muscle cryosections were incubated with anti-CD31 (Pharmingen) and anti-laminin (Sigma) antibodies, overnight at 4°C , revealed by cy3- or TRITC-labeled secondary antibodies (Jackson ImmunoResearch Laboratories).

Morphometric analysis

Two-dimension analysis was performed to evaluate distribution of muscle fiber diameter, percentage of centro- or peri-nucleated fibers, capillary count and distribution around each myofiber using ImageJ (NIH, Bethesda, USA) and NIS-Element (Nikon) softwares. At least 200 fibers were considered for each muscle.

Three-dimensional analysis was performed to evaluate organisation of vascular network. For each muscle, 10z-stack image reconstructions were achieved on 80 to 150 μ m-thick frozen sections. Analysis was carried out using IMARIS (ImarisBitplane, Zurich, Switzerland) software (quantification of vessel density, tortuosity, volume, anastomose count and distance between capillaries).

Nuclear Magnetic Resonance analysis

NMR experiments were performed on: 3 month-old *mdx*-4Cv (n=6) and control C57Bl/6J (n=9) and on 12 month-old *mdx*-4Cv (n=5) and control C57Bl/6J (n=7).

Hyperaemic response paradigm

To highlight differences between normal and altered muscles we classically applied a stress to increase the global need for perfusion. Ischemia-reperfusion stress was applied to the mouse left hindlimb which provokes maximal vasodilatation and limited resistance of arteries/arterioles (Bertoldi et al., 2008) just after tourniquet release.

In practice, anaesthesia was induced with 4% isoflurane delivered in 1.5L/min air and maintained with 1.75% isoflurane. During experiments, a water heating pad ensured a constant temperature of 37°C and breathing was monitored. After a 24min NMR acquisition at rest (baseline), ischemia of the leg was induced by occlusion of femoral artery by two surgical threads placed around the thigh and pulled tight by application of a weight (Bertoldi et al., 2008). After 30min of ischemia, the weight was instantly removed, inducing a hyperaemic response, which was monitored over the next 30min. During whole protocol, dynamic acquisitions of NMR scans of interleaved perfusion imaging and ^{31}P -spectroscopy (^{31}P -NMRS) were collected.

Multiparametric functional NMR (mpf-NMR) acquisitions

In vivo NMR experiments were conducted in a 4Tesla Biospec system equipped with a 20cm diameter 200mT.m⁻¹ gradient insert (BrukerBioSpin MRI GmbH, Ettlingen, Germany). Mice were placed supine in a 6cm diameter, 12cm length volume transmitter ^1H coil for whole-body signal excitation. An actively decoupled 2cm diameter surface ^1H coil, positioned below the left calf, was used for image signal reception. Muscle metabolites were probed by a 10mm ^{31}P saddle-shaped coil placed around the left leg.

As described in detail elsewhere (Baligand et al., 2009; Bertoldi et al., 2008), Arterial Spin Labelling (ASL)-NMR imaging and ^{31}P -NMRS acquisitions were

interleaved using the dedicated Bruker MultiScanControl software (BrukerBioSpin GmbH) in order to follow simultaneously and non-invasively: (i) muscle perfusion signal by SATuration-Inversion Recovery (SATIR) (time resolution: 10sec), and (ii) mitochondrial activity by dynamic ^{31}P -NMRS (time resolution: 2.5sec). In brief, ASL imaging is based on non-invasive alternate magnetic tagging of blood water spins to provide endogenous markers of muscle perfusion, measured in regions of interest (ROI) drawn in posterior compartment of the leg. Muscle bioenergetics and pH were assessed from ratios of energetic phosphates measurable by ^{31}P -NMRS at rest, *in vivo* mitochondrial oxidative capacity was directly assessed from the rate of creatine rephosphorylation at the end of ischemia, and intramuscular pH was calculated from chemical shift between phosphocreatine (PCr) and inorganic phosphate (Pi). A minimum of 50% PCr depletion at the end of ischemia was necessary to reliably measure dynamics for PCr recovery, and examinations which did not reach this threshold were rejected.

Statistics

Perfusion data were analysed by two-way ANOVA and repeated measurements ANOVA, followed by Bonferroni comparison of means when necessary. Analyses were performed with NCSS-2007 software (Kaysville, USA). Group comparisons for phosphorus spectroscopy analysis were performed using Mann-Whitney test.

Statistical analysis of histological data was performed with GraphPad-Prism software (La Jolla, USA). Fiber diameter repartition was evaluated by a chi-square test followed by a multi-t-test corrected for multiple comparisons using Holm-Sidak method. Same multi-t-test was used to evaluate capillary count/fiber repartition.

Statistical significance was taken at $p < 0.05$ and p-values indicated on figures are * $p < 0.05$, ** $p < 0.01$, and *** $p < 0.001$. Numerical NMR and histological data are reported as mean \pm SD.

Results

Normal microvascular network organisation in young-adult Flk1^{GFP/+}::mdx mouse.

Polyphasic subacute lesions, characterised by small inflammatory infiltrates and centrally nucleated fibers, were observed in *Gastrocnemius* muscle (Figure 3.1 A-B). Surprisingly, these lesions had no impact on blood microvascular network organisation; in both Flk1^{GFP/+} and Flk1^{GFP/+}::mdx mice, microvascular network was well organised with straight capillaries located along myofibers, parallel to each other with few anastomoses oriented perpendicularly to capillaries (Figure 3.1 C-F). Capillary diameter, measured using diameter of endothelial cell fluorescence, was similar in both groups (13-14µm), as well as anastomose count (1,200-1,650 anastomoses/mm³) (Figure 3.1 G-H).

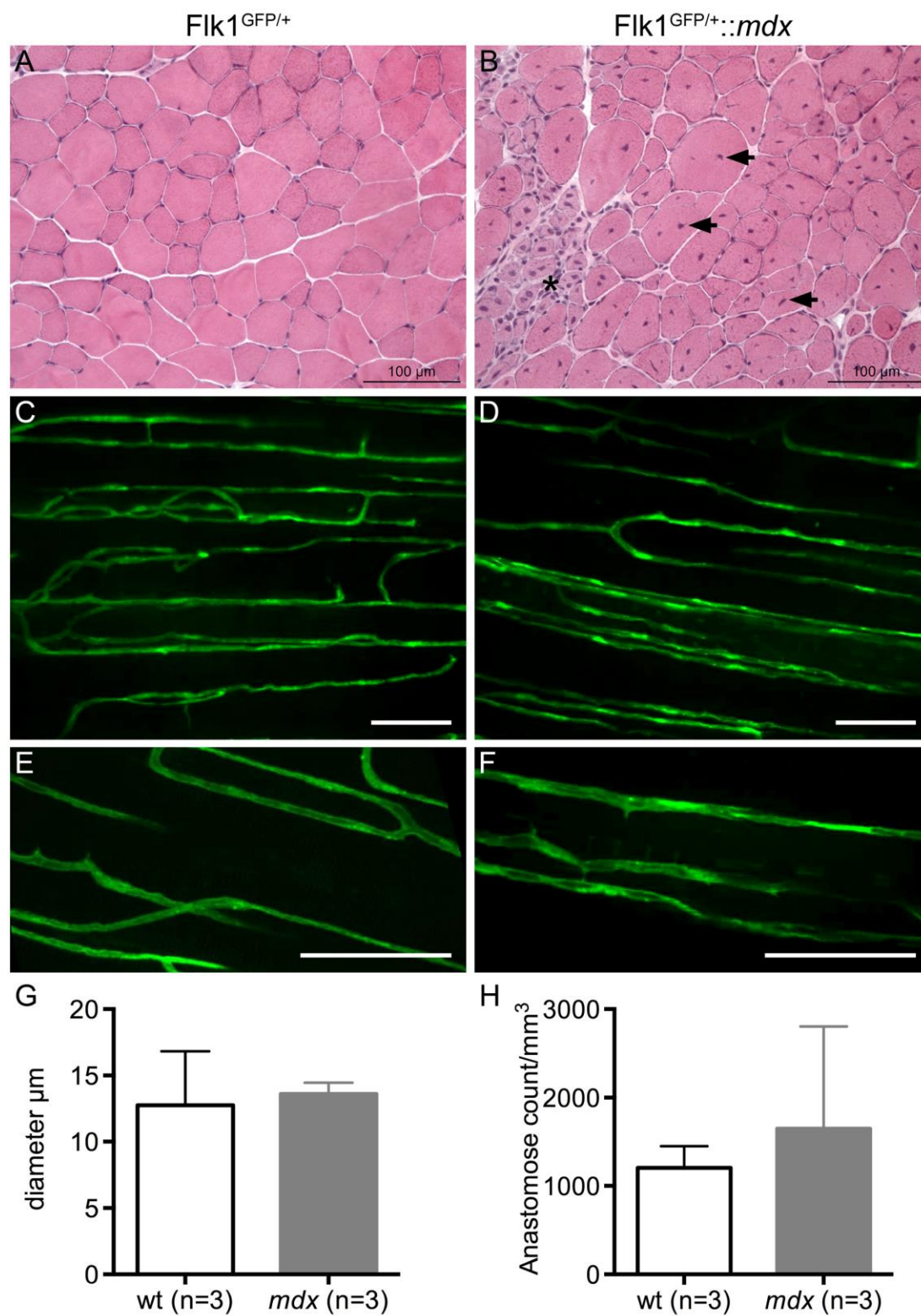


Figure 3.1. Normal microvascular network organisation in 3 month-old *mdx* mice. In contrast to wild-type mice (A), *mdx* mice (B) display subacute lesions in *Gastrocnemius* muscle, characterised by small inflammatory infiltrates (star)

associated with regenerated myofibers displaying central nuclei (arrows) (HE staining). Microvessel 3D organisation of Flk1^{GFP/+} (C, E) and Flk1^{GFP/+::mdx} (D, F) mice: normal blood capillary organisation, with capillaries regularly scattered along myofibers (C-F) (Scale bars: 50µm). Morphometric analyses revealed similar diameter (G) and anastomose count/mm³ (H) between capillaries from wild-type and *mdx* mice.

Immunofluorescence analyses did not detect any significant difference between young-adult wild-type and *mdx* mice (Figure 3.2). Both muscles displayed the same myofiber cross-section diameter, fiber size distribution, and “capillarization”, quantified by capillary count per fiber. Collectively, these results highlighted a normal capillary organisation in muscles of both groups.

Capillary-to-fiber perimeter exchange index (CFPE) has been used to calculate the contact surface area between capillaries and myofibers. It provides an indirect quantitative criterion to evaluate movement of oxygen from capillaries to muscle fibers (Hepple, 1997). CFPE index was not affected in young-adult *mdx* mice (Figure 3.2 F).

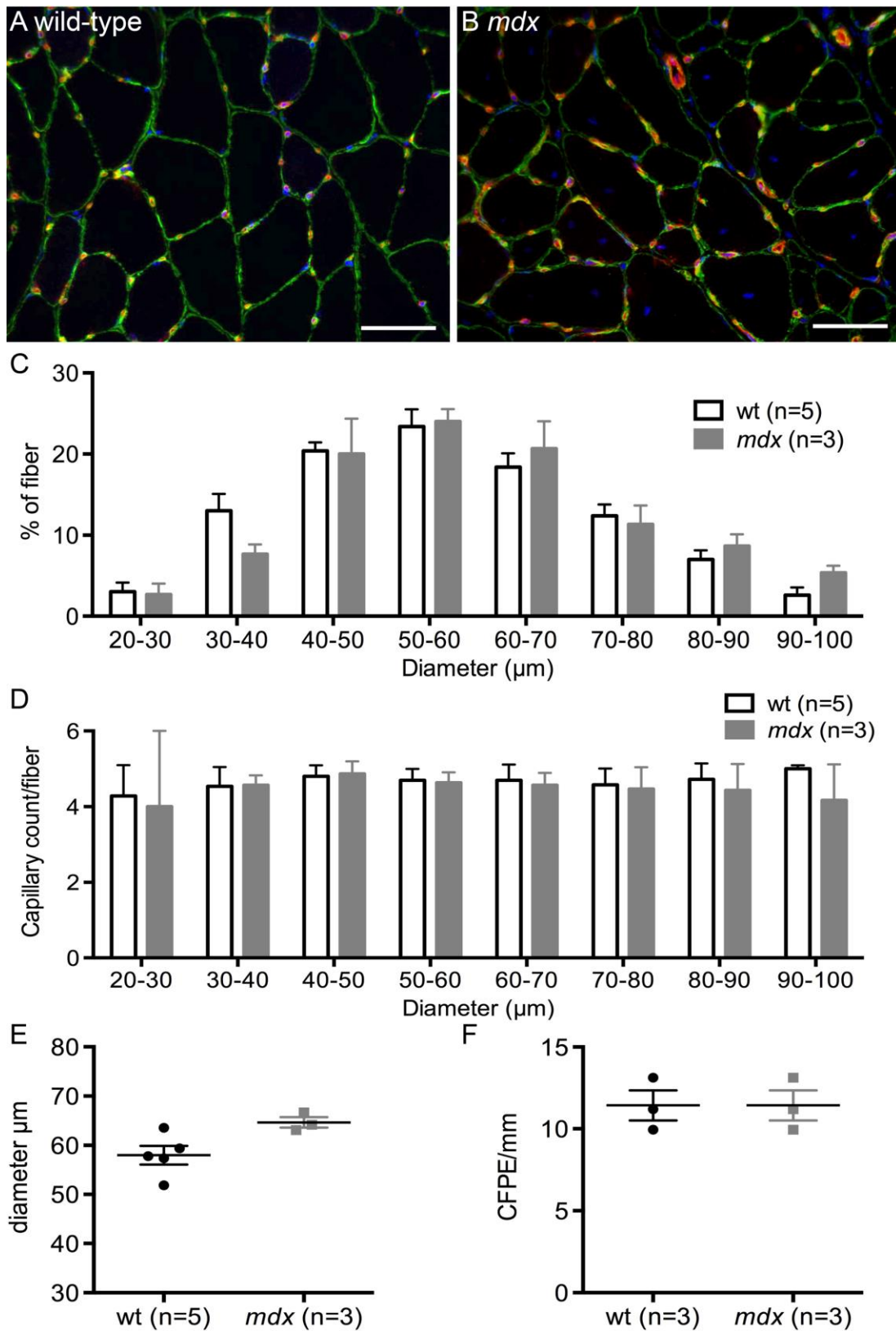


Figure 3.2. Capillary morphometry in 3 month-old mice. Young-adult wild-type (n=5) and *mdx* (n=3) mice display similar: capillary distribution in *Gastrocnemius*

muscle (A, B) (laminin-FITC and CD31-TRITC immunohistochemistry to label basal lamina (green) and blood vessels (red); Scale bar: 50 μ m), fiber size repartition (C), capillary count per fiber (D), capillary diameter (E), and capillary to fiber perimeter exchange index (CFPE).

Muscle blood perfusion is modified in young-adult mdx mice.

Despite similar microvascular organisation, profiles of reactive hyperaemia were significantly different in *mdx* (n=6) and wild-type (wt) (n=9) mice (Figure 3.3 A, $p < 10^{-6}$ with ANOVA). The release of ischemia provoked an instantaneous increase of perfusion, which was lower in wt mice (*mdx*: 78.7 ± 27.1 ml/min/100g; wt: 41.3 ± 32.3 ml/min/100g, 20s post-release). In wt mice, this first perfusion peak was followed by a drop to reach a plateau around a value of 26.6 ± 9.2 ml/min/100g peaking at 270s post-ischemia. In contrast, *mdx* muscle perfusion slightly increased to a mean perfusion value of 84.8 ± 24.8 ml/min/100g at 300s post-ischemia and reduced to 26.3 ± 25.9 ml/min/100g only 850s after stress release (Figure 3.3 A). Moreover, the global volume repaid after ischemia was significantly higher in *mdx* mice (wt: 474.3 ± 216.3 ml/100g; *mdx*: 1017 ± 369.2 ml/100g, $p < 0.05$). The response to ischemic stress was therefore different and enhanced in young-adult *mdx* mice while no morphological modification of microvessels was detected.

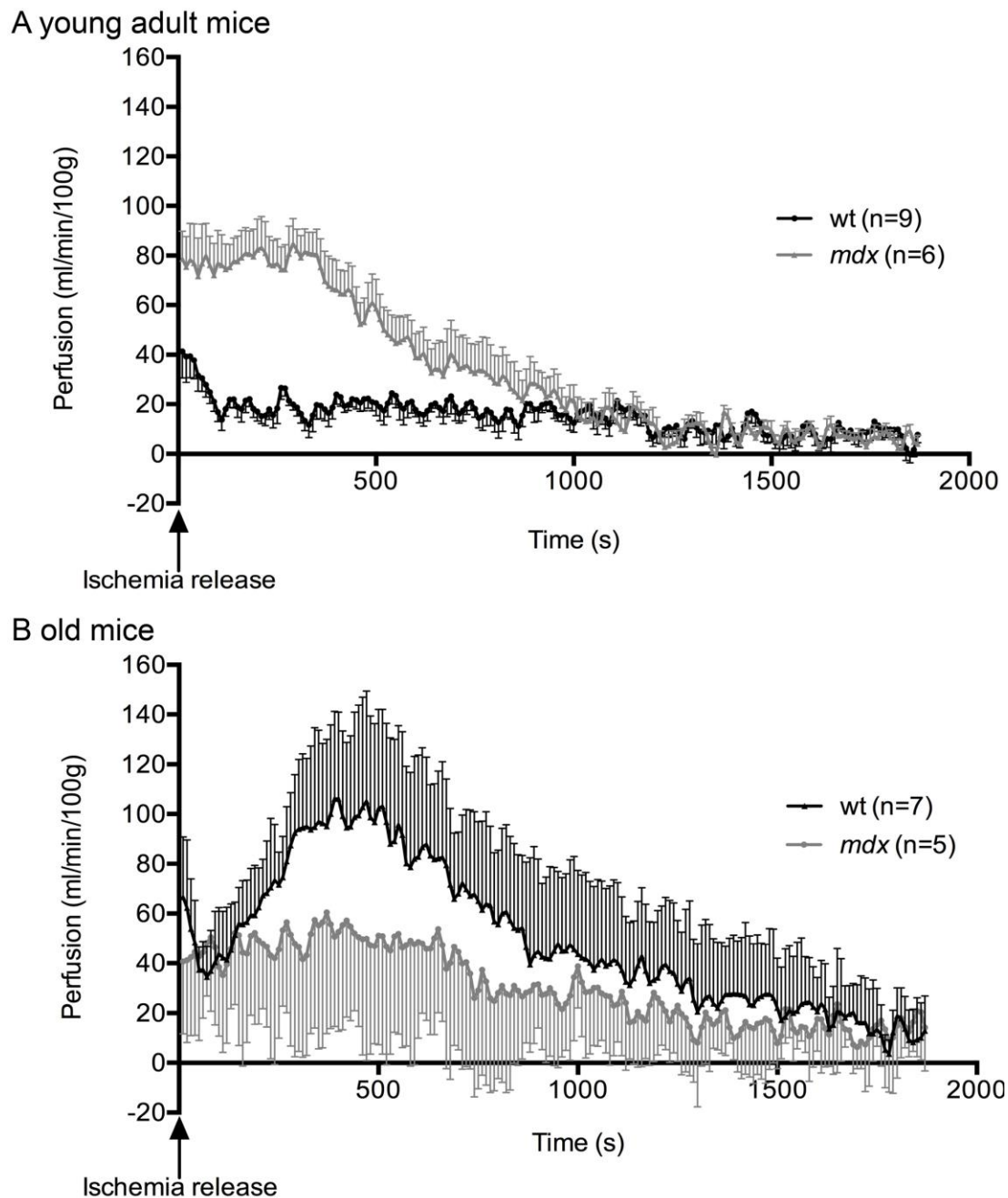


Figure 3.3. Muscle blood perfusion during ischemia-reperfusion. After release of ischemia, a rapid and important increase in perfusion is detected. (A) Different profiles of perfusion were obtained in young-adult mice: total perfusion was higher in *mdx* mice and a first “peak” of perfusion followed by a rapid decrease in muscle perfusion was only detected in wild-type mice. (B) A first “peak”, similar to what was observed in young-adult wild-type mice, was also observed in 12 month-old control animals. This first “peak” was not present in *mdx* mice, which also displayed a

reduced perfusion, with a maximum perfusion equivalent to half the value observed in wild-type mice during the hyperaemia phase. As the release of ischemia induced movements of the leg, images affected by these movement artefacts were removed from analysis of muscle perfusion.

Muscle bioenergetics in young-adult mice (Table 3.1)

At rest, *mdx* mice displayed a slightly higher Pi/PCr ratio compared to wt, which reflects an increase in ADP concentration in dystrophic mice. In addition, a lower PCr/ γ ATP ratio was observed in *mdx* mice, reflecting a decrease in metabolically functional muscle tissue.

The 30min ischemic stress induced a higher Pi/PCr ratio in *mdx* mice while PCr depletion tended to be accelerated compared to wt (*mdx*: Δ PCr = 65 ± 9 %; wt: Δ PCr = 58 ± 6 %; $p=0.09$).

At reactive hyperaemia, release revealed a significant acceleration of PCr resynthesis rate in *mdx* mice compared to wt, reflecting higher mitochondrial ATP production in the *mdx*.

Table 3.1. Energetic metabolism analysis from ^{31}P -spectroscopy in young-adult mice.

	wt (n=9)	<i>mdx</i> (n=6)
Δ PCr (%)	58 ± 6	65 ± 9
τ PCr (s)	118 ± 34	$76 \pm 34^*$
pH at rest (pH _{rest})	7.20 ± 0.04	7.17 ± 0.03
pH end ischemia (pH _{end})	7.00 ± 0.08	6.98 ± 0.03
Pi/PCr at rest (Pi/PCr _{rest})	0.08 ± 0.03	$0.10 \pm 0.01^*$
Pi/PCr end ischemia (Pi/PCr _{end})	0.93 ± 0.25	$1.71 \pm 0.52^*$
PCr/ATP γ at rest (PCr/ATP γ_{rest})	3.39 ± 0.25	$3.01 \pm 0.27^*$
PCr/ATP γ end ischemia (PCr/ATP γ_{end})	1.80 ± 0.62	1.39 ± 0.51

Ischemia stress was sufficient as the mean depletion of phosphocreatine (PCr) for wt and *mdx* mice was above 50%. Pi/PCr at rest and after ischemia were higher in *mdx* compared to wt mice while PCr/ATP γ at rest was lower (* $p<0.05$).

However, contrarily to wt, combined ^{31}P -NMRS and perfusion results showed a very tight correlation between time of rephosphorylation τPCr and various parameters reflecting perfusion: maximum perfusion ($R^2= 0.66$, $p<0.05$), time-perfusion integrals ($R^2> 0.98$, $p<0.001$ until 50s; $R^2>0.93$, $p<0.01$ until 150s) (Figure 3.4). In wt, none of the correlations between τPCr and perfusion were significant.

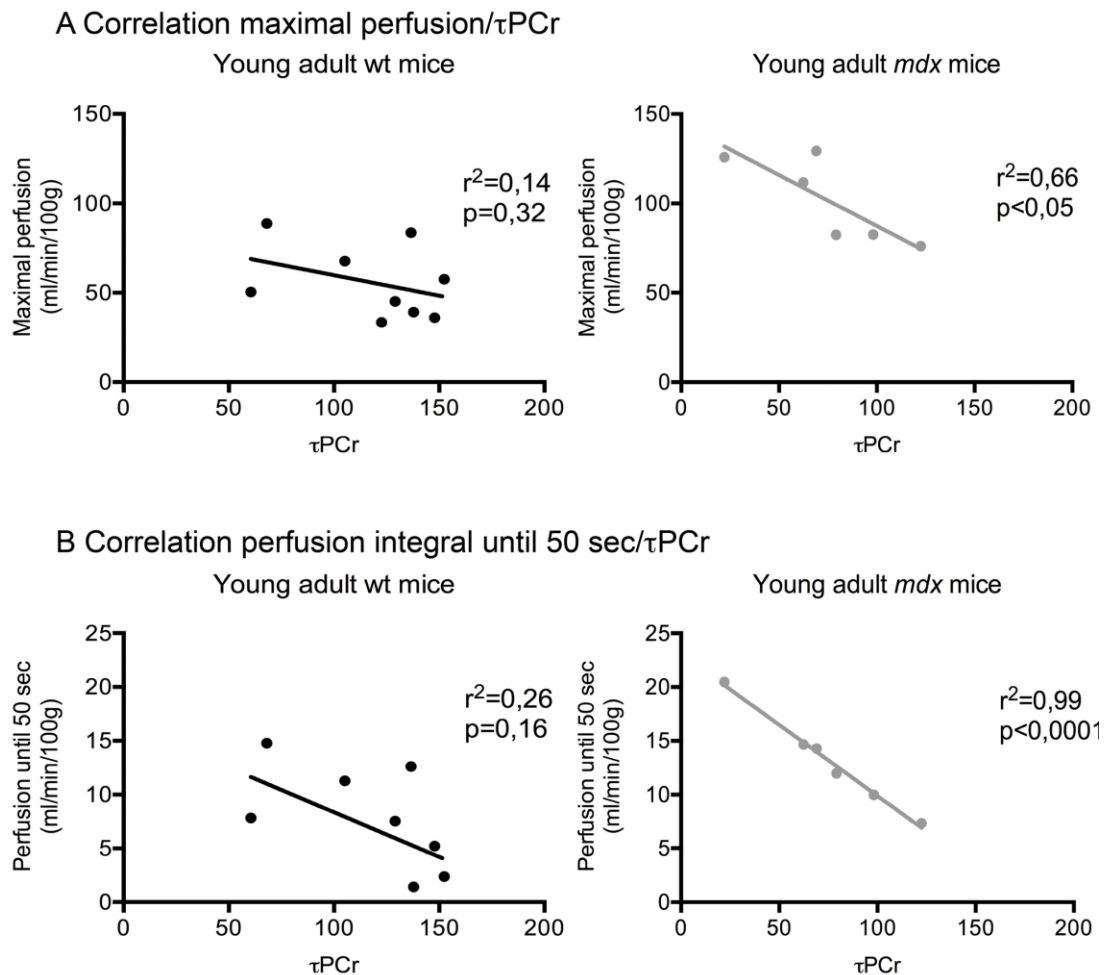


Figure 3.4. Correlation between perfusion and time of creatine rephosphorylation (τPCr) in 3 month-old mice. Correlation between τPCr and maximal perfusion (A) or time-perfusion integrals until 50s (B) is significant in *mdx* mice ($p<0.05$ and $p<0.0001$, respectively). In wt, none of the correlations were significant.

In summary, phosphate metabolism was accelerated during ischemia in 3 month-old *mdx* mice. At recovery, mitochondrial oxidative rephosphorylation was unexpectedly faster and perfusion was increased in comparison to age-matched control mice. Moreover, perfusion in *mdx* was directly related to mitochondrial ATP production. This is unlike normal healthy case where a luxury perfusion is observed and is neither limiting nor correlated to τ PCr.

Alteration of microvascular network organisation in old Flk1^{GFP/+}::mdx mouse

Old *mdx* mice displayed marked histological lesions; some already observed in young-adult as anisocytosis or centrally nucleated myofibers, others included persistence of chronic inflammation, and presence of endomysial/perimysial fibrosis (Figure 3.5 A-D). The microvascular network was as well organised in old Flk1^{GFP/+} as in young-adult mice (Figure 3.5 E, G). In contrast, Flk1^{GFP/+}::*mdx* mice displayed significant alterations, characterised by a marked increase in tortuosity and irregular scattering of capillaries (Figure 3.5 F, H). Capillary diameter was similar in both groups (12 μ m, Figure 3.5 I), but we identified a higher anastomose count, from more than 50,000 anastomoses/mm³ for Flk1^{GFP/+}::*mdx* mice to less than 1,000 anastomoses/mm³ for control Flk1^{GFP/+} (p<0.01) (Figure 3.5 J). Collectively, these results pointed to an anarchic blood vessel organisation in this context of dystrophinopathy.

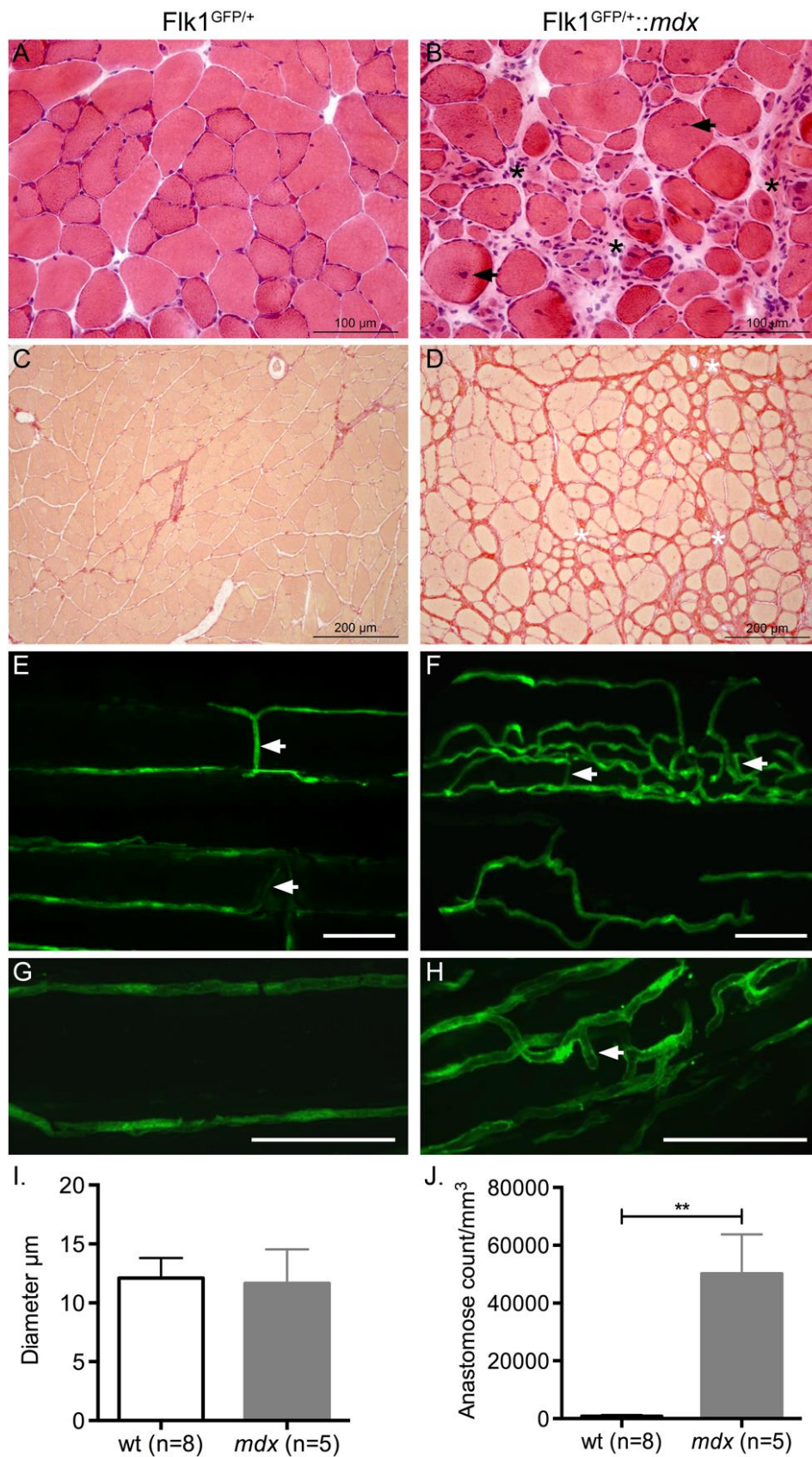


Figure 3.5. Alteration of microvascular network in 12 month-old *mdx* mice.

Twelve month-old wild-type mice display histologically normal muscles (A), with no

fibrosis (C), and regularly scattered capillaries along myofibers, with few anastomoses (E, G, J). In contrast, 12 month-old *mdx* mice display chronic histological lesions (B), characterised by multifocal inflammatory infiltrates (mostly macrophages), included in endomysial collagen tissue (fibrosis; stars), associated with a marked variation in myofiber size (anisocytosis) and the presence of atrophic and regenerating myofibers displaying centrally-located nuclei (arrows). Sirius red staining and fluorescence microscopy reveal a moderate to marked endomysial fibrosis (D) and microvascular network alterations (F,H), characterised by irregularly scattered tortuous capillaries (Scale bars: 50µm). Even if capillary diameter is similar between *mdx* and wild-type mice (I), a clear increase in anastomose count/mm³ is detected for old *mdx* mice (J). A, B: HE staining. C, D: Sirius red staining (specific for collagen staining). **p<0.01.

Immunofluorescence analyses showed that (i) myofiber cross-section mean diameter was smaller in *mdx* mice (*mdx*: 47.4±4.2 µm; wt: 61.2±3.9 µm; p<0.001) (Figure 3.6 C), (ii) the smaller myofibers (<50µm) were clearly under-vascularised (Figure 3.6 E), (iii) perinucleated (Figure 3.6 G), and (iv) represented almost 60% of total muscle fibers in *mdx* mice in contrast to 35% in controls (Figure 3.6 D). These data suggested either a progressive degradation of tissue with no maintenance of microvascular network with time or a defect of neo-angiogenesis. The CFPE was not affected in old mice (Figure 3.6 F). Collectively, these results pointed to severe alterations of microvessel organisation, especially around small/atrophic myofibers, suggesting chronic alteration of endothelial-myogenic cell interface.

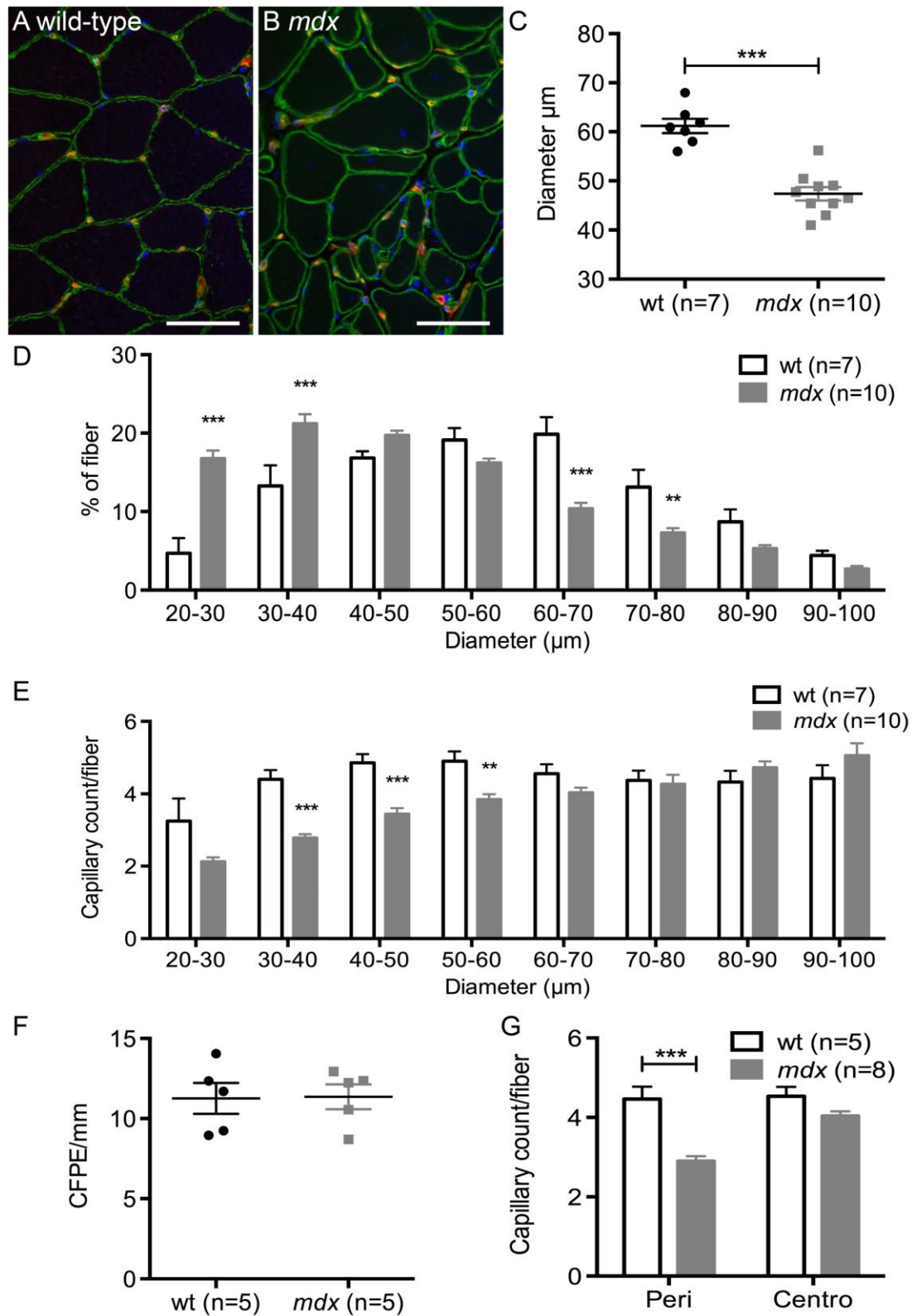


Figure 3.6. Twelve month-old *mdx* mice display atrophic myofibers with low capillarisation. Anisocytosis is more pronounced in old *mdx* mice, with the presence of small atrophic myofibers (A-C) (Laminin-FITC and CD31-TRITC

immunohistochemistry; Scale bars: 50µm). Capillary count per fiber highlights that small myofibers with a diameter up to 60µm display less capillaries at their periphery (E). These atrophic myofibers represent more than 60% of the total myofibers in *mdx* mice (D). The distance between capillaries and myofibers, calculated using the capillary to fiber perimeter exchange index (CFPE) is similar in both groups (F). Small myofibers with low capillarisation are mostly perinucleated myofibers (G) (*p<0.05, **p<0.01, ***p<0.001).

Alteration of muscle perfusion in old mdx mice

Despite severe alterations in *mdx* muscle microvascular network organization, no difference in muscle perfusion was observed between *mdx* and wt mice at rest (*mdx*: 12.09±5.90 ml/min/100g; wt: 8.19±2.19 ml/min/100g). After tourniquet release, rapid increase of perfusion was detected in muscles of the posterior hindlimb compartment; this increase was significantly lower in old *mdx* mice (*mdx* perfusion maximal value at 380s post-ischemia: 60.5±39.3 ml/min/100g; wt perfusion maximal value at 400s post-ischemia: 106.1±38.1 ml/min/100g, p<0.05), in contrast to what was seen in young mice.

Analysis of variance of perfusion time-courses demonstrated differing profiles between WT and *mdx* ($p<10^{-4}$), with specific differences in the early phase of reperfusion. A similar initial peak of perfusion, as the one observed in young-adult wt mice, was detected in the old wt group, 20s post-ischemia, but was absent in *mdx* mice (Figure 3.3 B).

Thus at 12 months, both *mdx* and wt showed different profiles from young-adult animals (ANOVA, $p<10^{-6}$), and in contrast to wt and young-adult *mdx*, old *mdx* mice displayed a decrease in muscle perfusion and a modified perfusion profile after an ischemic stress.

Muscle bioenergetics in 12 month-old mice (Table 3.2)

At rest, no difference in pH was observed between wt (n=7) and *mdx* (n=5) mice but hypoxic stress induced a significant acidosis in both groups ($p<0.005$), more pronounced in *mdx* (wt: $\Delta\text{pH} = 0.22\pm0.06$; *mdx*: $\Delta\text{pH} = 0.30\pm0.04$; $p<0.05$). Ischemia was associated with a significant increase in PCr depletion in old dystrophic mice compared to wt, though the difference in Pi/PCr ratio between the two groups was not significant. Unlike in young mice, the rephosphorylation rate was comparable in both groups. Indeed τPCr was shorter in the old compared to the young wt mice ($p<0.01$), but it was unchanged with age in the *mdx* mice. Thus, no alteration of oxidative capacities was observed in old *mdx* mice in response to hypoxic stress compared to age-matched control mice, despite reduced perfusion. In older mice (wt and *mdx*), no correlation was found between τPCr and perfusion variables.

Table 3.2. Energetic metabolism analysis from ^{31}P -spectroscopy in old mice.

	wt (n=7)	<i>mdx</i> (n=5)
ΔPCr (%)	54 ± 4	$63 \pm 2^{**}$
τPCr (s)	66 ± 25	80 ± 20
pH at rest (pH_{rest})	7.16 ± 0.07	7.18 ± 0.04
pH end ischemia (pH_{end})	6.94 ± 0.04	$6.87 \pm 0.04^*$
Pi/PCr at rest ($\text{Pi/PCr}_{\text{rest}}$)	0.08 ± 0.04	0.10 ± 0.01
Pi/PCr end ischemia ($\text{Pi/PCr}_{\text{end}}$)	1.24 ± 0.40	1.34 ± 0.20
PCr/ATP γ at rest ($\text{PCr/ATP}_{\gamma\text{rest}}$)	2.98 ± 0.35	3.05 ± 0.16
PCr/ATP γ end ischemia ($\text{PCr/ATP}_{\gamma\text{end}}$)	1.20 ± 0.35	1.36 ± 0.30

Ischemia stress was sufficient as the mean depletion of phosphocreatine (PCr) for wt and *mdx* mice was above 50%. ΔPCr is higher in *mdx* mice; pH decreased for both wt and *mdx* mice after ischemia, but *mdx* mice suffered a more severe acidosis. Others energetic parameters did not change in our experimental conditions (* $p<0.05$, ** $p<0.01$).

Discussion

Our study deciphers lesions of muscle microvascular network, in a model of chronic myopathy, using combination of state of the art histology/morphometry techniques and totally non-invasive functional approach. This experimental paradigm, combining histopathology and mpf-NMR, clearly relevant for clinical diagnosis and research, allowed us to associate for the first time the fine 3D-alterations of muscle microvascular network with functional repercussions on muscle.

Concerning the animal model, previous studies used 6 week to 6 month-old *mdx* mice (Loufrani et al., 2004; Matsakas et al., 2013; Palladino et al., 2013), which display very few chronic lesions with no fibrosis, in contrast to what happens in human (Grounds et al., 2008). We therefore worked on 12 month-old *mdx* mice, displaying persistence of endomysial inflammation and fibrosis, more representative of human DMD and thus more relevant for chronic myopathy and DMD pathophysiology study, in contrast to young-adult *mdx* mice displaying no chronic lesions. We demonstrated (i) strong alterations of microvascular network structure associated with reduced muscle perfusion in old *mdx* mice, (ii) functional increase in muscle perfusion and mitochondrial oxidative phosphorylation with normal microvascular network organisation in young-adult *mdx* mice, and (iii) a different impact of age on wild-type and *mdx* mouse muscles.

In young-adult and old wild-type mice, no difference could be detected in muscle histology or microvascular network organisation. Perfusion is primarily regulated by smooth muscles that control blood flow distribution and capillary recruitment (Clifford and Hellsten, 2004). Capillary resistance, at rest, plays only a minor role in perfusion regulation. Using ischemia-reperfusion, we provoked maximal arteriolar dilatation in order to limit arteriolar resistance, and thus capillary network becomes predominant in control of muscle perfusion (Baligand et al., 2012). Analysis of perfusion profiles revealed the existence of a “peak” of perfusion in the first seconds after ischemia release, for young-adult and old wild-type mice. This initial “peak” suggests specific regulation of perfusion in early phase after ischemia release, probably coordinated by perivascular smooth muscles and/or pericytes (Yemisci et al., 2009).

Surprisingly and in contrast to previous studies describing decreased vascular density (Loufrani et al., 2004; Matsakas et al., 2013), we did not detect any alteration in vascular network 3D-organisation in young-adult *mdx* mice. However, muscle post-ischemic perfusion was higher than in age-matched control mice. Moreover, time resolution of mpf-NMR allowed to demonstrate the absence of the initial “peak” of perfusion, probably because of an alteration of perivascular smooth muscles and/or pericytes. In smooth muscle, loss of dystrophin indeed results in decreased capacity of vasculature to respond to shear stress induced endothelium-dependant dilatation, probably related to NO production alteration (Loufrani et al., 2001). Absence of dystrophin also provokes defects in mechanotransduction, secondarily responsible for down-regulation of new blood vessel formation (Ando and Kamiya, 1992; Davies and Nowak, 2006; Ichioka et al., 1997). One of the main mechanisms considered in the literature to explain variations of perfusion in dystrophinopathies is a defect in neuronal NO (nNOS) synthase activity. In DMD pathogenesis, absence of dystrophin leads to an impairment of nNOS localisation to the sarcolemma resulting in muscle vasoconstriction and abnormal blood flow during muscle contraction (Brenman et al., 1995; Loufrani et al., 2001; Sander et al., 2000). Concerning pericytes, Yemisci demonstrated in the brain, after a 2h ischemic stress, that pericytes remain contracted despite successful re-opening of blood flow, impairing microcirculatory reflow (Yemisci et al., 2009). These experiments were carried out *ex vivo*, and no functional *in vivo* validation was done. Our data obtained in mpf-NMR seem therefore to highlight functional alterations of smooth muscles and/or pericytes after ischemic stress. This alteration is severe enough to significantly impact perfusion profiles between control and *mdx* mice, and we are currently carrying out new experiments to better understand the effect of an absence of dystrophin in perivascular cells and their involvement in dystrophinopathy pathophysiology. Interestingly, a longitudinal PET study in dystrophic mice evidenced that normalised resting blood flow and blood volume, in addition to FDG uptake, were higher in 8 week old dystrophic mice than in wt, and progressively decreased to below wt values at 22 weeks of age, and this age-dependent effect graded with severity of dystrophy (Ahmad et al., 2011).

Old Flk1^{GFP/+}::*mdx* model allowed us to highlight disorganisation of microvascular network. A marked increase in capillary tortuosity, an irregular

scattering, and an increase in anastomose count were observed. Existence of these highly abundant anastomoses, suggests that “radial” as well as “longitudinal” (parallel to myofibers) blood flow is important, and in turn, that “longitudinal” flow is abnormally heterogeneous, capillary longitudinal resistance being likely to vary a lot from capillary to capillary which would be the driven force for collateral flow.

Considering the close association between capillaries and myofibers, we demonstrated in old *mdx* mice that more than 60% of myofibres were atrophic with peripheral nuclei and displayed less capillaries at their periphery, resulting in a global undercapillarisation. In parallel, NMR analysis revealed a two-fold decrease in perfusion after ischemia release. The significant decrease of capillary density around small myofibers is likely responsible for these functional alterations. Under maximal arteriolar dilatation, capillary resistance, which is inversely proportional to capillary density, becomes indeed predominant in controlling peripheral resistance. Our data are thus in agreement with other studies demonstrating the effect of age on dystrophinopathy pathophysiology (Palladino et al., 2013; Straino et al., 2004). Our hypothesis is that interaction between angiogenesis and myogenesis could be affected in old *mdx* mice; the increasingly scarce capillaries would provoke an alteration of myofiber regeneration that in turn could lead to impairment of remaining microvascular network support, maintaining a vicious circle. Christov et al. already introduced the idea that angiogenesis and myogenesis are coupled during muscle regeneration, these processes involving several growth factors, such as vascular endothelial growth factor - VEGF (Christov et al., 2007). Treatment with VEGF strongly ameliorates *mdx* phenotype, with improvement of functional parameters, increase in capillary density, improved muscle regeneration, and decrease in interstitial fibrosis (Deasy et al., 2009; Messina et al., 2007). Fibrosis is by the way a key parameter influencing perfusion, and is increased in DMD (Desguerre et al., 2009). However, fibrosis might not be the most limiting factor to perfusion, as it only represents 10% of old *mdx* mice muscle tissue in our study. Moreover, distance between capillaries and myofibers, generally modified with endomysial fibrosis (Hepple, 1997), is similar between young-adult and old wild-type and *mdx* mice.

The reproducibly observed in vivo increase of post-ischemic muscle perfusion with old age in wt animals was found to be reproducible with age in this and other

mouse strains, but no explanation is currently put forward, while effect of aging on perfusion is still debated even in humans (Rudroff et al., 2014; Trinity et al., 2014).

In parallel to perfusion analysis, acquisition of ^{31}P -spectroscopy revealed moderate energetic metabolism alterations, in agreement with previous literature, and contrarily to what might be expected from alterations of enzymatic activities or defects of mitochondrial localization *in vitro*. Compensatory mechanisms must thus exist in dystrophic muscle (Cole et al., 2002; Dunn et al., 1991; Heerschap et al., 1988).

As for perfusion, anomalies in phosphorus metabolites in wild-type animals depended on age, as already evoked in early studies of *mdx* metabolism (Dunn et al., 1991, 1993). Anomalies at rest were more marked in younger *mdx*: Pi/PCr reflecting resting ADP production was increased while PCr/ATP proportional to functional muscle was reduced (-11%), coherently with other reports (Cole et al., 2002; Dunn et al., 1991; Heerschap et al., 1988) (-50% or more in DMD children (Kemp et al., 1993)).

Unlike a recent study in 3 month-old *mdx* mice (Percival et al., 2013), where 10min ischemia was used as stress protocol, we found greater depletion after 30min ischemia in both young-adult and old *mdx*. During prolonged ischemia, two energetic pathways are activated to supply ATP demand: ATP-PCr system and glycolytic pathway. Production of ATP directly from PCr consumption is very small; it is therefore unlikely that PCr would be consumed to compensate for defective glycolytic pathway. The higher depletion observed in both young-adult and old *mdx* could more likely reflect a higher ATP demand to maintain ionic homeostasis.

Confrontation between perfusion and metabolic data obtained simultaneously by NMR revealed that despite strongly reduced perfusion in old *mdx* mice, oxidative metabolism was preserved, suggesting existence of a “luxury perfusion”, *i.e.* reserve of perfusion that can be eliminated without impact on muscle physiology, as previously evidenced in a model of peripheral artery disease (Vidal et al., 2002). It generally explains the absent – or very loose – correlation between perfusion and PCr recovery rates in wild-type animals and in old *mdx*. This contrasts with the tight correlation between initial perfusion and τPCr of young *mdx* mice, which display faster τPCr recovery and stronger perfusion than controls. Using optical spectroscopy

to analyse myoglobin and haemoglobin oxygen desaturation in parallel to ^{31}P -NMRS, Percival observed strong uncoupling between ATP synthesis and O_2 consumption in 4 month-old *mdx*, dystrophic muscle producing 39% ATP less per O_2 consumed than controls (Percival et al., 2013). We might thus hypothesize that at this young age, increased perfusion might be a means to compensate for mitochondrial inefficiency.

Conclusion

In conclusion, we demonstrated strong structural and functional alterations in muscle microvascular network of dystrophin-deficient *mdx* mice, with an increasing severity in parallel to aging. Our approach combining 3D-morphological analyses with non-invasive functional evaluation, allowed to better characterise the impact of histological lesions on tissue function. Collectively, our data pointed out that vascular network has a key role in dystrophinopathy pathophysiology and would be very important target for the set-up of new innovative therapeutic strategies.

Supplementary Information

S3.1. Nuclear Magnetic Resonance analysis

Multiparametric functional NMR (mpf-NMR) acquisitions.

Ischemia of the left leg was induced by occlusion of the femoral artery by two surgical threads placed around the thigh. During the experiment, both perfusion through arterial spin labelling (ASL) NMR imaging and energetic metabolism through ^{31}P -NMR spectroscopy were followed.

NMR perfusion analysis.

Arterial spin labelling (ASL) is based on the non-invasive magnetic tagging of blood water spins. Images were acquire after positive or negative labelling alternately (Figure S3.1-A). To avoid large vessels, regions of interest (ROI) were drawn in the posterior compartment of the leg. Muscle perfusion f was calculated from the normalized difference between consecutive images according to the equation (Raynaud et al., 2001):

$$f = -\lambda / T_{ev} \times \ln \left[\frac{(M^+ - M^-)}{(M^+ + M^-) \times (1 - \exp(r_l T_{ev}))} + 1 \right]$$

where r_l is the longitudinal relaxation rate for muscle ($r_l = Tl^{-1}$, Tl measured by saturation-recovery acquisition for each mouse at the end of 30 minutes hyperaemic period), M^+ and M^- are the signals of positive and negative labelled perfusion images and λ is the blood-tissue partition coefficient ($\lambda=0.9$).

^{31}P -NMR Spectroscopy analysis.

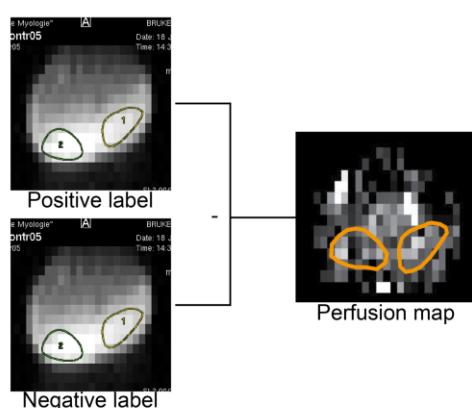
Successive ^{31}P Free Induction Decays were acquired throughout rest, ischemia and hyperaemia. ^{31}P -spectroscopy gives access to principal metabolites implicated in energetic metabolism such as phosphocreatine (PCr), the three α , β , γ ATP and inorganic phosphate (Pi). Signal intensity of these resonances is directly proportional

to their concentrations, which allows the quantitative following of these metabolite variations (Figure S3.1-B).

At ischemia and recovery, PCr recovery was fitted by a mono-exponential function with a least mean squares algorithm and pH was calculated from the chemical shift δ_{Pi} between PCr and Pi according to the formula (Taylor et al., 1983):

$$pH = 6.75 + \log \left[\frac{(3.27 - \delta_{Pi})}{(\delta_{Pi} - 5.69)} \right]$$

A Perfusion map



B ^{31}P spectrum

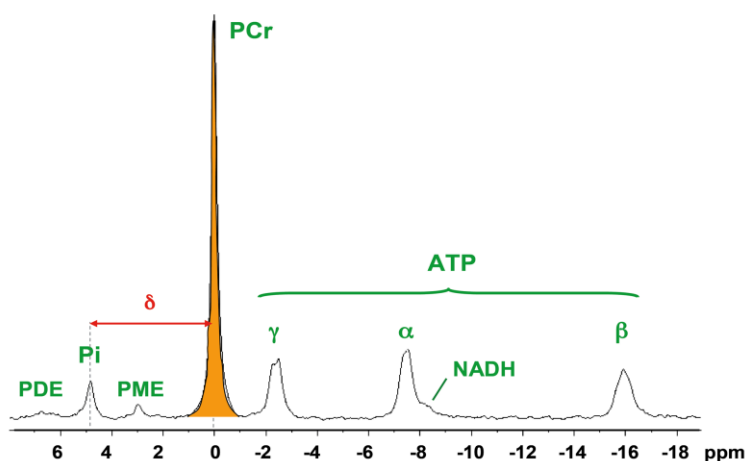


Figure S3.1. Nuclear Magnetic Resonance analysis. Multiparametric and functional NMR allows measurement of muscle perfusion with imagery combined to ASL and energetic metabolism through ^{31}P -spectroscopy. A combination of these measures in

one experiment gives access to relations between muscle blood supply and bioenergetics during a stress. (A) Perfusion is obtained by acquisition of images after positive and negative labelling; the perfusion map is obtained by the difference between consecutive images. (B) ^{31}P -spectroscopy gives access to principal metabolites implicated in energetic metabolism such as phosphomonoesters (PME), inorganic phosphate (Pi), phosphodiester (PDE), phosphocreatine (PCr) and the three α , β , γ ATP. pH is calculated from the chemical shift δ_{Pi} between PCr and Pi.

Chapter 4

Non-invasive NMR study of the mouse
model for centronuclear myopathy with
mutation in the dynamin-2 gene

Chapter 4. Non-invasive NMR study of the mouse model for centronuclear myopathy with mutation in the dynamin-2 gene

Introduction

Congenital myopathies are a group of genetic muscle diseases with non-dystrophic characteristics, clinical presentation at birth and slow progression. The structural forms are characterized by the presence of morphological alterations within the muscle fiber, such as the presence of regions with protein accumulation (rods), regions with altered organelles distribution (cores), or with altered positioning of the nucleus. The kind of morphological alterations defines the three major categories of structural congenital myopathies: nemaline myopathy, core myopathies and centronuclear myopathies.

In the group of centronucleated myopathies, muscle fibres present internalized or centralized nuclei, in opposition to the peripheral positioning observed in normal muscle fibers. Histopathological characteristics can include abnormal NADH-TR staining, but do not involve extensive muscle degeneration and regeneration. Clinically, centronuclear myopathies are highly variably regarding the age of onset and pattern of weakness, ranging from severe congenital forms to adult-onset forms with slow progression and mild phenotype (Nance et al., 2012). The variability in the phenotype is related to the mutations in the involved genes. The more severe X-linked form of centronuclear myopathy is caused by mutations in *MTM1* gene, coding for the protein myotubularin. Mutations in the gene coding for amphiphysin 2 (*BINI*) lead to juvenile autosomal recessive centronuclear myopathy; and mutations in the gene coding for dynamin-2 (*DNM2*), with autosomal dominant heritage, are related to a generally more benign adult phenotype of centronuclear myopathy. Additional cases with mutations in *RYR1*, *hJUMPY* and *MTMR14* genes have been also described (Bitoun et al., 2005, 2007; Jungbluth et al., 2008; Nance et al., 2012; Wilmschurst et al., 2010). Mutation in the *PTPLA* gene is related to centronuclear myopathy in

labrador dogs, but until now, there is no report of mutations in this gene causing centronuclear myopathy in humans (Pelé et al., 2005).

Animal models of congenital myopathies have been developed, helping in the elucidation of the disease pathomechanisms and in the search for therapeutic strategies. Among the murine models of structural myopathies, there are several models for nemalinic myopathy that mimic the phenotype observed in human disease, in the same way as the *Ryr1* knock-in models for core myopathy (Boncompagni et al., 2009; Zvaritch et al., 2009). On the other hand, some murine strains with the same molecular defect as human patients do not present weakness and histopathological features as observed in humans, such as the *Sepn1* knockout mouse, which aimed to model core myopathy (Rederstorff et al., 2011).

Among the centronuclear myopathies murine models, *Mtm1* knock-out (Buj-Bello et al., 2002) and the *Mtm1* p.R69C knock-in mice (Pierson et al., 2012), models for myotubular myopathy, have similar severe clinical and histological features as observed in patients. For the *DNM2* gene, a mouse model was developed carrying the most frequent mutation detected in patients with *DNM2*-related centronuclear myopathy: the knock-in *KI-Dnm2*^{R465W} mouse. In opposition to what is observed in humans, heterozygous mice have a small proportion of centronucleated fibers and a mild phenotype, with muscle atrophy and force reduction that start after 2 months of age (Durieux et al., 2010).

There is no cure or treatment for the congenital myopathies, which drives the study of therapies based on new methods, such as cellular and genetic approaches. Non-invasive methods to follow the possible benefits of these new therapeutic strategies in clinical trials are highly desirable. In this context, nuclear magnetic resonance (NMR) studies in patients and animal models for congenital myopathies have been developed, in a first moment to better describe muscle involvement in these disorders, but with potential use as outcome measures in clinical trials.

Muscle nuclear magnetic resonance imaging (NMRI) from congenital myopathy patients allowed identifying the pattern of muscle involvement in these diseases, with strong correlation with the genotype. This pattern varies among congenital myopathies but also between other muscle pathologies, such as muscular dystrophies and inflammatory myopathies. The identification of the pattern of muscle

involvement can orientate the molecular study and help in the differential diagnosis in humans (Mercuri et al., 2007; Quijano-Roy et al., 2011, 2012).

There are still very few NMR studies with animal models for congenital myopathy. Gineste and collaborators have developed a series of NMR studies in murine models for nemaline myopathy, where increased energetic cost for muscle contraction and higher muscle T2 could be observed (Gineste et al., 2013a, 2013b, 2013c). In this context, the aim of this study is to enrich the panel of murine models non-invasively characterized with NMR. *KI-Dnm2^{R465W}* mice model to autosomal dominant centronuclear myopathy were evaluated at different ages. NMR results were compared to histological findings, aiming to find parameters of muscle alteration detectable even when a mild phenotype is present.

Materials and Methods

Animals

In total, 29 mice were evaluated by NMR: 9 heterozygous *KI-Dnm2^{R465W}* (*Dnm2*) mice and 5 normal littermates (wild-type) of 3 months of age; 7 *Dnm2* and 8 wild-type of 6 months of age. Additionally, 4 *Dnm2* and 2 wild-type mice (4 month-old) were included for histological analysis. Mice were kindly supplied by Dr. Marc Bitoun, Institut de Myologie. Mice were kept under the French rules for good animal care.

Nuclear Magnetic Resonance (NMR)

For NMR measurements, mice were anesthetized with 4% isoflurane (Forene, Abbott, Rungis, France) delivered in 1.5 L/min air, and anesthesia was maintained with 1.75% isoflurane. Breathing was monitored all along the experiments, and mice were kept at 37 °C using a heating water pad.

In vivo NMR experiments were done in a 4T magnet (Magnex, Abington, UK) equipped with a 20 cm diameter 200 mT.m⁻¹ gradient insert (Bruker BioSpin MRI GmbH, Ettlingen, Germany) and interfaced with a Biospec Avance console using ParaVision 3.0.2 software (Bruker BioSpin MRI GmbH). 1H coil designed for mouse

experiments and built in the NMR Laboratory was used. All NMR experiments were done in the NMR Laboratory, Institut de Myologie, Paris, France.

Tridimensional T1 weighted images of the posterior limbs, from the feet to the lumbar region, were acquired for the anatomical evaluation (RARE - *Rapid Acquisition with Relaxation Enhancement* - sequence: TE=9.82 ms, TR=800 ms, NEX=1, RARE-factor = 4, FOV: 4.5 x 2.56 x 5.0 cm, matrix size: 256 x 192 x 64).

T1 and T2 measurements were acquired in two selected slices, one in the thigh and one in the lower leg. The lower leg slice was positioned at 1/4 of the tibia length (evaluated from the 3D scan) from the knee, a position close to the maximum cross section area (CSA). The thigh slice was positioned symmetrically to the lower leg slice from the knee. For T1 measures, a saturation recovery sequence was used, with 13 different TR (0.002, 0.1, 0.2, 0.3, 0.4, 0.6, 0.8, 1.2, 1.6, 2.4, 3.2, 4.0 and 6.5 s), TE=10 ms and NEX=2. For T2 measurements, a Multi-Slice Multi-Echo (MSME) sequence was used, with 32 TEs ranging from 5.03 ms to 160.96 ms ($5.03 \text{ ms} * n$; $n=1, \dots, 32$), TR=2158.4 ms and NEX=4. Sequences for T1 and T2 measurement were acquired using the same geometry: slice thickness=2.0 mm, FOV=4.0 x 4.0 cm, matrix size 128x128.

Data analysis

For 3D-T1w images, any possible fat infiltration in muscles was evaluated qualitatively in the tridimensional reconstruction. Tibia length was measured in a coronal cut (Figure 4.1-a), while total cross section area (CSA) and cross section area excluding subcutaneous fat (CSA_m) were measured in a transversal projection, positioned at 1/4 of the tibia length from the knee (Figure 4.1-b). Muscle atrophy was evaluated comparing the ratios CSA over tibia length (CSA/L_{tibia}) and CSA_m over tibia length (CSA_m/L_{tibia}).

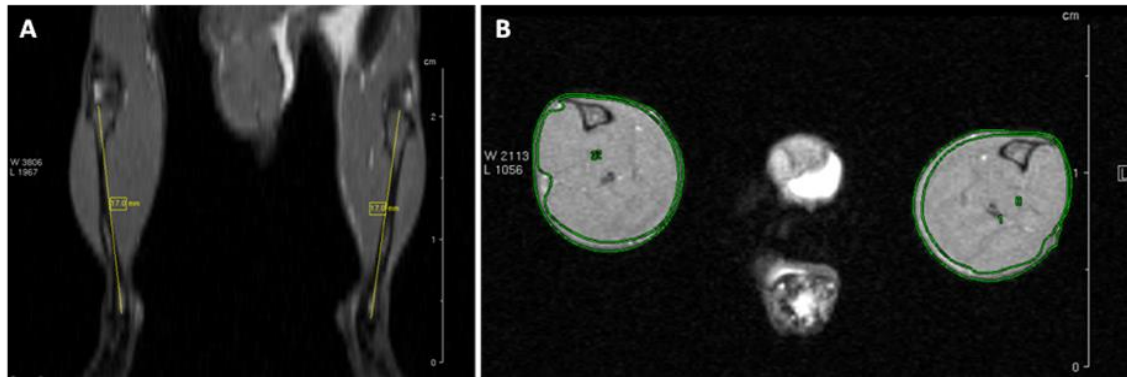


Figure 4.1: Anatomical measures: tibia length and cross section area with and without subcutaneous fat. T1-weighted images showing the posterior limbs of two wild-type mice, illustrating the measurement of: (A) tibia length in a coronal section, and (B) cross section area including (CSA) and excluding subcutaneous fat (CSA_m).

For T1 and T2 measurements, six regions of interest were drawn, four in the lower leg slice and two in the thigh slice. In the lower leg slice, ROIs encompassed the following muscles: gastrocnemius/soleus lateral (GL), gastrocnemius/soleus medial (GM), tibialis anterior/extensor digitorum longus/peroneus (TA/EDL/Pe), and tibialis posterior/flexor digitorum longus (TP/FDL), as exemplified in Figure 4.2-A. In the thigh level, two ROIs were drawn to comprise all muscles in medial (TM) or lateral compartments (LM) (Figure 4.2-B). One additional ROI was drawn in both slices including only noise, for use in T2 estimation. The NMRI signal was used for fitting monoexponential curves to T1 and T2 values.

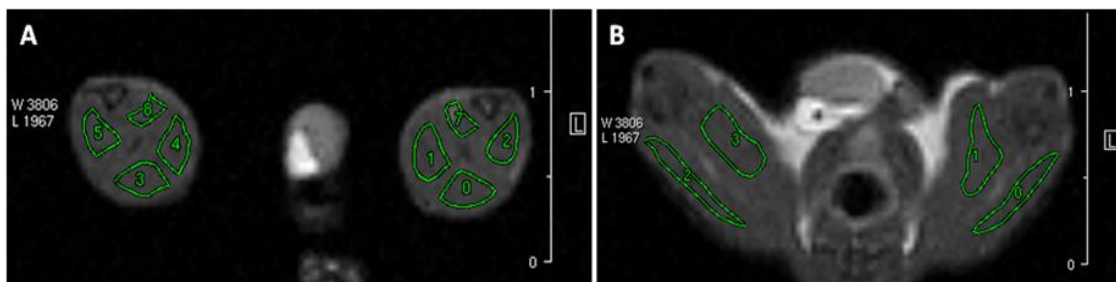


Figure 4.2: ROIs for T1 and T2 measurements. Transversal images at (A) lower leg and (B) thigh levels from a wild-type mouse, showing ROIs designed for T1 and T2 measurements. (A) At the lower leg level, 4 ROIs were selected in each leg: gastrocnemius lateralis (GL: 0,3), gastrocnemius medialis (GM: 1,4), TA/EDL/Pe

(2,5), and TP/FDL (7,8). (B) At the thigh level, two ROIs were designed for each leg: lateral (TL: 0,2) and medial (TM: 1,3) compartments.

Histological analysis

Four *KI-Dnm2*^{R465W} and 2 wild-type mice (4 month-old), which were not evaluated by NMR, were euthanized by cervical dislocation under anesthesia. The gastrocnemius muscle was collected, immediately frozen in liquid N₂ cooled isopentane and kept at -70°C until use. The muscles were cut in 8 µm slices and stained with hematoxylin-eosin (H&E) for general histological evaluation, and with NADH-TR and SDH staining for the evaluation mitochondrial distribution in muscle fibres.

Statistical analysis

Data were analyzed with one-way analysis of variance (ANOVA) or repeated-measures ANOVA, followed by Bonferroni multiple comparison of means when appropriate (NCSS, Kaysville, UT, USA). One-way ANOVA with two factors (mouse strain: *KI-Dnm2*^{R465W} or wild-type; age: 3 or 6 months) was used to compare mice weight, CSA/L_{tibia} and CSA_m/L_{tibia} ratios. Repeated measures ANOVA with two factors between groups (mouse strain: *KI-Dnm2*^{R465W} or wild-type; age: 3 or 6 months) and one factor within groups (muscle group) was used to compare muscle T1 and T2 values (mean value from left and right leg for each mouse). The differences were considered significant when p<0.05 (after Geisser-Greenhouse correction for the repeated measures ANOVA). NMR data are reported as mean ± standard deviation (SD).

Results

Morphometrical evaluation

Visually, T1 weighted images did not show evidences of fat infiltration or altered signal in muscles from *KI-Dnm2*^{R465W}. Body weight, cross section area

normalized to tibia length (CSA/L_{tibia}) and cross section area excluding the subcutaneous fat normalized to tibia length (CSA_m/L_{tibia}) were compared to evaluate if NMR could detect muscle atrophy in the *KI-Dnm2^{R465W}* mice. The values are described in Table 4.1.

Table 4.1: Atrophy evaluation in the *KI-Dnm2^{R465W}* mice (Dnm2)

	Weight (g)	CSA(mm ²)/L _{tibia} (mm)	CSA _m (mm ²)/L _{tibia} (mm)
Dnm2 - 3m (n=9)	28.66 ± 2.88	2.61 ± 0.29 *	2.19 ± 0.26 *
WT - 3m (n=5)	30.26 ± 2.22	3.16 ± 0.15	2.74 ± 0.25 #
Dnm2 - 6m (n=7)	32.87 ± 4.88	2.79 ± 0.18	2.26 ± 0.15
WT - 6m (n=8)	32.36 ± 2.17	2.92 ± 0.17	2.36 ± 0.15

CSA: cross section area; L_{tibia}: tibia length; CSA/L_{tibia}: atrophy index. CSA_m: CSA excluding the subcutaneous fat; CSA_m/L_{tibia}: lean mass atrophy index.

*: different from wild-type (WT) at the same age, p<0.05; #: different from the younger mice from the same lineage, p<0.05.

When comparing weight, no differences were observed between *KI-Dnm2^{R465W}* and wild-type mice, at both ages (Table 4.1). The only difference observed was between 6 and 3 months-old mice: when grouping both mouse strain the older mice had higher weight than the younger mice, as expected (3 months-old mice: 29.23±2.69 g, 6 months-old mice: 32.60±3.56 g, p<0.05). The mouse strain did not show a major effect in weight (*KI-Dnm2^{R465W}*: 30.50±4.31 g; wild-type: 31.55±2.35 g; p=0.66) and there was no combined effect of age and lineage (p=0.40).

KI-Dnm2^{R465W} mice presented lower CSA/L_{tibia} ratio than wild-type mice (*KI-Dnm2^{R465W}*: 2.69±0.26, wild-type: 3.01±0.20, p<0.001), indicating atrophy. The age did not show a major effect (3 month-old mice: 2.81±0.36; 6 month-old mice: 2.86±0.18; p=0.71), but lineage and age presented significant interaction (p<0.05). In the Bonferroni multiple comparison test, 3 month-old *KI-Dnm2^{R465W}* mice had significantly reduced CSA/L_{tibia} ratio when compared to wild-type mice at the same age (Table 4.1, p<0.05)

The ratio CSA_m/L_{tibia} was calculated in order to verify if the reduced CSA/L_{tibia} ratio observed in $KI-Dnm2^{R465W}$ mice was related to loss of lean tissue. Similarly, $KI-Dnm2^{R465W}$ mice presented lower CSA_m/L_{tibia} ratio than wild-type ($KI-Dnm2^{R465W}$: 2.22 ± 0.21 ; wild-type: 2.51 ± 0.26 ; $p < 0.001$). Age did not present major effect over CSA_m/L_{tibia} (3 months-old mice: 2.38 ± 0.37 ; 6 months-old mice: 2.32 ± 0.15 ; $p = 0.07$). Again, there was a significant interaction between mouse strain and age ($p < 0.01$). In the Bonferroni multiple comparison test, CSA_m/L_{tibia} was reduced in 3 months old $KI-Dnm2^{R465W}$ when compared to age-matched wild-type mice ($p < 0.05$). This difference disappeared when comparing 6 months-old mice, as observed in the comparison of CSA/L_{tibia} ratio. Wild-type mice showed reduction of CSA_m/L_{tibia} ratio with aging ($p < 0.05$), but this reduction was not observed in $KI-Dnm2^{R465W}$ mice (Table 4.1).

T1 measurements

The T1 values in seconds (s) for the six ROIs evaluated are shown in Figure 4.3. Mouse strain did not show a major effect on T1 values (T1 $KI-Dnm2^{R465W}$: 1.37 ± 0.06 s; wild-type: 1.37 ± 0.05 s; $p = 0.72$). Age had an influence on muscle T1 values: 3 months-old mice had higher muscle T1 than 6 months-old mice (3 month-old mice: T1 = 1.39 ± 0.06 s; 6 month-old mice: T1 = 1.35 ± 0.06 s, $p < 0.05$), but this difference was observed only when grouping both mouse strains. There was no interaction between mouse strain and age ($p = 0.93$).

Muscle groups presented a major effect on muscle T1 values ($p < 0.0001$), but there were no correlations between muscle group and mouse strain ($p = 0.52$), between muscle group and age ($p = 0.12$) or between muscle group, mouse strain and age ($p = 0.36$). This indicates that T1 varies due to intrinsic differences between muscles groups, that are probably not related neither to age nor to the mouse strain. Bonferroni multiple comparison of means showed that T1 values from lateral and medial thigh muscles were higher than the values observed in all the ROIs corresponding to lower leg muscles ($p < 0.05$). Medial thigh muscles had higher T1 value than lateral thigh

muscles ($p<0.05$). The ROI corresponding to TA/EDL/Pe had muscle T1 lower than all other muscles from the lower leg and thigh ($p<0.05$, Figure 4.3).

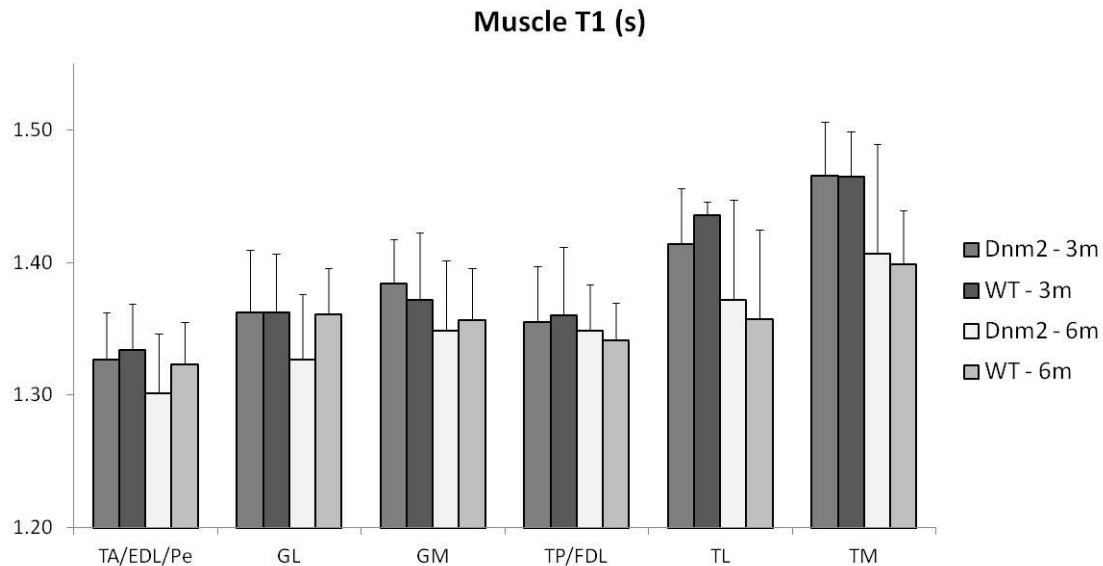


Figure 4.3: Muscle T1 for *KI-Dnm2^{R465W}* (Dnm2) and wild-type (WT) mice. Muscle T1 (seconds) varies between muscle groups, but no differences were observed between *KI-Dnm2^{R465W}* (Dnm2) and wild-type (WT) mice at both ages.

T2 measurements

The T2 values in millisecond (ms) for *KI-Dnm2^{R465W}* and wild-type mice are presented in Figure 4.4. Mouse strain showed a major effect on T2 values: muscle T2 was increased in *KI-Dnm2^{R465W}* mice when compared to wild-type mice (*KI-Dnm2^{R465W}*: 31.64 ± 1.24 ms, wild-type: 30.29 ± 1.45 ms, $p<0.0001$). There was no effect of age on T2 values (3 month-old mice: 31.23 ± 1.59 ms, 6 month-old mice: 30.85 ± 1.39 ms, $p=0.66$), and there was no correlation between mouse strain and age on the T2 values ($p=0.46$).

Bonferroni multiple comparison of means showed that both 3 and 6 month-old *KI-Dnm2^{R465W}* mice had higher muscle T2 than age-matched wild-type (T2 *KI-Dnm2^{R465W}*-3m: 31.79 ± 1.36 ms, wild-type-3m: 30.23 ± 1.51 ms, $p<0.05$; *KI-*

Dnm2^{R465W}-6m: 31.45±1.06 ms, wild-type-6m: 30.32±1.43, p<0.05). When evaluating the muscle groups separately, the *KI-Dnm2*^{R465W} mice showed higher muscle T2 than wild-type for all muscle groups (p<0.05, Figure 4.4).

Muscle group presented also a major effect on muscle T2 values (p<0.0001), but there were no correlations between muscle group and mouse strain (p=0.47), between muscle group and age (p=0.30) or between muscle group, mouse strain and age on muscle T2 values (p=0.58). Bonferroni multiple comparison of means showed that the ROIs corresponding to GL, GM and TA/EDL/Pe had lower T2 values than the ROIs corresponding to the thigh muscles and to TP/FDL. The T2 value of the medial thigh (TM) muscles was higher than the T2 value for all other ROIs. GL muscle showed a lower T2 value than GM (Table 2, p<0.05). In *KI-Dnm2*^{R465W} mice, the difference between muscle groups was similar to the observed in wild-type mice, but the T2 value for all muscle groups summed was increased (p<0.05). In general, each muscle group from *KI-Dnm2*^{R465W} mice presented a mean increase of 1.34±0.33 ms in the T2 value, 4% of the mean T2 value from wild-type mice (Figure 4.4).

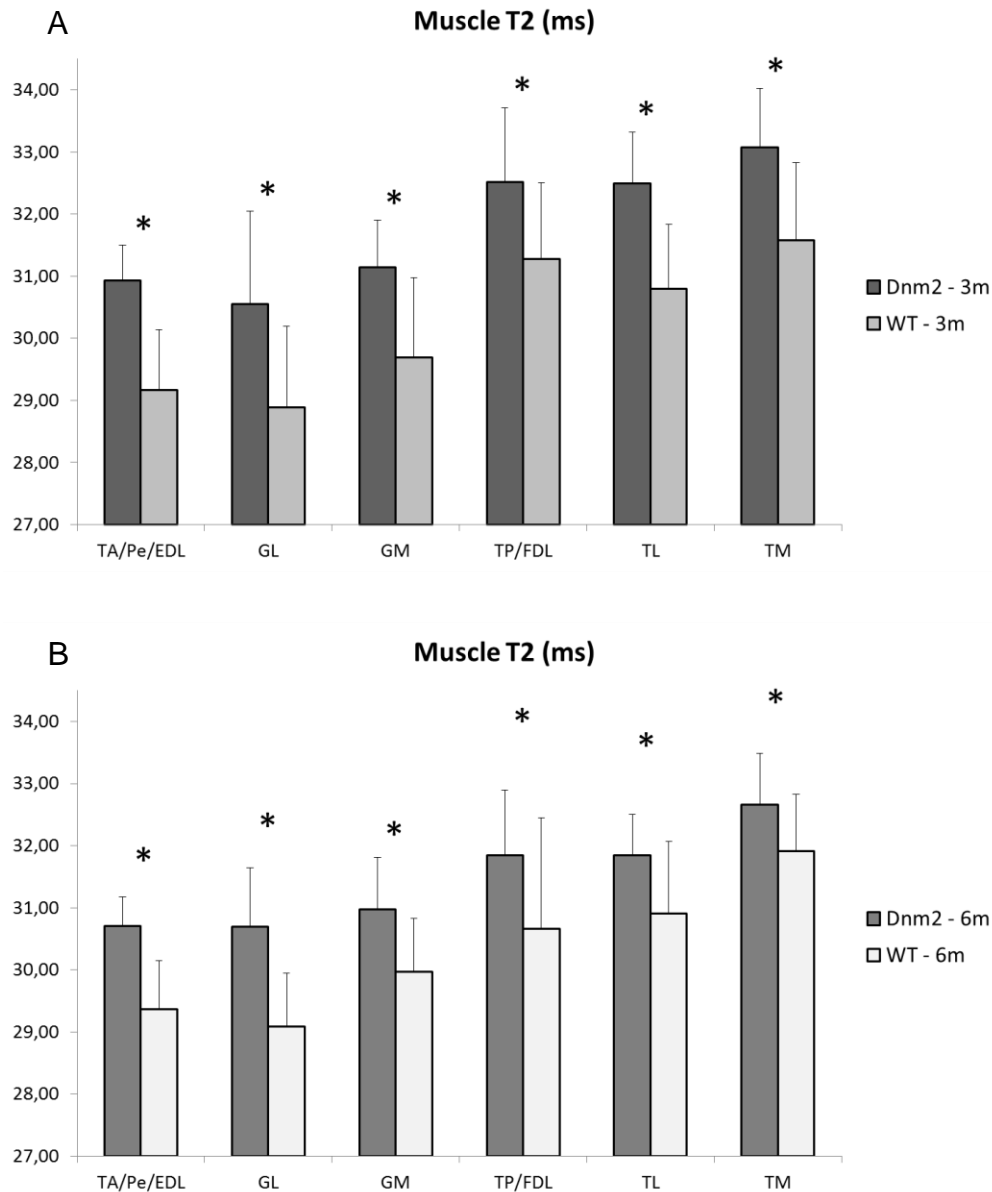


Figure 4.4: Muscle T2 for *KI-Dnm2^{R465W}* (Dnm2) and wild-type (WT) mice. Muscle T2 (milliseconds) is increased in *KI-Dnm2^{R465W}* (Dnm2) mice as compared to wild-type (WT), for all muscle groups, in (A) 3 month-old and (B) 6 month-old mice ($p < 0.05$). Muscle groups had different T2 values in both strains.

Histological analysis

Muscle from *KI-Dnm2^{R465W}* mice had a histological aspect similar to that of wild-type mice in H&E staining, with polygonal shaped fibers, thin layers of connective tissue, no inflammation nor necrosis (Figure 4.6 - A, D). Few

centronucleated fibers were observed in *KI-Dnm2^{R465W}* mice (Figure 4.6 - A, arrow). NADH-TR and SDH staining revealed higher amount of mitochondrial enzymes in the center of some fibers in *KI-Dnm2^{R465W}* mice (Figure 4.6 - B, C, arrowheads). This observation indicated for altered distribution of mitochondria: despite the normal localization of nuclei in the periphery of muscle fibers, mitochondria are concentrated in the center of muscle fibers in this mouse model.

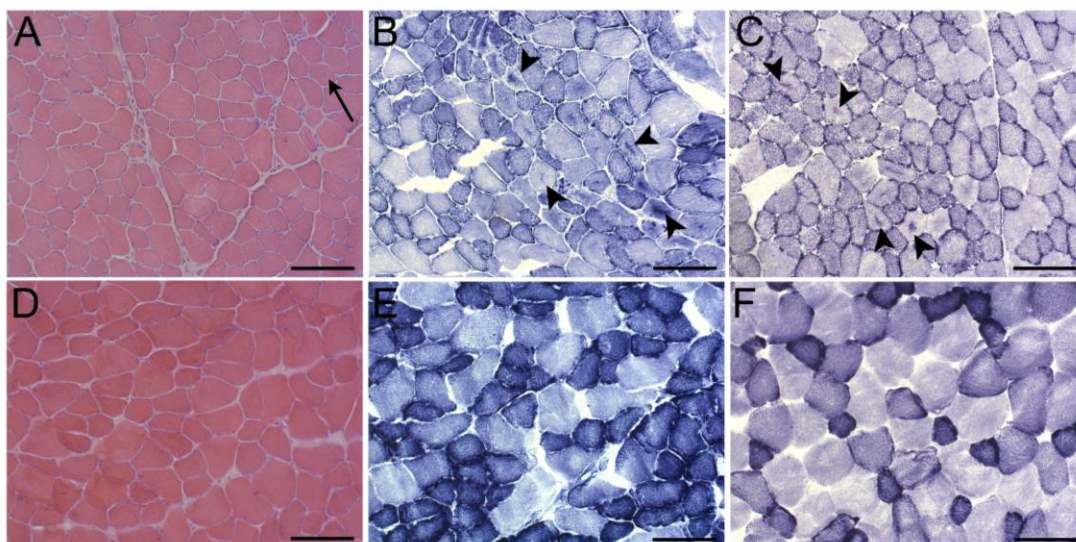


Figure 4.6: Histological analysis of *KI-Dnm2^{R465W}* and wild-type mice (4 month-old). H&E staining (A, D) showed very few fibers with centrally placed nuclei (arrow) in *KI-Dnm2^{R465W}* mice (A), but muscle is generally similar to wild-type mice (D). NADH (B, E) and SDH(C, F) staining revealed altered mitochondria distribution in the sarcoplasm of *KI-Dnm2^{R465W}* mice (arrowheads). A, B, C: *KI-Dnm2^{R465W}*; D, E, F: wild-type. Scale bars = 100 μ m.

Discussion

In this study, the heterozygous knock-in mouse with the most frequent mutation in patients with dynamin-2 related centronuclear myopathy, the *KI-Dnm2^{R465W}* mouse, was non-invasively evaluated with NMR. Morphometric measures, T1 and T2 relaxometry were compared with histological analysis, the standard method to evaluate muscles in genetic diseases. Even if only mild alterations can be detected with clinical evaluation and histological analyses in this mouse model, this non-invasive NMR study could identify muscle atrophy and increased muscle T2 in the heterozygous *KI-Dnm2^{R465W}* mice.

Despite of the similar body weight, reduced ratios CSA/L_{tibia} and CSA_m/L_{tibia} indicated muscle atrophy in the *KI-Dnm2^{R465W}* mice. The atrophy was particularly evident in 3 month-old mice, and the difference became less evident when comparing 6 months-old mice. Durieux and collaborators compared the weight of isolated muscles of heterozygous *KI-Dnm2^{R465W}* and wild-type mice at 3 weeks, 2 months and 8 months of age. *KI-Dnm2^{R465W}* mice presented progressive atrophy of gastrocnemius/plantaris, tibialis anterior and quadriceps muscles, while there was a transient weight increase for the soleus muscle at 2 months of age, and no changes for the extensor digitorum longus (Durieux et al., 2010). Our MRI comparison considered all the lower leg muscles, including gastrocnemius, plantaris, soleus, tibialis anterior and EDL, but also the other smaller muscles such as tibialis posterior and flexor digitorum longus. The combination of muscle atrophy, hypertrophy and sparing of all lower leg muscles, could be the cause of the atrophy observed with MRI in the *KI-Dnm2^{R465W}* mice only at 3 months of age.

In addition, only wild-type mice showed lean mass reduction with aging. This indicates a very slow progression, or even rescue of the myopathic phenotype in heterozygous *KI-Dnm2^{R465W}* mice. This hypothesis is corroborated by the observation of myofibers disorganization in 2 month-old heterozygous *KI-Dnm2^{R465W}* mice, with partial reversion of this alteration in 8 month-old *KI-Dnm2^{R465W}* mice (Durieux et al., 2010).

Human patients with *DNM2*-related centronuclear myopathy show increased muscle signal in T1 weighted MRI, which is related to fat infiltration in the muscles.

Lower leg muscles are usually compromised before thigh muscles in these patients. Soleus is the primarily and most affected muscle, followed by tibialis anterior, gastrocnemius and peroneus. In the thigh level, the posterior muscles are affected before anterior muscles (Catteruccia et al., 2013). In opposition to what is described for patients, *KI-Dnm2*^{R465W} mice did not show any alterations in muscle T1, for all muscle groups and ages studied. A decrease in muscle T1 would be expected in the presence of fat infiltration, and increased T1 values could be related to edema or inflammation. The *KI-Dnm2*^{R465W} mice did not present these alterations in our histological analysis and on the already described model description (Durieux et al., 2010). The absence of fat infiltration in muscles is also in agreement with other NMR and histological data from murine models for different muscle disease, where even if severe phenotype and histological aspect are observed, fat infiltration is rarely observed (McIntosh et al., 1998b; Pratt et al., 2013; Walter et al., 2005).

Despite of similar muscle T1 in *KI-Dnm2*^{R465W} and wild-type mice, a decrease in muscle T1 was observed with aging for both lineages, especially for thigh muscles. It is known that aging causes an increase in the intra muscular adipose tissue in humans (Goodpaster et al., 2001; Schwenzer et al., 2009). A similar increase in the fat content could be related to the decrease in T1 values observed in older mice from both strain, without any influence of the mutation.

Muscle T2 was increased in *KI-Dnm2*^{R465W} mice at both ages and for all muscle groups. An increase in muscle T2 was already observed in a mouse model to nemaline congenital myopathy, the transgenic mouse carrying the human Asp286Gly mutation in the *ACTA1* gene. In this mouse model, the increase in muscle T2 correlated negatively with maximum muscle force, and was considered related to the degeneration/regeneration process, indicated in the histological analysis by the presence of contronucleated fibers (Gineste et al., 2013b). This mouse model do not present the usual pathological processes related to increased muscle T2, such as inflammation, edema and necrosis, which are observed in dystrophic muscles. Histological analysis shows the presence of intracellular alterations such as nemaline bodies, tubular aggregates, ringbinden fibers and centronucleated fibers, in addition to reduced fiber diameter (Ravenscroft et al., 2011). Similarly, in our study the consistently increased muscle T2 in the *KI-Dnm2*^{R465W} could not be related to tissue

alterations such as edema, inflammation or necrosis. Instead of it, the increased muscle T2 can be possibly related to intracellular disorganization, as observed by the altered mitochondrial positioning (Durieux et al., 2010). Indeed, muscle water T2 reflects the mobility of water molecules in the tissue, being possibly affected when muscle structure is altered (Kim et al., 2010).

Alterations in muscle T2 have also been observed in centronuclear myopathy patients with mutation in DNM2. Nevertheless, in human patients these alterations are usually related to fat infiltration in muscles (Quijano-Roy et al., 2012; Schessl et al., 2007; Susman et al., 2010). Since in mouse models for genetic muscle diseases fat infiltration is extremely rare, we could not correlate the increased T2 observed in *KI-Dnm2^{R465W}* mice to the MRI observations in centronuclear myopathy patients.

Muscle groups did not show different involvement due to the disease in *KI-Dnm2^{R465W}* mice at both ages. Nevertheless, it was possible to identify variations in both T1 and T2 values for the 6 muscle groups studied, for both mouse strains. In general, thigh muscles showed higher T1 and T2 values than lower leg muscles, and the ROI corresponding to the TP/FDL muscles showed higher T2 values than the other muscles. For thigh muscles, the associated increase of both muscle T1 and T2 does not indicate for an increase in the fat content in those regions. For the TP/FDL muscles, the increase in muscle T2 without changes in muscle T1 is possibly related to the presence of a high amount of non-muscle structures in this anatomical region, such as vessels, nerves and connective tissue. Since both lineages show the same pattern of changes in T1 and T2 values for the anatomical regions evaluated, we hypothesized that these differences are possibly related to intrinsic characteristics of each muscle group, which would not be altered by the mutation in *Dnm2* gene in mice.

In conclusion, this non-invasive study was able to identify muscle atrophy and altered muscle T2 in *KI-Dnm2^{R465W}* mice, even when only small differences are observed clinically or histologically. These results indicate that NMR, especially T2 relaxometry, is sensitive enough to identify alterations in a pre-clinical stage in the centronuclear myopathy model, the heterozygous *KI-Dnm2^{R465W}* mouse.

Chapter 5

Pilot functional and metabolic evaluation of the *KI-Dnm2*^{R465W} mice

Chapter 5. Pilot functional and metabolic evaluation of the *KI-Dnm2^{R465W}* mice

Introduction

In addition to the phenotypical characterization of *KI-Dnm2^{R465W}* mice with MR images, we aimed to investigate non-invasively T1 and T2 relaxometry, function and metabolism of this mouse model. In genetic muscle diseases, muscle blood perfusion, oxygen consumption and energetic metabolism may be slightly changed or be unaffected at rest, but defective regulations alterations might be revealed by stressing the muscles. Considering that the *KI-Dnm2^{R465W}* mouse has a mild phenotype, we have conducted a pilot study to evaluate possible major functional and metabolic alterations in this mouse model, at rest and after muscle stress. *KI-Dnm2^{R465W}* mice were evaluated with multiparametric functional NMR (mpfNMR), which combines the dynamic acquisition of ASL images for the evaluation of tissue perfusion, BOLD (Blood Oxygen Level Dependent contrast) signal for the estimation of tissue oxygen balance, and ³¹P spectroscopy for the evaluation of energetic metabolism. Two different paradigms of muscle stress were applied: stimulation of concentric contractions to simulate moderate exercise, and induction of prolonged muscle ischemia to evaluate the energetic metabolism and muscle function under hypoxia and in the hyperemic response after the end of ischemic stress.

Pilot study 1. Exercise as the paradigm of muscle stress in KI-Dnm2R465W mice

Materials and methods

Animals

Six mice were successfully evaluated with functional NMR after exercise as muscle stress. Three heterozygous *KI-Dnm2^{R465W}* (*Dnm2*) and 2 normal littermates (wild-type) were evaluated with 3 months of age. One *KI-Dnm2^{R465W}* mouse could be re-evaluated at 6 months of age. One WT mice was evaluated at 6 months of age for comparison. The mice were kindly supplied by Dr. Marc Bitoun, Institut de Myologie, and were kept under the French rules for good animal care.

Electrical stimulation for the simulation of moderate exercise

The mice were laid in supine position and two surface electrodes were placed in the ankle and at the popliteal region with electro-conductive gel. A moderate exercise was simulated with pulsed electro stimulation during two minutes (pulse duration: 120 ms, interval between pulses: 2.5 s, pulse frequency: 50 Hz, pulse intensity: 2 mA). The muscle force was assessed by measuring the pressure the mouse foot exerted over a custom built non-magnetic ergometer dedicated to mice, allowing the measure of the mouse force in mili Newton - mN (Baligand et al., 2011). The 2 minutes of electrical stimulation were followed by 10 minutes of recovery, when the mpf-NMR scans were acquired. Twelve bouts of exercise-recovery were repeated and summed to allow a higher signal to noise ratio (SNR) for the NMR measurements.

Multiparametric functional NMR (mpf-NMR)

The setup used for the mpfNMR was the same as described in Chapter 3 - "Structural and functional alterations of skeletal muscle microvascular network in dystrophin-deficient *mdx* mice". Mice were laid supine with the left leg immobilized in extension. The calf was placed over a 2 cm diameter surface 1H coil, used for reception of 1H NMR signal. A 31P saddle shaped coil (length 10 mm, inner diameter

10 mm) was wrapping the leg. Then, the mouse was placed in a volume transmitter 1H coil (6 cm inner diameter and 12 cm length) for the whole-body tagging of blood. A stack of spin echo images of the mouse leg was acquired initially, and the slice of interest was chosen at the calf's largest cross-section.

Muscle function was assessed with simultaneous measures of muscle perfusion and capillary oxygenation via ASL tagging and Blood Oxygen Level Dependent (BOLD) signals, respectively. They were interleaved with the evaluation of mitochondrial activity via dynamic ³¹P MRS. Tissue perfusion and BOLD signal were acquired with an Arterial Spin Labeling (ASL) SATuration-Inversion Recovery (SATIR) pulse sequence. ASL is based on NMR labeling of the water spins from arterial blood. The labeled spins act as endogenous markers, allowing the non-invasive evaluation of blood perfusion. After alternated positive (M_+) or negative (M_-) labeling, rapid spin-echo images were acquired (inter-echo time: 2.9 s, RARE factor: 32, matrix size: 128 x 32, FOV: 5 x 2 cm, slice thickness: 2 mm, TR: 10 sec). The delay between the tag module and the image acquisition (evolution time - T_{ev}) was 1 second. The muscle perfusion (f) was then calculated according to Equation 5.1, where λ is the blood-tissue partition coefficient for the magnetization, and assuming $\lambda=0.9$ (Raynaud et al., 2001). The BOLD contrast can be extracted from the ASL spin-echo images, averaging consecutive pairs of images as described in Equation 5.2 (Duteil et al., 2006).

$$f = -\frac{\lambda}{T_{ev}} \cdot \ln \left[\frac{M_+ - M_-}{M_+ + M_-} \cdot \left(1 - \exp \left(-\frac{1}{T_1} \cdot T_{ev} \right) \right) + 1 \right] \quad \text{Equation 5.1}$$

$$BOLD = \frac{M_+ + M_-}{2} \quad \text{Equation 5.2}$$

Muscle energy metabolism was evaluated by ³¹P nuclear magnetic resonance spectroscopy (³¹P NMRS). ³¹P FIDs were collected serially from the total volume of the left leg (hard-pulse: 100 μ s, spectral width: 12 kHz, number of complex data points: 4000, TR: 2.5 sec). ASL and ³¹P NMRS signals were interleaved using a dedicated Bruker MultiScanControl tool developed on ParaVision 3.0.2 (Bruker

BioSpin GmbH, Ettlingen, Germany). During the recovery period of the ^1H NMR ASL sequence, 4 successive FIDs at the ^{31}P frequency were acquired. The interleaved acquisitions generated a set of perfusion-weighted images with 10 s of time resolution and a set of ^{31}P spectra with time resolution 2.5 s (Baligand et al., 2009). One bout of MSC was acquired without electrical stimulation (rest), followed by 12 bouts with electrical stimulation to simulate exercise.

After the mpf-NMR measures, a sequence for T1 measurement was applied over the same geometry as the ASL scans (TR: 0.002, 0.1, 0.2, 0.3, 0.4, 0.6, 0.8, 1.2, 1.6, 2.4, 3.2, 4.0 and 6.5 seconds, TE: 10 ms). The muscle T1 value for each mouse was used in the calculation of its blood perfusion (Equation 5.1).

Data Analyses

For the perfusion images, two ROIs were drawn in the posterior compartment of the leg, over the muscle tissue, avoiding large vessels, fat, skin, and bone tissue. The ROIs covered the lateral and medial gastrocnemius and part of the soleus muscle. The muscle perfusion and BOLD contrast were calculated from Equations 5.1 and 5.2, respectively.

Phosphorus spectra were processed with the standard Paravision 3.0.2 and XWIN-NMR softwares. All spectra acquired with mpfNMR were summed to generate a reference spectrum with higher SNR. The reference spectrum was treated: zero-filling (8 kHz), 8 Hz line broadening exponential multiplication, Fourier transform, manual zero- and first-order phase correction and manual baseline correction were performed. The phase and baseline correction parameters were saved and applied to all the individual spectra from mpf-NMR, after zero-filling, exponential filtering and Fourier transforming.

The areas under the peaks corresponding to phosphomonoesters (PME), inorganic phosphate (Pi), phosphodiester (PDE), phosphocreatine (PCr) and the three phosphates from ATP (α , β , γ) were integrated (PME: 8.0 to 5.6 ppm; Pi: 5.6 to 3.6 ppm; PDE: 3.5 to 1.5 ppm; PCr: 1.5 to -1.5 ppm; γ -ATP: -1.5 to -3.5; α -ATP: -6.2 to -9.2; β -ATP: -14.5 to -17.1 ppm). pH was calculated from the chemical shift δ_{Pi} between PCr and Pi according to Equation 5.3 (Taylor et al., 1983).

$$pH = 6.75 + \log \left[\frac{3.27 - \delta_{Pi}}{\delta_{Pi} - 5.69} \right] \quad \text{Equation 5.3}$$

PCr recovery after exercise was fitted by a mono-exponential function with a least mean squares algorithm, to estimate the PCr recovery time (τ_{PCr}). For the exercise protocol, 288 ^{31}P spectra were collected. The pH at the end of the exercise period was calculated based on the summation of ^{31}P spectra over the last 25 s of exercise.

Force measurements typically varied over the 12 exercise bouts: the first 2 bouts were related to higher but decreasing force, while the 10 consecutive exercise bouts were related to a similar force curve. The 10 last exercise bouts were then considered identical, allowing the inter-exercise summation of perfusion data and ^{31}P spectra collected for each animal, which allowed improving SNR.

Results

The completely non-invasive set-up used was adapted from the minimally invasive set up developed previously in the NMR laboratory (Baligand et al., 2009). Briefly, subcutaneous electrodes were replaced by surface electrodes for the electrical stimulation. The non-invasive set up was not as effective as the minimally invasive one: over 29 exams (including repeated acquisition trials in the same mouse, with at least 1 week of interval, and discarded acquisitions), only 6 could be analyzed. Among the 23 discarded exams, 8 of them were from *KI-Dnm2^{R456W}* mice and 15 from wild-type mice. The exams were discarded due to problems in the acquisition or due to alterations in the mouse vital signs: in 14 exams the force measured was too low, indicating wrong positioning of the mouse, problems in the setup or low current for electrical stimulation; 1 exam was interrupted due to breakdown of the ^{31}P coil; 1 exam was excluded due to inefficient mouse heating during the acquisition. 3 exams from wild-type mice and 1 from *KI-Dnm2^{R456W}* were stopped due to alterations in the mouse's vital signs. One exam could be completed but not evaluated: this *KI-*

Dnm2^{R456W} mouse had low perfusion and low PCr depletion, indicating that the exercise was not correctly performed, despite the normal force measurements. 2 *KI-Dnm2*^{R456W} mice, one at each age, died during the acquisition, possibly due to the isoflurane anesthesia.

Two wild-type and 2 *KI-Dnm2*^{R456W} mice at 3 months of age and 1 wild-type and 1 *KI-Dnm2*^{R456W} mice at 6 months of age could be successfully evaluated under the exercise protocol. The *KI-Dnm2*^{R456W} mouse evaluated at 6 months of age was evaluated also when it was 3 month-old. Due to the small samples, no statistic analysis was run to compare the data.

The force curve showed the expected pattern for all mice: force was higher in the first exercise bout, decreasing until the 3rd exercise bout. From 3rd to 12th exercise bouts, force was approximately constant for all mice. In general, it was not possible to identify any difference in force between *KI-Dnm2*^{R456W} and wild-type mice at 3 and 6 months of age (Figure 5.1).

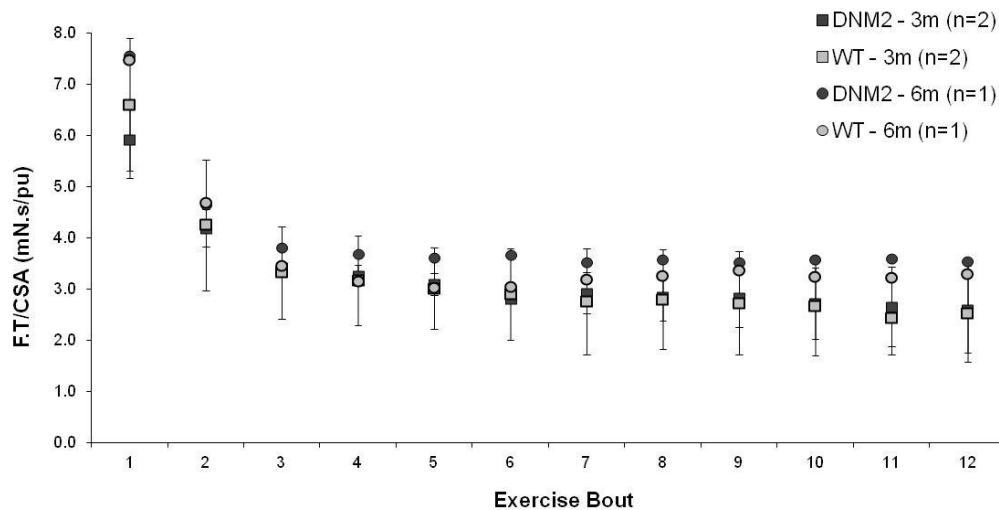


Figure 5.1. Force curve for *KI-Dnm2*^{R456W} (DNM2) and wild-type (WT) mice at 3 and 6 months of age (3m, 6m, respectively). The four groups have a similar reduction in the force exerted until the third exercise bout. Between 3rd and 12th exercise bouts, force measured is approximately constant, which allows inter-exercise summation.

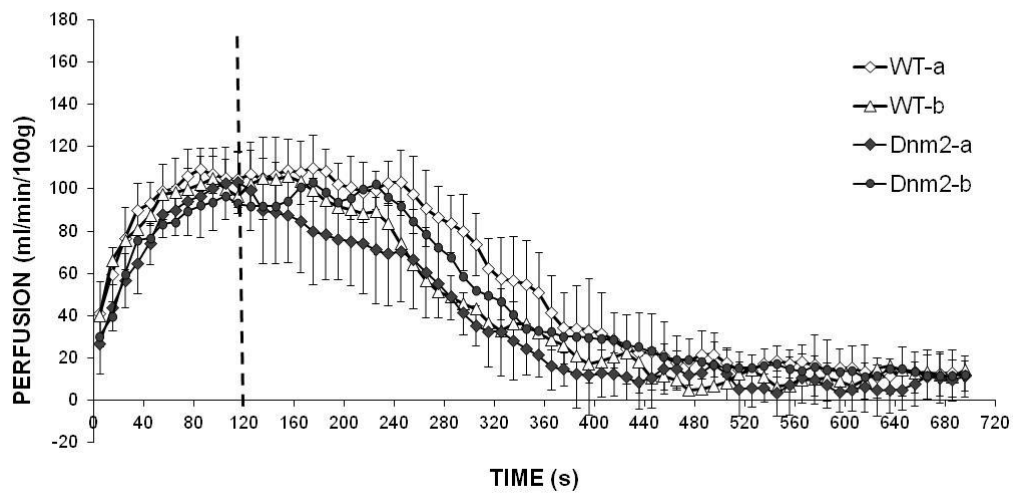
During 2 minutes of electrical stimulation to simulate exercise, muscle perfusion increased and BOLD signal decreased in all mice (Figures 5.2 and 5.3, respectively). After the end of exercise, muscle perfusion decreased until it returned to the basal level. Perfusion curves were similar for 3 month-old *KI-Dnm2^{R456W}* and wild-type mice (Figure 5.2-a). Nevertheless, when comparing 6 month-old mice, the perfusion pattern tended to be different between mouse lineages: the *KI-Dnm2^{R456W}* mouse tended to reach a higher and earlier perfusion peak after exercise than the age-matched wild-type (Figure 5.2-b). Even though, when muscle perfusion was integrated over the total exercise and recovery time, *KI-Dnm2^{R456W}* mice tended to present lower total perfusion than wild-type mice at both ages (Table 5.1). More mice should be evaluated to confirm these results.

Table 5.1. Maximum perfusion (ml.min⁻¹.100g⁻¹), time to maximum perfusion (seconds) and total perfusion (integral over time - 12 minutes) for *KI-Dnm2^{R456W}* (Dnm2) and wild-type (WT) mice at 3 and 6 months of age.

	3 month-old		6 month-old	
	Dnm2 (n=2)	WT (n=2)	Dnm2 (n=1)	WT (n=1)
Max Perf	103.05 ± 0.14	107.91 ± 3.02	154.94	115.21
Time to max (s)	135.00 ± 42.43	155.00 ± 14.14	85.00	175.00
Total Perfusion	343.77 ± 80.17	397.76 ± 77.03	408.49	423.73

Both *KI-Dnm2^{R456W}* and wild-type mice, at 3 and 6 months of age, showed the same pattern of BOLD curves. BOLD signal showed a short and transient increase in a first moment, during exercise, which evolved to an accentuated decrease. After reaching its minimum, BOLD signal started to recover and reached the initial values in the end of the recovery time (Figure 5.3). Results indicate that *KI-Dnm2^{R456W}* mice may reach the minimum BOLD signal earlier than WT mice, indicating that possibly the oxygen supply was exhausted earlier in the myopathic mice. Differences in the minimum BOLD value could not be detected between ages or strains (Table 5.2).

A)



B)

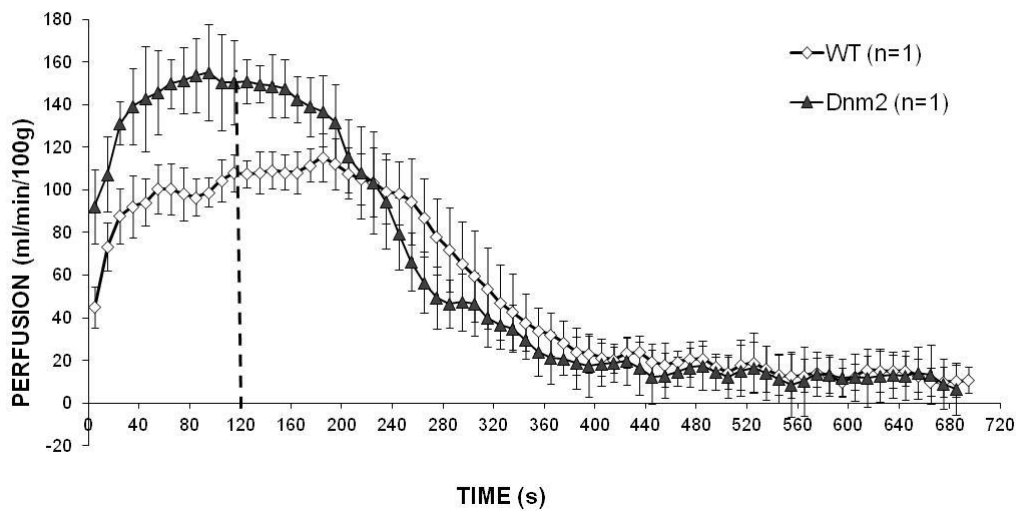


Figure 5.2: Perfusion profile for (A) 3 months-old mice and (B) 6 months-old mice. Dashed lines at 120 s indicate end of exercise and start of the recovery period. The perfusion profile for each mouse is presented isolated. (A) Visually, there is no major difference in the profile for 3 months-old *KI-Dnm2^{R456W}* (Dnm2) and wild-type (WT) mice. (B) 6 months-old *KI-Dnm2^{R456W}* mouse might have a higher and earlier perfusion peak after exercise.

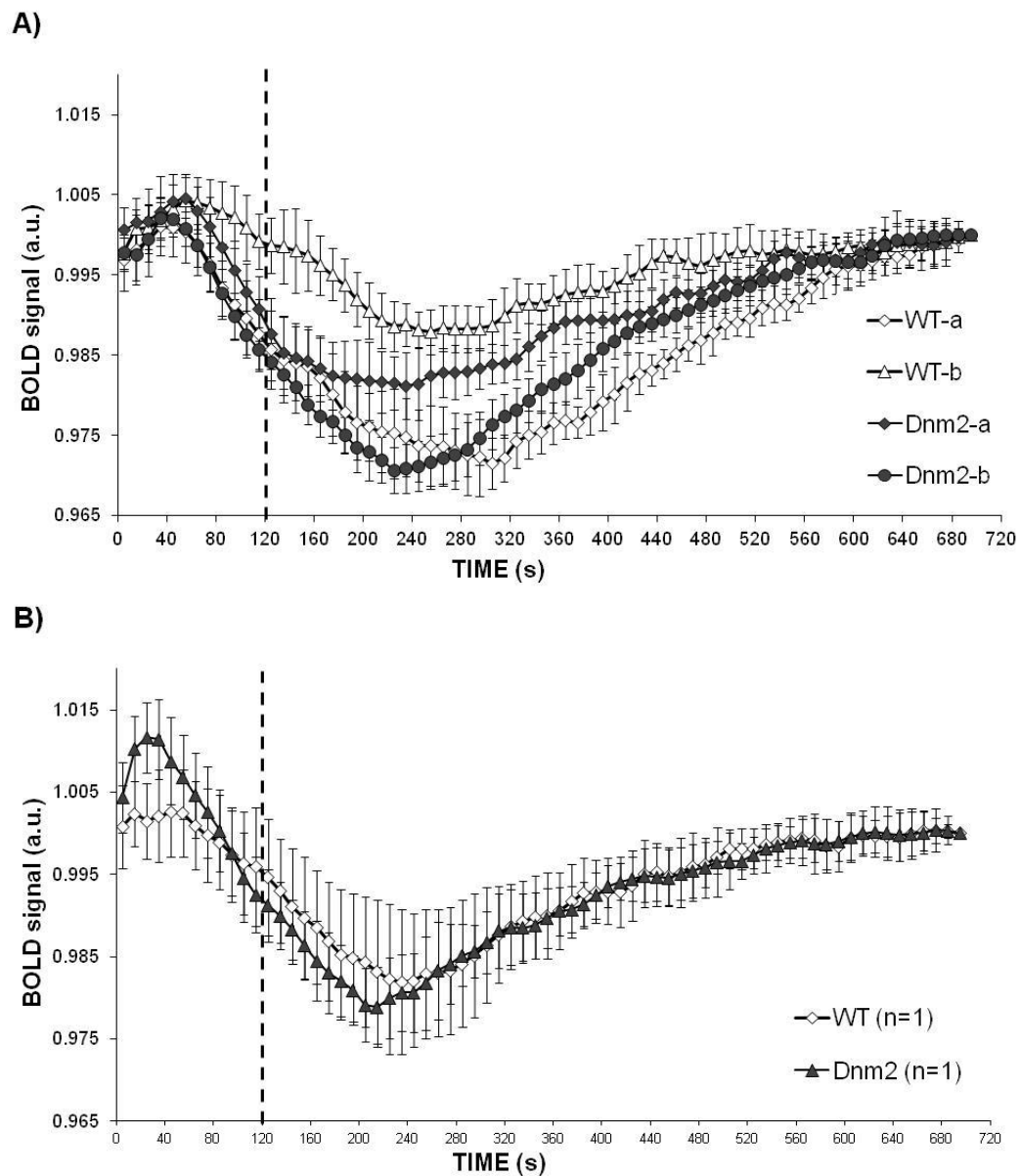


Figure 5.3: BOLD signal evolution with time for (A) 3 month-old and (B) 6 months-old *KI-Dnm2^{R456W}* (Dnm2) and wild-type (WT) mice. The BOLD profile for each mouse is shown in separated curves. Dashed lines at 120 s indicate the end of exercise and start of the recovery period.

Table 5.2. Minimum BOLD signal (arbitrary units) and time to reach minimum (seconds) for 3 and 6 months-old *KI-Dnm2^{R456W}* (Dnm2) and wild-type (WT) mice.

	3 month-old		6 month-old	
	Dnm2 (n=2)	WT (n=2)	Dnm2 (n=1)	WT (n=1)
MIN BOLD (a.u.)	0.976 ± 0.007	0.980 ± 0.012	0.974	0.982
Time to minimum (s)	220.0 ± 7.1	270.0 ± 35.4	190.00	225.00

Finally, when comparing ³¹P MRS during exercise and recovery, there was a possible tendency of higher Pi/PCr ratio in 3 month-old *KI-Dnm2^{R456W}* mice, that was inverted in 6 month-old mice. Additionally, a higher acidification after exercise might be present in 6 month-old *KI-Dnm2^{R456W}* mice (Table 5.3).

Table 5.3. ³¹P MRS acquired at rest, during exercise and recovery in *KI-Dnm2^{R456W}* (Dnm2) and wild-type (WT) mice at 3 and 6 months of age.

	3 month-old		6 month-old	
	Dnm2 (n=2)	WT (n=2)	Dnm2 (n=1)	WT (n=1)
τPCr	53.20 ± 28.02	71.91 ± 9.82	73.01	73.01
Δ PCr	0.63 ± 0.13	0.63 ± 0.01	0.72	0.72
pH-rest	7.18 ± 0.07	7.17 ± 0.01	7.27	7.24
pH-end	7.07 ± 0.01	7.04 ± 0.00	6.98	7.06
Pi/PCr - rest	0.09 ± 0.04	0.13 ± 0.00	0.11	0.08
Pi/PCr - end	2.50 ± 1.22	2.16 ± 0.04	2.22	2.70
PCr/ATP - rest	2.13 ± 0.45	2.23 ± 0.10	2.15	3.02
PCr/ATP - end	0.73 ± 0.15	0.75 ± 0.03	0.93	0.86

τPCr: time to recover PCr to the basal level; ΔPCr: percentage of PCr depletion after exercise; *end* refers to the end of exercise; Pi/PCr: proportional to ADP production; PCr/ATP: proportional to the metabolically functional muscle tissue.

Discussion

The very few *KI-Dnm2^{R456W}* and wild-type littermates evaluated functionally under this protocol showed a possible tendency of altered muscle perfusion and BOLD signal after moderate exercise. Force measures did not indicate for major differences between *KI-Dnm2^{R456W}* and WT mice. The young *KI-Dnm2^{R456W}* mice tended to have higher Pi/PCr ratio in the end of the exercise when compared to age-matched wild-type, while old *KI-Dnm2^{R465W}* mice tended to have a more accentuated acidification of muscle after exercise. The reduced total perfusion and Pi/PCr ratio associated to altered BOLD signal could indicate for impaired muscle function in *KI-Dnm2^{R465W}* mice. More mice should be evaluated to confirm the results, but it could not be done due to the experimental difficulties to run the exercise protocol. It is possible though that adjustments should be done in the set-up to allow the measurements (Wary et al., 2011).

The electrical stimulation protocol presented repeated problems, and several mice did not perform all the 12 bouts of exercise-recovery or presented very low force measures, indicating an ineffective electrical stimulation. Over 29 exams, only 6 were successful and could be analyzed. To allow a more adequate functional evaluation of the *KI-Dnm2^{R465W}* mice a different protocol was proposed, with perturbation of the muscle physiology with a prolonged ischemia.

Pilot study 2. Prolonged ischemia as the paradigm of muscle stress

Considering the methodological difficulties to continue with functional and metabolic evaluation of *KI-Dnm2*^{R456W} mice under the exercise protocol, a different paradigm was proposed. An ischemic condition was temporarily applied to the mouse's leg using a cuff in the thigh. After 30 minutes, the cuff was quickly removed, causing a fast hyperemic response, when arteries and arterioles are dilated, minimizing its resistance. The ischemia-hyperemia paradigm allows the evaluation of the impact of capillaries regulation and structure in muscle blood perfusion after ischemic stress, allowing also the study of energetic metabolism under hypoxia and during the recovery period.

Materials and Methods

Animals

4 *KI-Dnm2*^{R456W} and 3 wild-type mice at 6 months of age and 3 *KI-Dnm2*^{R456W} mice at 3 months of age were evaluated functionally under the ischemia protocol. Mice were kindly supplied by Dr. Marc Bitoun, Institut de Myologie, and were kept under French rules for good animal care.

31P spectroscopy at rest

Phosphorus spectroscopy (³¹P MRS) at rest was collected before any perturbation in the muscle, with the same set-up used for the mpfNMR described in the previous pilot study. Three successive ³¹P acquisitions were collected (hard-pulse: 100μs, spectral width: 12 kHz, number of complex data points: 4000, TR: 2.5 sec, NR: 350). Localized shimming of water signal from the lower leg muscle volume (9x9x9 mm in general) allowed the acquisition of good quality ³¹P spectra (PCr line width of 10-25 Hz in the unfiltered ³¹P spectra).

Ischemia protocol

The methodology was similar to what was described in Chapter 3. After the acquisition of ^{31}P MRS at rest, the mpfNMR acquisition was launched for recording baseline muscle perfusion. After the measurements of muscle perfusion and ^{31}P MRS at rest, mice were submitted to ischemia of the left leg. Two surgical threads had been positioned subcutaneously around the thigh, and blood flow was interrupted by pulling tight the threads with the use of a 0.5 kg weight, leading to the occlusion of femoral artery (Bertoldi et al., 2008)(Bertoldi et al, 2008). After 30 minutes of ischemia, the blood flow was restored by the quick removal of the weight and loosening of the threads, causing a hyperemic response in the leg. The muscle perfusion and metabolism were monitored during the whole protocol, and the data were collected and analyzed as described for the previous pilot study and in Chapter 3.

Results

The ischemia protocol was successfully executed in 9 over 16 experiments: 3 3-month-old *KI-Dnm2^{R456W}* mice, 3 6-month-old *KI-Dnm2^{R456W}* mice, and 3 6-month-old wild-type mice. 2 *KI-Dnm2^{R456W}* mice died during the protocol. The ischemia was not effective in 3 mice, due to problems in the positioning of the threads. One exam was acquired with proper ischemia, but low hyperemia and no PCr depletion, so the exam was discarded. One acquisition was interrupted due to methodological problem. No statistical comparisons were done due to the small samples size.

^{31}P spectroscopy at rest

No major differences were observed in the ^{31}P spectroscopy at rest between 6 month-old *Dnm2* and wild-type mice, neither between 3 and 6 month-old *KI-Dnm2^{R456W}* mice (Table 5.4).

Table 5.4: 31P NMR spectroscopy at rest for the ischemia protocol.

	<i>KI-Dnm2</i> ^{R456W}		WT
	3 month-old (n=3)	6 month-old (n=3)	6 month-old (n=3)
PME/PCr	0.16 ± 0.08	0.19 ± 0.03	0.18 ± 0.11
PDE/PCr	0.04 ± 0.07	0.11 ± 0.06	0.06 ± 0.03
pH	7.11 ± 0.12	7.03 ± 0.15	7.04 ± 0.11
Pi/PCr	0.12 ± 0.08	0.20 ± 0.06	0.19 ± 0.06
PCr/ATP-γ	2.57 ± 0.39	2.69 ± 0.15	2.68 ± 0.25

PME: phosphomonoesters; PDE: phosphodiesters; Pi/PCr: proportional to ADP production rate; PCr/ATP-γ: proportional to the metabolically functional muscle tissue.

mpfNMR

For all mouse groups, muscle perfusion at rest was similar (Table 5.5). After prolonged ischemia, the perfusion profile in hyperemic response was similar for all mouse groups. Blood perfusion increased quickly after tourniquet release, and returned to basal levels in the recovery phase (Figure 5.4). Nevertheless, *KI-Dnm2*^{R465W} mice tended to achieve lower maximal and total perfusion than wild-type mice. Additionally, the maximal perfusion was observed later in the myopathic mice (Table 5.5).

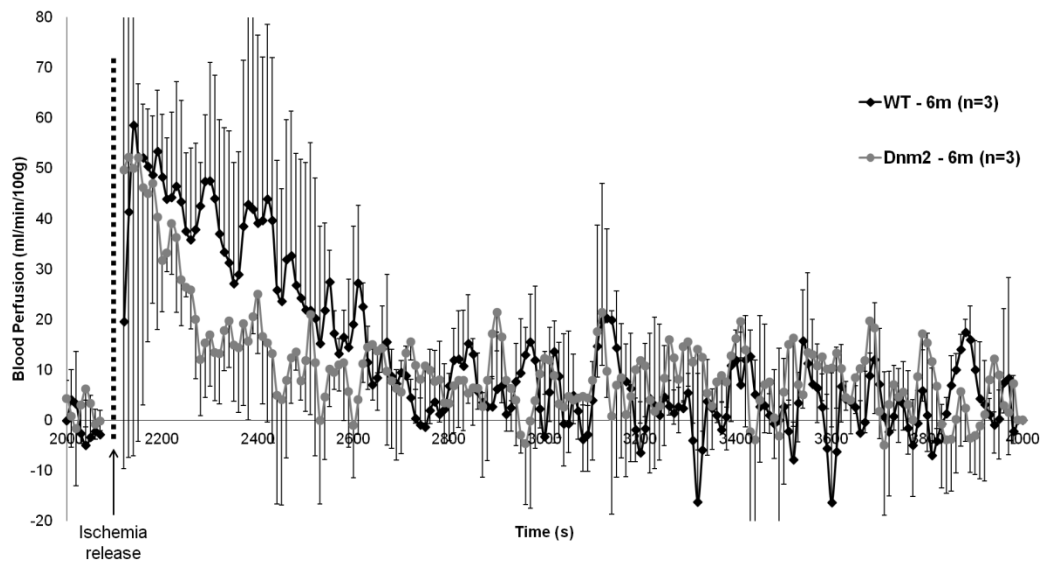
In the comparison between *KI-Dnm2*^{R456W} mice at different ages, maximum perfusion in 3 month-old mice tended to be lower than in 6 month-old mice (Figure 5.4-B).

Table 5.5: Perfusion data for *KI-Dnm2*^{R456W} (Dnm2) and wild-type (WT) mice.

	Dnm2		WT
	3 month-old (n=3)	6 month-old (n=3)	6 month-old (n=3)
Perf at rest	5.16 ± 1.94	7.61 ± 6.62	6.22 ± 1.50
MAX perf	44.23 ± 4.80	70.95 ± 43.66	85.02 ± 38.92
Time to peak (s)	284.67 ± 81.68	272.00 ± 93.66	215.00 ± 3.46
Total Perf	365.95 ± 202.10	340.91 ± 131.19	393.32 ± 194.96

Perfusion at rest (ml.min⁻¹.100g⁻¹), maximum perfusion after the cuff release (ml.min⁻¹.100g⁻¹), time to peak (seconds) and total perfusion (integral over time - 65 minutes) for 3- and 6-month-old *KI-Dnm2*^{R456W} mice and 6-month-old wild-type mice.

A) Old mice: Dnm2 X WT



B) Dnm2 mice: young X old

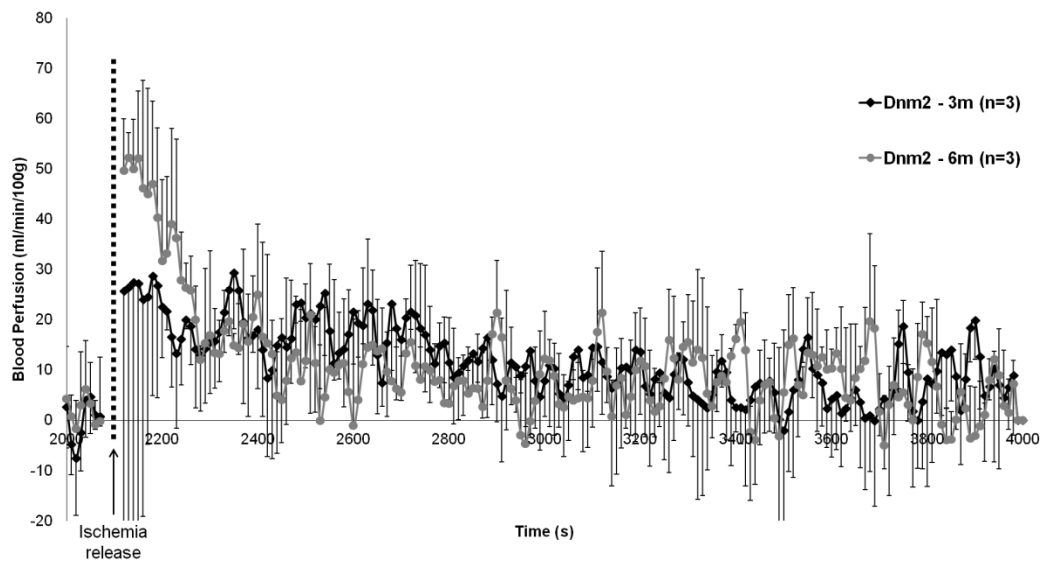


Figure 5.4: Perfusion profile after the cuff release for *KI-Dnm2*^{R456W} (Dnm2) and wild-type (WT) mice at 3 and 6 months of age. (A) Comparison between mouse strains, 6 month-old mice. (B) Comparison between 3 and 6 month-old *KI-Dnm2*^{R456W} mice.

Dynamic ^{31}P spectroscopy

Even if 9 mice could complete the mpfNMR ischemia protocol, only 4 mice depleted more than 50% of muscle PCr: the three 6-month-old wild-type mice and one 3-month-old *KI-Dnm2^{R456W}* mouse. All 6 month-old *KI-Dnm2^{R456W}* mice and two 3-month-old *KI-Dnm2^{R456W}* mice depleted a smaller amount of PCr (19-39%). No comparison could be done between *KI-Dnm2^{R456W}* and wild-type mice or between *KI-Dnm2^{R456W}* mice at different ages, since only one *KI-Dnm2^{R456W}* mouse achieved the minimal PCr depletion and there were no measurements from age-matched wild-type. It is possible, though, that the reduced PCr depletion observed in *KI-Dnm2^{R456W}* mice could be related to altered energetic metabolism under hypoxia in this mouse model, but more mice should be scanned to verify this hypothesis.

Discussion

When submitting *KI-Dnm2^{R456W}* mice to prolonged ischemia, a possible trend of reduced perfusion and impaired energetic metabolism in the affected mice was observed. This trend is consistent with the results from the previous pilot study, when muscle perfusion was measured after simulated exercise. To confirm if these possible functional or metabolic alterations are indeed present in the *KI-Dnm2^{R456W}* mice more animals should be analyzed.

Even if results were speculative, these pilot studies revealed methodological barriers to functional evaluation with exercise as muscle perturbation. In opposite, functional evaluation was feasible in the mouse model to centronuclear myopathy with mutation in dynamin-2 when ischemia was applied as muscle stress. Considering this, a third pilot study was proposed: the functional and metabolic evaluation of the muscle from *KI-Dnm2^{R456W}* mice after an acute lesion, using the ischemia-hyperemia paradigm.

Pilot study 3. Regeneration in the DNM2 mice: T1, T2 and functional analysis after injury

Even with the very small sample sizes, either when exercise or when ischemia were applied as perturbation to the muscle physiology, a tendency of reduced muscle perfusion possibly combined to impaired energetic metabolism might be present in the heterozygous *KI-Dnm2^{R456W}* mouse. There are indications that myotubular myopathy patients, with mutation in *MTM1*, have reduced population of satellite cells, which would lead to impaired muscle regeneration (Shichiji et al., 2013). A similar reduction in the number of satellite cells is observed in the *Mtm1-null* mouse (Lawlor et al., 2012). If the reduced number of satellite cells is a common feature in centronuclear myopathies, this population would be altered also in *KI-Dnm2^{R456W}* mice, impacting on the muscle regeneration after injury.

To access muscle function and metabolism in *KI-Dnm2^{R456W}* mice under muscle regeneration, the functional evaluation following ischemic stress was repeated in *KI-Dnm2^{R456W}* and wild-type after an acute electrically induced muscle injury. Our hypothesis was that if there were any impairment in muscle regeneration, it would be reflected by poorer metabolic and functional measurements. The purpose was to study the myopathic muscle under extreme conditions, when possible differences in muscle function and metabolism would be more evident.

Materials and Methods

Animals

Four *KI-Dnm2^{R456W}* mice and 5 wild-type littermates, females, 3 month-old, were evaluated. Mice were supplied by Dr. Marc Bitoun, and were kept under controlled environment, with 12/12 hours illumination cycle, with food and water at libidum, following the French rules for animal care.

Muscle Injury

Mice were anesthetized with isoflurane (5% for induction, 1.75% for maintenance, 1.5 l/min airflow) and the left gastrocnemius was shaved. The electrically induced damage was done by positioning two circular electrodes (7 mm diameter, 4 mm of distance between electrodes) covered with ultrasound transmission gel perpendicularly to muscle fibers, over the gastrocnemius muscle. Animals were submitted to 8 electrical pulses (voltage: 100V), with duration of 20 milliseconds and an interval of 0.5 second between pulses, in order to induce muscle damage.

NMR

The NMR evaluation consisted of T2 measurements of both limbs, followed by mpfNMR under and after ischemic stress and T1 measurements of the injured limb as described previously. Immediately after the NMR session, mice were euthanized by cervical dislocation under isoflurane anesthesia.

Three time points after muscle lesion were selected for this pilot study: 3, 5 and 10 days after injury. One *KI-Dnm2^{R456W}* and two wild-type mice were evaluated at 3 and at 5 days after injury; 2 *KI-Dnm2^{R456W}* and 2 wild-type mice were evaluated 10 days after injury. The interruption of the blood flow to the calf was not effective in both wild-type mice evaluated 3 days after muscle lesion. One of these mice was euthanized for the histological evaluation, and the second one was evaluated again at 10 days after injury.

Results

Muscle Perfusion

Perfusion at rest, maximal perfusion and total blood perfusion values after the tourniquet release are shown in Table 5.6. Perfusion at rest tended to be increased both in *KI-Dnm2^{R456W}* and wild-type mice up to the 5th day after muscle injury. Both lineages showed a decrease in the perfusion at rest from the 5th to the 10th day after muscle lesion, reaching values closer to the normal ones for each strain (Table 5.5). This apparently increased blood perfusion at rest may be related to the inflammatory

process observed in the acute response to the injury, which includes accentuated edema.

After tourniquet release, all mice showed increased perfusion, characterizing the hyperemic response. Nevertheless, *KI-Dnm2^{R456W}* mice tended to have a more accentuated increase in blood perfusion than wild-type mice, both at 5 and 10 days after injury (maximal perfusion in *KI-Dnm2^{R456W}* mice was 3 to 4 times higher than wild-type at the same time after injury). At 3 days after injury, there were no wild-type mice for the comparison (Figure 5.5).

At 5 days after injury, in addition to the increased maximal perfusion, *KI-Dnm2^{R456W}* presented higher total perfusion than wild-type. This was not maintained at 10 days after injury, when despite of the higher maximal perfusion in Dnm2 mice, no differences were evident in the total perfusion (Table 5.6).

Table 5.6. Perfusion at rest (Perf_{REST}), maximal perfusion (Perf_{MAX}) and total perfusion (Perf_{TOTAL}) after tourniquet release (ml.min⁻¹.100g⁻¹), 3-, 5- and 10-days after injury, for *KI-Dnm2^{R456W}* and wild-type mice.

		Perf _{REST}	Perf _{MAX}	Perf _{TOTAL}
	Dnm2 (n=1)	15.9 ± 9.1	202.5	1292.5
3 d	WT (n=2)	30.1 ± 1.3	--	--
	Dnm2 (n=1)	35.7 ± 11.7	233.9	2062.7
5 d	WT (n=2)	31.0 ± 28.6	75.7 ± 38.1	662.6 ± 198.5
	Dnm2 (n=2)	12.0 ± 3.2	229.3 ± 99.9	686.7 ± 133.5
10 d	WT (n=2)	4.6 ± 0.7	51.0 ± 20.1	669.7 ± 179.5

When the perfusion profiles were evaluated, a marked difference could be observed between *KI-Dnm2^{R456W}* and wild-type mice. Regardless of the moment after muscle injury, *KI-Dnm2^{R456W}* mice presented a high perfusion peak just after the tourniquet release, 3 to 4 times higher than the maximal perfusion achieved by wild-type mice. This initial peak was followed by a rapid decrease in blood perfusion, reaching values near to those observed in wild-type mice. The *KI-Dnm2^{R456W}* mice

evaluated 3 and 5 days after muscle injury apparently presented this first peak during a longer period than the *KI-Dnm2*^{R456W} mice evaluated 10 days after muscle injury (Figure 5.5).

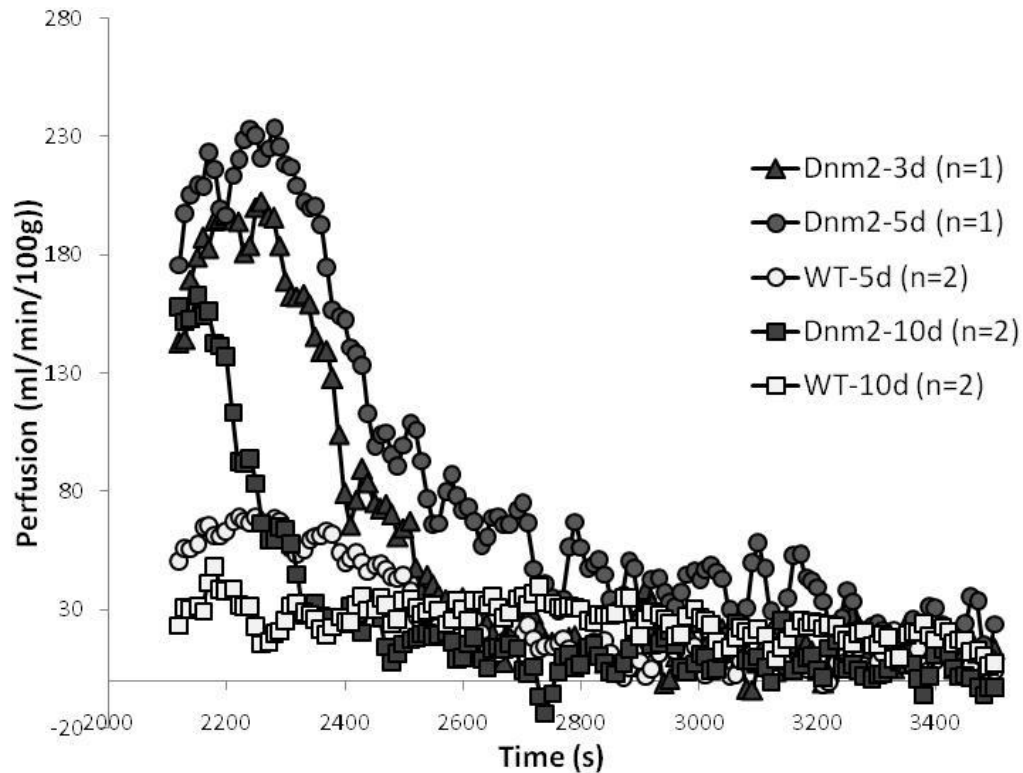


Figure 5.5. Blood perfusion profile for *KI-Dnm2*^{R456W} (Dnm2) and wild-type (WT) mice, 3-, 6- and 10-days after muscle injury. In all time points, *KI-Dnm2*^{R456W} mice presented a high initial perfusion peak, not observed in wild-type mice.

Muscle T2 evaluation after muscle injury

Muscle T2 reflected inflammatory and degenerative processes observed after acute lesion. Both *KI-Dnm2*^{R456W} and wild-type mice showed increased muscle T2 after muscle lesion. Increased T2 was confined to the posterior compartment of the leg: while muscle T2 was increased in gastrocnemius, no changes were observed in tibialis anterior muscle for both strains. The increase in muscle T2 was more accentuated up to 5 days after injury. Both *KI-Dnm2*^{R456W} and wild-type mice showed a tendency of returning to normal muscle T2 values with time. Nevertheless, until the

last time point evaluated (10 days after injury), the injured leg still showed increased T2 values in both mouse strains, indicating that the regeneration process was not completed even in the wild-type mice (Table 5.7).

Table 5.7. Muscle T2 (ms) for Gastrocnemius and Tibialis Anterior muscles at different time points after injury.

		Gastrocnemius		Tibialis Anterior	
		Injured	Contralateral	Injured	Contralateral
3 d	Dnm2 (n=1)	79.5 ± 0.9	32.9 ± 1.5	30.4	29.8
	WT (n=2)	91.0 ± 2.4	28.4 ± 0.6	27.5 ± 0.1	27.6 ± 0.5
5 d	Dnm2 (n=1)	112.5 ± 13.0	30.0 ± 0.6	30.3	29.7
	WT (n=2)	88.2 ± 23.0	28.9 ± 0.5	28.4 ± 0.1	28.1 ± 0.3
10 d	Dnm2 (n=2)	45.6 ± 1.8	30.8 ± 1.2	29.9 ± 0.3	29.3 ± 0.7
	WT (n=2)	40.6 ± 1.1	28.5 ± 0.5	27.9 ± 0.5	28.1 ± 0.0

Gastrocnemius: mean value for medial and lateral gastrocnemius. 3d, 5d, 10d: 3-, 5-, and 10-days after muscle injury in the posterior compartment of the leg.

Muscle T1 after acute muscle injury

Muscle T1 was measured only in the injured leg, due to the setup used for the images acquisition. A possibly reduced muscle T1 was observed in the first days after injury, showing a tendency to return to normal values with time. The same pattern was observed in *KI-Dnm2^{R456W}* and wild-type mice (Table 5.8).

Table 5.8. Muscle T1 (s), 3-, 5- and 10-days after muscle injury.

		Muscle T1 (s)
3 d	Dnm2 (n=1)	1.18
	WT (n=0)	--
5 d	Dnm2 (n=1)	1.27
	WT (n=2)	1.34 ± 0.09
10 d	Dnm2 (n=2)	1.43 ± 0.11
	WT (n=2)	1.41 ± 0.17

Discussion

Despite the small number of mice evaluated, this pilot study indicates for possible major differences between *KI-Dnm2^{R456W}* and wild-type mice during the regeneration process. These differences were particularly evidenced when regarding maximum perfusion after ischemia. All *KI-Dnm2^{R456W}* mice showed 3 to 4 times higher maximum perfusion than WT mice, at all time points studied. Such a high perfusion might indicate altered regulation of vascular control after ischemic stress. Interestingly, *KI-Dnm2^{R465W}* mice tended to present reduced total perfusion in the previous pilot studies, without muscle injury. A deeper evaluation of muscle regeneration and vascularization in *KI-Dnm2^{R465W}* mice would be interesting to better understand the disease mechanisms in this murine model.

In addition to the perfusion results, T2 measurements showed increased T2 in the injured muscle, with T2 approaching the normal values with time after injury for both strains. This was already expected, once muscle T2 is related to edema, necrosis and inflammation, which tend to be normalized approximately 15 days after injury (Baligand et al., 2012). Nevertheless, the evaluation of the time to return to normal T2 values could be an interesting non-invasive indicative of possibly altered regeneration in *KI-Dnm2^{R465W}* mice.

Even if this was a pilot study, with very few mice evaluated, the results indicate for major differences in muscle function during regeneration in *KI-Dnm2^{R465W}* mice. More mice should be evaluated to confirm these hypotheses.

Chapter 6

Evaluation of the potential use of micro-
Computed Tomography in the study of
muscles from murine models for muscle
dystrophies

Chapter 6. Evaluation of the potential use of micro-Computed Tomography in the study of muscles from murine models for muscle dystrophies

Introduction

Muscle imaging techniques such as computed tomography (CT) and nuclear magnetic resonance imaging (NMRI) have the capacity to assess the severity and identify patterns of muscle fatty infiltrative involvement in chronic muscle disorders. While NMR offers a wealth of other biomarkers (fibrosis, perfusion, energy metabolism) to characterize the skeletal muscle, CT scans offers the advantage of a lower cost of installation and maintenance. CT produces images with usually higher resolution but with less contrast for soft tissues than NMRI.

In human patients, CT images have been used in the evaluation of muscle disorders since the early 80s. Atrophy, fat infiltration and altered X-ray opacity was observed in affected muscles (Bulcke et al., 1981; Grindrod et al., 1983; Jiddane et al., 1983; Schwartz et al., 1988; Stern et al., 1984; Termote et al., 1980; De Visser and Verbeeten, 1985). In addition to the evaluation of muscle radiodensity, CT images can be used to estimate muscle volume and mass, variables that often correlate negatively with the disease progression (Nakayama et al., 2013a).

The development of high-resolution tomography (micro-CT) has permitted the acquisition of images from small animals. Mouse models for muscle dystrophies have already been studied with micro-CT, but the investigation were focused on the evaluation of bones, lung and airway alterations (Lopez et al., 2008; Novotny et al., 2011, 2014). To our knowledge, the description of muscle alterations in mice with micro-CT was restricted to the identification of atrophy (Manske et al., 2010; Weber et al., 2012).

In this context, our purpose was to evaluate how informative muscle micro-CT analysis could be in the study of mouse models for muscle dystrophy. Two severely affected mouse strains were scanned: *Large^{myd}* and the double mutant *mdx/Large^{myd}*

mice, in addition to wild-type mice. *Large*^{myd} mice have a mutation in the glycosyltransferase *Large* gene, which leads to poor glycosylation of the protein alpha-dystroglycan (α -DG) and altered link of the sarcolemma with the extracellular matrix (Grewal et al., 2001). The double mutant *mdx/Large*^{myd} mouse harbors mutations in the *Large* and in the dystrophin genes, resulting in total absence of the protein dystrophin, deficient glycosylation of α -DG and a very severe dystrophic phenotype (Martins et al., 2013). These two dystrophic strains present fibrosis, inflammation and necrosis in the muscle, in addition to regenerating fibers. Nevertheless, at variance with human patients, no fat infiltration is observed in muscles.

In this study, cross sectional area, muscle X-ray opacity and muscle signal heterogeneity in the micro-CT images were evaluated in the two dystrophic strains *Large*^{myd} and *mdx/Large*^{myd}, and compared to wild-type mice. In addition, we tested the efficacy of micro-CT images in the detection of the degeneration/regeneration process in a model of muscle damage induced by electroporation. Our micro-CT results confirmed that, even with increased resolution, micro-CT images are not sensitive enough to detect alterations observed in dystrophic and injured muscle other than changes in muscle volume, such as those related to inflammation, necrosis and fibrosis.

Materials and Methods

Animals

34 mice were scanned: 4 *mdx/Large*^{myd}; 12 *Large*^{myd} and 18 C57Black/6 mice (wild-type), aged between 2 and 6 months. 13 wild-type mice were scanned for the phenotype characterization, and 5 wild-type mice were scanned after muscle injury (3 mice scanned 3 days after injury, 2 mice scanned 15 days after injury). Mice were supplied by the Human Genome Research Center animal house, Bioscience Institute (Sao Paulo), and kept in controlled environment, with water and food *ad libitum*, 12 hours light/12 hours dark.

Muscle injury with electroporation

To better understand the effect of muscle lesions on the X-ray opacity, muscles of 5 wild-type mice (2 month-old) were injured by electroporation. Three mice were scanned 3 days after injury, when muscles are under an accentuated inflammatory process with edema, necrosis and inflammation, which would increase the muscle water content. Two mice were scanned 15 days after injury, when muscle was regenerating, with altered cytoarchitecture, characterized by smaller fibers with centrally placed nuclei. These time points were chosen based on previous results from the group (Vainzof et al., 2014), where marked differences could be detected in the histological analysis of normal murine muscle after electrically induced injury (Figure 6.1).

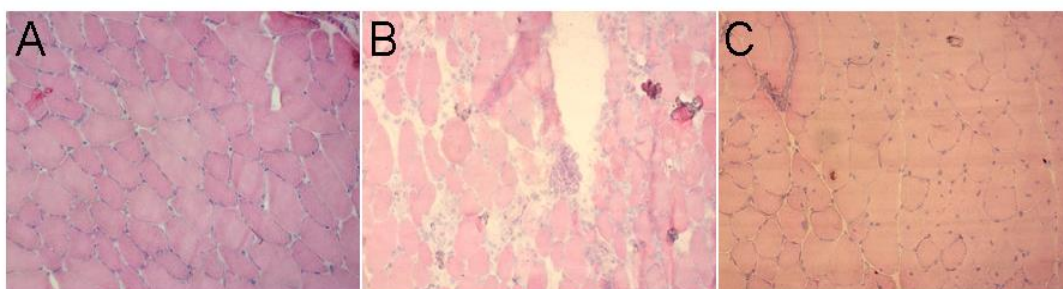


Figure 6.1. Normal murine muscle (A) in comparison to injured muscle in the acute phase after lesion (B - 3 days after injury) and when regeneration has overcome degeneration (C - 15 days after injury). H&E, zoom 200X. Adapted from (Vainzof et al., 2014).

Mice were anesthetized by intraperitoneal injection of 40 μ l of 2:1 ketamine 10% : xylazine 2% mixture. The left hindlimb was shaved and two circular electrodes with 0.7 mm diameter were positioned facing the posterior compartment of the lower leg, over the gastrocnemius muscles, with a 4 mm distance between them, and covered with electroconductive gel. Eight unipolar pulses of 100V, with 20 ms duration and 500 ms interval, were applied to induce muscle injury

Micro-CT

Mice were anesthetized with 4% isoflurane, and anesthesia was maintained with 1.75% isoflurane mixed with oxygen, in a 1 L/min gas flow. Then, mice were prone positioned with the posterior limbs symmetrically extended for the micro-CT scans. During all the scan time, the mice breathing rate was monitored by video. After images acquisition, all mice were euthanized in CO₂ chamber, and muscles were collected for further posterior histological, protein or molecular analyses.

Micro-CT scans were performed in a micro-tomography system (SkyScan 1176 in vivo micro-CT, SkyScan, Kontich, Belgium). Scanning parameters were: 50 kV, 500 mA; Filter Al 0.5 mm; voxel volume 18 mm³. The acquisition time was 13 minutes, and experiment time never exceeded 30 minutes, including mouse positioning.

Projection images were reconstructed with the NRecon Reconstruction Software, provided by the manufacturer (SkyScan). Reconstructed images were smoothed (smooth factor=3, Gaussian function); ring and beam hardening artifacts were corrected (ring reduction factor: 10%; beam hardening correction factor: 19%). All images were reconstructed over the same dynamic range, resulting in identical gray scales.

Data Analysis

The images were analyzed with the CT-Analyser Software (SkyScan). Tibia length (L_{tibia}) was measured and one transversal slice was selected at approximately $\frac{1}{4}$ of the tibia length from the knee to the feet, where no fat from the popliteal region was visible. On that slice, the cross-section area (CSA) was measured, and the ratio $\text{CSA}/L_{\text{tibia}}$ was compared as an index of atrophy. In the same image, one ROI was drawn comprising the muscles from the posterior compartment of the lower leg (gastrocnemius and soleus), excluding any fat, skin and bone tissue. A second ROI was drawn in the empty space to estimate the noise. The histogram of grayscale values inside muscle ROI was evaluated. While mean intensity identifies changes in

radiodensity in the whole tissue, the ratio $SD_{\text{signal}}/SD_{\text{noise}}$ (SD: standard deviation) inside the muscle ROI was used as a measurement of the muscle signal heterogeneity.

Statistical Analysis

The analyses were done with one-way ANOVA, with Bonferroni comparison of means when necessary (NCSS 2001, Kaysville, Utah, USA). Differences were considered significant if $p < 0.05$. Muscle radiodensity and signal heterogeneity data are reported as mean \pm SD.

Results

Phenotypical characterization of the dystrophic muscle with micro-CT

No differences in the radiodensity were detected in the comparison between male and female mice or between mice with different age from the same strain, both for wild-type and *Large^{myd}* mice. Considering this, all mice from each strain were grouped for further analysis.

In the comparison between mouse strains, a marked difference related to atrophy was observed (Figure 6.2). CSA/L_{tibia} was different between the three mouse lineages ($p < 0.01$), being reduced in the more affected *mdx/Large^{myd}* mice when compared to wild-type, while *Large^{myd}* mice showed intermediary values (Table 6.1). Nevertheless, when comparing intensity and heterogeneity of muscle signal, the differences observed between the groups were not considered significant: among 256 tones in the grayscale, the differences were of the order of one tone (Table 6.1).

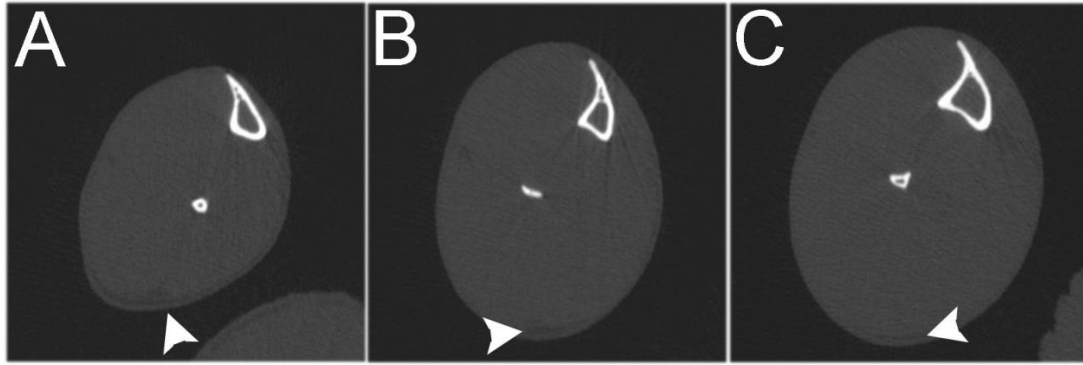


Figure 6.2. Transversal reconstructed micro-CT images from (A) *mdx/Large^{myd}*, (B) *Large^{myd}* and (C) wild-type mice. Apart from atrophy, no difference was identified in the muscle signal for the three strains. The arrowheads show the subcutaneous fat, with reduced signal in comparison to muscle and skin.

Table 6.1. Micro-CT results for *mdx/Large^{myd}*, *Large^{myd}* and wild-type mice.

	X-ray opacity (GS)	Heterogeneity (SD_{signal}/SD_{noise} - GS)	CSA/L_{tibia} ** (mm)
<i>mdxLarge^{myd}</i> (n=4)	27.6 ± 0.2	2.4 ± 0.3	96.3 ± 13.9
<i>Large^{myd}</i> (n=12)	27.6 ± 0.2	2.1 ± 0.2	121.7 ± 22.8
Wild-type (n=13)	27.8 ± 0.2	2.0 ± 0.1	143.4 ± 22.6

CSA: cross section area; L_{tibia}: tibia length; GS: grayscale; SD: standard deviation; px: pixels.

Evaluation of injured muscle with micro-CT

This pilot study was conducted to evaluate if an acute and severe muscle lesion would create alterations that could be detected with micro-CT images. While murine dystrophic muscle presents mainly necrosis, infiltrates of inflammatory cells and fibrosis, normal murine muscle presents accentuated inflammation and necrosis in the acute phase after injury, with important edema observed 3 days after lesion (Figure 6.1-B). After 15 days, injured muscle shows predominance of smaller regenerating fibers, identifiable by the centrally placed nuclei (Figure 6.1-C). Three

mice were scanned 3 days after injury, and 2 mice were scanned 15 days after injury. Injured leg was compared to the contralateral leg from the same mouse. Due to the small number of mice studied, no statistical analysis was done.

In both time points, injured leg tended to show increased CSA/L_{tibia}, compatible with the edema induced by muscle lesion. A slightly reduced X-ray opacity was observed in the injured leg in the acute phase after lesion. This can be caused by the higher amount of water present in the tissue due to edema, which would reduce its global radiodensity. In the second time point (15 days after injury), no differences were observed in X-ray opacity or signal heterogeneity between injured and control legs, even if muscle cytoarchitecture is changed in the histological analysis (Table 6.2).

Table 6.2. Effect of muscle injury after 3 and 15 days in the micro-CT results.

	Muscle	X-ray opacity (GS)	Heterogeneity (SD _{signal} /SD _{noise} - GS)	CSA/L _{tibia} (mm)
3 days after injury (n=3)	Injured	27.4 ± 0.3	2.1 ± 0.3	163.7 ± 6.2
	Control	28.4 ± 0.0	2.0 ± 0.0	139.9 ± 10.1
15 days after injury (n=2)	Injured	28.1 ± 0.2	2.0 ± 0.0	132.5 ± 0.8
	Control	28.4 ± 0.1	2.0 ± 0.0	115.5 ± 6.6

CSA: cross section area; L_{tibia}: tibia length; GS: grayscale; SD: standard deviation; px: pixels.

Discussion

In this study, we have shown that micro-CT images can identify muscle atrophy, but not major alterations in the muscle content in mice. Two severely affected mouse strains were scanned, *Large^{myd}* and the double mutant *mdx/Large^{myd}* mice. Both strains present severe muscle dystrophy, with necrosis, inflammatory infiltration and fibrosis in the histological analysis. These dystrophic mice showed

atrophy in micro-CT images, as already described in morphological studies (Lane et al., 1975; Martins et al., 2013). Nevertheless, the dystrophic alterations in the muscles were not reflected by muscle X-ray opacity or muscle signal heterogeneity. In the evaluation of injured muscle from normal mice, the presence of edema, necrosis and inflammation tended to be reflected by reduced muscle X-ray opacity in the acute phase after lesion.

In humans, the quantitative evaluation of muscle radiodensity shows reduced muscle signal usually related to the fat replacement observed in muscle dystrophies, polymyositis and neurogenic disorders (Bilgen et al., 2001; Swash et al., 1995; Vlaskovits et al., 2000). Duchenne and Becker muscular dystrophies patients present alterations in muscle radiodensity in CT images even in early stages of the disease, and the CT numbers (X-ray opacity) decrease with the advance of the disease (Arai et al., 1995). Not only the absolute CT values, but the histogram of the muscle radiodensity also changed with disease progression in patients with Duchenne muscular dystrophy, evidencing the increase in the fat content in the muscles (Nakayama et al., 2013b). In opposite, patients with Pompe disease showed high density in liver and skeletal muscles in CT scans, compatible with the glycogen accumulation in these tissues, that tend to get closer to normal values after treatment (Ishigaki et al., 2012). This indicated that fat replacement is not the only factor influencing changes in the muscle radiodensity in CT images.

Micro-CT studies of dystrophic mice have so far focused on the evaluation of bone structure and architecture, extracting information such as trabecular bone morphometry, cortical bone geometry and volumetric bone density (Novotny et al., 2011, 2014). The low-coefficient of X-ray attenuation of soft tissues, such as muscle, limits the visualization of internal details in CT or micro-CT images. The use of micro-CT in the study of soft tissue has been developed recently, but with techniques that include decalcification, dehydration and/or the use of contrast agents in *ex-vivo* specimens. When the soft-tissue had been previously treated, *ex-vivo* contrast enhanced micro-CT allowed the visualization of muscle structures, achieving resolution down to the level of skeletal muscle fibers, close to the histological resolution (Aoyagi et al., 2013; Baverstock et al., 2013; Jeffery et al., 2011; Metscher, 2009).

The *in vivo* evaluation of mouse muscle with micro-CT was still limited to a few studies. Contrast-enhanced micro-CT allowed the cardiac evaluation of living mice (Badea et al., 2006). Muscle loss after botulin toxin injection and in sarcopenia condition in mice was described by measuring the muscle cross section area from micro-CT images (Manske et al., 2010; Weber et al., 2012). Micro-CT images of the *Tnt^{mdm}* mouse, model for muscle dystrophy with myositis, showed skeletal anomalies in the spine and thoracic rib cage in addition to reduction of lung volume. In addition to morphological, histological and molecular data, these micro-CT results supported the hypothesis of early mechanical diaphragm dysfunction in this murine model (Lopez et al., 2008).

In general, mouse models to muscle dystrophies do not present fat infiltration in the muscles as human patients do (Carnwath and Shotton, 1987; McIntosh et al., 1998b). This is the case for the two dystrophic mouse strains evaluated in this study, including the very severely affected *mdx/Large^{myd}* mouse, in which the major dystrophic alterations observed in histological analysis are necrosis, inflammation and fibrosis (Martins et al., 2013). They remained undetected by micro-CT imaging. Our results support the hypothesis that muscle alterations might possibly be evidenced in micro-CT images only in very extreme conditions, such as the acute phase after extensive electrically induced muscle damage.

In conclusion, these preliminary results showed that micro-CT images can identify muscle atrophy in mouse model for muscular dystrophy. However, even if CT images identified alterations in muscle composition in dystrophic human patients, it was not possible to reach the same in murine models with micro-CT images. It is possible though that with the use of proper contrast agents new avenues could be opened in the evaluation of murine soft tissue with micro-CT.

General Conclusions and Perspectives

General Conclusions and Perspectives

In this thesis, different mouse models for genetic muscle diseases were non-invasively characterized, with innovative techniques for data acquisition and analyses. The combined use of magnetic resonance imaging and texture analysis allowed the identification of subtle differences in three dystrophic mouse models with variable degree of muscle involvement: the *mdx* mouse, with absence of the protein dystrophin, functionally and histologically mildly altered model for Duchenne muscular dystrophy; the *Large^{myd}* mouse, with defective glycosylation of the protein α -DG and severe phenotype, model for congenital muscular dystrophy 1D; and the double mutant *mdx/Large^{myd}*, with both mutations and a very severe phenotype. Different patterns of distribution of muscle alterations according to the mutation could be detected in these murine models. Even if the images were acquired in a 2T magnet, this somewhat extends to murine models for muscle dystrophies what is observed in human patients, where the pattern of muscle involvement varies according to the primary genetic mutation.

In addition to the ability to identify different muscle phenotypes, these results reveal that NMR can be sensitive enough to identify pre-clinical alterations in mouse models for genetic muscle disorders even when no major phenotypical or histological changes can be detected. With functional multiparametric NMR, it was possible to detect age-related alterations in muscle blood perfusion in the widely studied *mdx* dystrophic mouse. These alterations could be observed even in young-adult mice, when no vascular alterations were visible in the histological analysis. The NMR data unraveled changes in the muscle function, raising questions about the impact of pericytes and vascular alterations in the dystrophy disease mechanisms.

Despite technical difficulties, NMR morphologic evaluation and relaxometry identified alterations in the *KI-Dnm2^{R465W}* mouse, model for autosomal dominant centronuclear myopathy, which presents only mild phenotypical and histological alterations. The continuation of the functional and metabolic evaluation of this mouse

model could put light on the disease mechanisms and the phenotypical differences in the mouse model when compared to human patients.

All the four evaluated murine models for genetic muscle disorders presented two common features: increased muscle T2 and absence of fat infiltration. This was observed even in early stages of muscle involvement, and in the presence of mild phenotypes such as the *KI-Dnm2*^{R465W} mouse. An increase in muscle T2 is also observed in dystrophic and in some myopathic patients, being related to necrosis and inflammation in early stages of muscle involvement, and to fat infiltration in late stages of the disease, when the degenerated muscle has been replaced by adipose tissue.

While the three studied dystrophic mice presented necrosis and an important inflammatory process, the mouse model to centronuclear myopathy displayed only altered distribution of organelles in the sarcoplasm, namely mitochondria and nuclei of a few percentage of muscle fibers. These observations support the hypothesis that even if no fat infiltration, necrosis or inflammation were observed in genetic muscle disorders, alterations in muscle structure and physiology could result in increased muscle T2. Despite the fact that increased muscle T2 could not be related to specific histopathological changes, it allowed the evaluation of muscle involvement at the tissue level, different from standard histological analyses that usually evaluate small muscle specimens.

Additionally, high resolution computed tomography was used in the search for alterations in the muscle of murine models for muscle dystrophies. Muscle atrophy could be detected in the dystrophic *Large*^{myd} and *mdx/Large*^{myd} mice. However, even if alterations in muscle X-ray opacity in human patients were already described, no differences could be observed in the intensity or heterogeneity of muscle signal in the dystrophic strains. In the acute phase after muscle injury in control mice, a tendency of reduced X-ray opacity may be present. These results support the hypothesis that major alterations, such as accentuated inflammation and edema, must be present to allow the identification of changes in muscle X-ray opacity in mice. In addition to the reduced dimensions, the absence of fat infiltration in the murine dystrophic muscle disabled the identification of differences in micro-CT signal intensity and heterogeneity.

In summary, this thesis contributed to the expansion of the basic phenotypical characterization of mouse models for muscle genetic disorders with non-invasive techniques. This is an essential step prior to the use of non-invasive techniques as outcome measures in pre-clinical studies for therapeutic protocols. Because of its non-traumatic and non-invasive character, these methods have great potential as outcome measure in pre-clinical studies in mouse models for genetic muscle disorders. In special, NMR gives reproducible, sensitive and objective results from morphological, functional and metabolic approaches, allowing early identification of subtle muscle alterations in longitudinal studies. This is highly valuable in clinical and pre-clinical therapeutic protocols, making it a good predictor of muscle functional improvement.

The translation of the non-invasive methods used in this thesis to human patients is almost direct. Non-invasive outcome measures are essential in clinical trials and in the follow-up of dystrophic and myopathic patients. Reducing invasive and painful proceedings such as biopsies can improve the quality of life for these patients, who can be already under severe disease conditions. In parallel to the development of new therapeutic approaches, there is an increasing interest in non-invasive and non-traumatic tools to access any benefice in patients.

Finally, this thesis comprised an important transfer of knowledge in the field of non-invasive evaluation of murine models for genetic diseases. For the first time, the muscle of mouse models for different forms of genetic muscle diseases was evaluated non-invasively in Brazil with NMR and micro-CT, thanks to the close collaboration developed between the Brazilian and French research groups.

Bibliography

- Ahmad, N., Welch, I., Grange, R., Hadway, J., Dhanvantari, S., Hill, D., Lee, T.-Y., and Hoffman, L.M. (2011). Use of imaging biomarkers to assess perfusion and glucose metabolism in the skeletal muscle of dystrophic mice. *BMC Musculoskelet. Disord.* *12*, 127.
- Aleman, M., Riehl, J., Aldridge, B. M., Lecouteur, L. A., Stott, J. L. & Pessah, I. N. (2004) Association of a mutation in the ryanodine receptor 1 gene with equine malignant hyperthermia. *Muscle & nerve.* *30*, 356–365.
- Allamand, V., and Campbell, K.P. (2000). Animal models for muscular dystrophy: valuable tools for the development of therapies. *Hum. Mol. Genet.* *9*, 2459–2467.
- Amthor, H., Egelhof, T., McKinnell, I., Ladd, M.E., Janssen, I., Weber, J., Sinn, H., Schrenk, H.-H., Forsting, M., Voit, T., et al. (2004). Albumin targeting of damaged muscle fibres in the *mdx* mouse can be monitored by MRI. *Neuromuscul. Disord.* *14*, 791–796.
- Ando, J., and Kamiya, A. (1992). Blood flow and vascular endothelial cell function. *Front. Med. Biol. Eng. Int. J. Jpn. Soc. Med. Electron. Biol. Eng.* *5*, 245–264.
- Aoyagi, H., Iwasaki, S., and Nakamura, K. (2013). Three-dimensional observation of mouse tongue muscles using micro-computed tomography. *Odontology* 1–8.
- Arai, Y., Osawa, M., and Fukuyama, Y. (1995). Muscle CT scans in preclinical cases of Duchenne and Becker muscular dystrophy. *Brain Dev.* *17*, 95–103.
- Araishi, K., Sasaoka, T., Imamura, M., Noguchi, S., Hama, H., Wakabayashi, E., Yoshida, M., Hori, T., and Ozawa, E. (1999). Loss of the sarcoglycan complex and sarcospan leads to muscular dystrophy in β -sarcoglycan-deficient mice. *Hum. Mol. Genet.* *8*, 1589–1598.
- Araujo, E.C., Fromes, Y., and Carlier, P.G. (2014). New Insights on Human Skeletal Muscle Tissue Compartments Revealed by In Vivo T2 NMR Relaxometry. *Biophys. J.* *106*, 2267–2274.
- Arpan, I., Forbes, S.C., Lott, D.J., Senesac, C.R., Daniels, M.J., Triplett, W.T., Deol, J.K., Sweeney, H.L., Walter, G.A., and Vandenborne, K. (2013). T2 mapping provides multiple approaches for the characterization of muscle involvement in neuromuscular diseases: a cross-sectional study of lower leg muscles in 5–15-year-old boys with Duchenne muscular dystrophy. *NMR Biomed.* *26*, 320–328.
- Arsic, N., Zacchigna, S., Zentilin, L., Ramirez-Correa, G., Pattarini, L., Salvi, A., Sinagra, G., and Giacca, M. (2004). Vascular endothelial growth factor stimulates skeletal muscle regeneration in vivo. *Mol. Ther.* *10*, 844–854.

- Asai, A., Sahani, N., Kaneki, M., Ouchi, Y., Martyn, J.J., and Yasuhara, S.E. (2007). Primary role of functional ischemia, quantitative evidence for the two-hit mechanism, and phosphodiesterase-5 inhibitor therapy in mouse muscular dystrophy. *PLoS One* 2, e806.
- Bachmann, G., Damian, M.S., Koch, M., Schilling, G., Fach, B., and Stöppler, S. (1996). The clinical and genetic correlates of MRI findings in myotonic dystrophy. *Neuroradiology* 38, 629–635.
- Badea, C.T., Bucholz, E., Hedlund, L.W., Rockman, H.A., and Johnson, G.A. (2006). Imaging methods for morphological and functional phenotyping of the rodent heart. *Toxicol. Pathol.* 34, 111–117.
- Bagher, P., Duan, D., and Segal, S.S. (2011). Evidence for impaired neurovascular transmission in a murine model of Duchenne muscular dystrophy. *J. Appl. Physiol.* 110, 601–609.
- Baligand, C., Gilson, H., Menard, J.C., Schakman, O., Wary, C., Thissen, J.-P., and Carlier, P.G. (2009). Functional assessment of skeletal muscle in intact mice lacking myostatin by concurrent NMR imaging and spectroscopy. *Gene Ther.* 17, 328–337.
- Baligand, C., Wary, C., Menard, J.C., Giacomini, E., Hogrel, J.-Y., and Carlier, P.G. (2011). Measuring perfusion and bioenergetics simultaneously in mouse skeletal muscle: a multiparametric functional-NMR approach. *NMR Biomed.* 24, 281–290.
- Baligand, C., Jouvion, G., Schakman, O., Gilson, H., Wary, C., Thissen, J.-P., and Carlier, P.G. (2012). Multiparametric functional nuclear magnetic resonance imaging shows alterations associated with plasmid electrotransfer in mouse skeletal muscle. *J. Gene Med.* 14, 598–608.
- Barresi, R., and Campbell, K.P. (2006). Dystroglycan: from biosynthesis to pathogenesis of human disease. *J. Cell Sci.* 119, 199–207.
- Baverstock, H., Jeffery, N.S., and Cobb, S.N. (2013). The morphology of the mouse masticatory musculature. *J. Anat.* 223, 46–60.
- Beggs, A.H., Böhm, J., Snead, E., Kozlowski, M., Maurer, M., Minor, K., Childers, M.K., Taylor, S.M., Hitte, C., Mickelson, J.R., et al. (2010). MTM1 mutation associated with X-linked myotubular myopathy in Labrador Retrievers. *Proc. Natl. Acad. Sci.* 107, 14697–14702.
- Buj-Bello, A., Laugel, V., Messaddeq, N., Zahreddine, H., Laporte, J., Pellissier, J.-F., and Mandel, J.-L. (2002). The lipid phosphatase myotubularin is essential for skeletal muscle maintenance but not for myogenesis in mice. *Proc. Natl. Acad. Sci.* 99, 15060–15065.
- Bertoldi, D., Loureiro de Sousa, P., Fromes, Y., Wary, C., and Carlier, P.G. (2008). Quantitative, dynamic and noninvasive determination of skeletal muscle perfusion in

mouse leg by NMR arterial spin-labeled imaging. *Magn. Reson. Imaging* 26, 1259–1265.

Bilgen, C., Bilgen, I.G., and Sener, R.N. (2001). Oculopharyngeal muscular dystrophy: clinical and CT findings. *Comput. Med. Imaging Graph.* 25, 527–529.

Bitoun, M., Maugenre, S., Jeannet, P.-Y., Lacène, E., Ferrer, X., Laforêt, P., Martin, J.-J., Laporte, J., Lochmüller, H., Beggs, A.H., et al. (2005). Mutations in dynamin 2 cause dominant centronuclear myopathy. *Nat. Genet.* 37, 1207–1209.

Bitoun, M., Bevilacqua, J.A., Prudhon, B., Maugenre, S., Taratuto, A.L., Monges, S., Lubieniecki, F., Cances, C., Uro-Coste, E., Mayer, M., et al. (2007). Dynamin 2 mutations cause sporadic centronuclear myopathy with neonatal onset. *Ann. Neurol.* 62, 666–670.

Böhm, J., Vasli, N., Maurer, M., Cowling, B., Shelton, G.D., Kress, W., Toussaint, A., Prokic, I., Schara, U., Anderson, T.J., et al. (2013). Altered Splicing of the BIN1 Muscle-Specific Exon in Humans and Dogs with Highly. *PLoS Genet.* 9, e003430.

Boncompagni, S., Rossi, A.E., Micaroni, M., Hamilton, S.L., Dirksen, R.T., Franzini-Armstrong, C., and Protasi, F. (2009). Characterization and temporal development of cores in a mouse model of malignant hyperthermia. *Proc. Natl. Acad. Sci.* 106, 21996–22001.

Borrelli, O., Salvia, G., Mancini, V., Santoro, L., Tagliente, F., Romeo, E.F., and Cucchiara, S. (2005). Evolution of gastric electrical features and gastric emptying in children with Duchenne and Becker muscular dystrophy. *Am. J. Gastroenterol.* 100, 695–702.

Bradley, W.G., O'Brien, M.D., Walder, D.N., Murchison, D., Johnson, M., and Newell, D.J. (1975). Failure to confirm a vascular cause of muscular dystrophy. *Arch. Neurol.* 32, 466.

Brenman, J.E., Chao, D.S., Xia, H., Aldape, K., and Bredt, D.S. (1995). Nitric oxide synthase complexed with dystrophin and absent from skeletal muscle sarcolemma in Duchenne muscular dystrophy. *Cell* 82, 743–752.

Bresolin, N., Castelli, E., Comi, G.P., Felisari, G., Bardoni, A., Perani, D., Grassi, F., Turconi, A., Mazzucchelli, F., Gallotti, D., et al. (1994). Cognitive impairment in Duchenne muscular dystrophy. *Neuromuscul. Disord.* 4, 359–369.

Brunelli, S., Sciorati, C., D'Antona, G., Innocenzi, A., Covarello, D., Galvez, B.G., Perrotta, C., Monopoli, A., Sanvito, F., Bottinelli, R., et al. (2007). Nitric oxide release combined with nonsteroidal antiinflammatory activity prevents muscular dystrophy pathology and enhances stem cell therapy. *Proc. Natl. Acad. Sci.* 104, 264–269.

Buckland, K.F., and Gaspar, B.H. (2014). Gene and cell therapy for children—New medicines, new challenges? *Adv. Drug Deliv. Rev.* 73, 162–169.

- Bulcke, J.A., Crolla, D., Termote, J.-L., Baert, A., Palmers, Y., and van den Bergh, R. (1981). Computed tomography of muscle. *Muscle Nerve* 4, 67–72.
- Bulfield, G., Siller, W.G., Wight, P.A., and Moore, K.J. (1984). X chromosome-linked muscular dystrophy (mdx) in the mouse. *Proc. Natl. Acad. Sci.* 81, 1189–1192.
- Burch, T.G., Prewitt, R.L., and Law, P.K. (1981). In vivo morphometric analysis of muscle microcirculation in dystrophic mice. *Muscle Nerve* 4, 420–424.
- Carnwath, J.W., and Shotton, D.M. (1987). Muscular dystrophy in the mdx mouse: Histopathology of the soleus and extensor digitorum longus muscles. *J. Neurol. Sci.* 80, 39–54.
- Catteruccia, M., Fattori, F., Codemo, V., Ruggiero, L., Maggi, L., Tasca, G., Fiorillo, C., Pane, M., Berardinelli, A., Verardo, M., et al. (2013). Centronuclear myopathy related to dynamin 2 mutations: clinical, morphological, muscle imaging and genetic features of an Italian cohort. *Neuromuscul. Disord.* 23, 229–238.
- Childers, M.K., Joubert, R., Poulard, K., Moal, C., Grange, R.W., Doering, J.A., Lawlor, M.W., Rider, B.E., Jamet, T., Danièle, N., et al. (2014). Gene therapy prolongs survival and restores function in murine and canine models of myotubular myopathy. *Sci. Transl. Med.* 6, 220ra10.
- Christov, C., Chrétien, F., Abou-Khalil, R., Bassez, G., Vallet, G., Authier, F.-J., Bassaglia, Y., Shinin, V., Tajbakhsh, S., Chazaud, B., et al. (2007). Muscle satellite cells and endothelial cells: close neighbors and privileged partners. *Mol. Biol. Cell* 18, 1397–1409.
- Claire, W., Naulet, T., Thibaud, J.-L., Monnet, A., Blot, S., and Carlier, P.G. (2012). Splitting of Pi and other ³¹P NMR anomalies of skeletal muscle metabolites in canine muscular dystrophy. *NMR Biomed.* 25, 1160–1169.
- Clifford, P.S., and Hellsten, Y. (2004). Vasodilatory mechanisms in contracting skeletal muscle. *J. Appl. Physiol.* 97, 393–403.
- Cole, M.A., Rafael, J.A., Taylor, D.J., Lodi, R., Davies, K.E., and Styles, P. (2002). A quantitative study of bioenergetics in skeletal muscle lacking utrophin and dystrophin. *Neuromuscul. Disord.* 12, 247–257.
- Crosbie, R.H., Barresi, R., and Campbell, K.P. (2002). Loss of sarcolemma nNOS in sarcoglycan-deficient muscle. *FASEB J. Off. Publ. Fed. Am. Soc. Exp. Biol.* 16, 1786–1791.
- Dalkilic, I., and Kunkel, L.M. (2003). Muscular dystrophies: genes to pathogenesis. *Curr. Opin. Genet. Dev.* 13, 231–238.
- Dangain, J., and Vrbova, G. (1984). Muscle development in mdx mutant mice. *Muscle Nerve* 7, 700–704.

- Davies, K.E., and Nowak, K.J. (2006). Molecular mechanisms of muscular dystrophies: old and new players. *Nat. Rev. Mol. Cell Biol.* 7, 762–773.
- Deasy, B.M., Feduska, J.M., Payne, T.R., Li, Y., Ambrosio, F., and Huard, J. (2009). Effect of VEGF on the regenerative capacity of muscle stem cells in dystrophic skeletal muscle. *Mol. Ther.* 17, 1788–1798.
- Deconinck, N., and Dan, B. (2007). Pathophysiology of duchenne muscular dystrophy: current hypotheses. *Pediatr. Neurol.* 36, 1–7.
- Deconinck, A.E., Rafael, J.A., Skinner, J.A., Brown, S.C., Potter, A.C., Metzinger, L., Watt, D.J., Dickson, J.G., Tinsley, J.M., and Davies, K.E. (1997). Utrophin-dystrophin-deficient mice as a model for Duchenne muscular dystrophy. *Cell* 90, 717–727.
- Desguerre, I., Mayer, M., Leturcq, F., Barbet, J.-P., Gherardi, R.K., and Christov, C. (2009). Endomysial fibrosis in Duchenne muscular dystrophy: a marker of poor outcome associated with macrophage alternative activation. *J. Neuropathol. Exp. Neurol.* 68, 762–773.
- Detombe, S.A., Dunmore-Buyze, J., and Drangova, M. (2012). Evaluation of eXIA 160XL cardiac-related enhancement in C57BL/6 and BALB/c mice using micro-CT. *Contrast Media Mol. Imaging* 7, 240–246.
- Dubowitz, V. (2004). Therapeutic efforts in Duchenne muscular dystrophy; the need for a common language between basic scientists and clinicians. *Neuromuscul. Disord.* 14, 451–455.
- Dubowitz, V., Sewry, C.A., and Oldfors, A. (2013). *Muscle Biopsy: A Practical Approach* (Elsevier Health Sciences).
- Duclos, F., Straub, V., Moore, S.A., Venzke, D.P., Hrstka, R.F., Crosbie, R.H., Durbeej, M., Lebakken, C.S., Ettinger, A.J., Van Der Meulen, J., et al. (1998). Progressive muscular dystrophy in α -sarcoglycan-deficient mice. *J. Cell Biol.* 142, 1461–1471.
- Dunn, J.F., and Zaim-Wadghiri, Y. (1999). Quantitative magnetic resonance imaging of the mdx mouse model of Duchenne muscular dystrophy. *Muscle Nerve* 22, 1367–1371.
- Dunn, J.F., Frostick, S., Brown, G., and Radda, G.K. (1991). Energy status of cells lacking dystrophin: an in vivo/in vitro study of mdx mouse skeletal muscle. *Biochim. Biophys. Acta BBA-Mol. Basis Dis.* 1096, 115–120.
- Dunn, J.F., Tracey, I., and Radda, G.K. (1993). Exercise Metabolism in Duchenne Muscular Dystrophy: A Biochemical and ³¹P-nuclear Magnetic Resonance Study of mdx Mice. *Proc. R. Soc. Lond. B Biol. Sci.* 251, 201–206.

- Durieux, A.-C., Vignaud, A., Prudhon, B., Viou, M.T., Beuvin, M., Vassilopoulos, S., Fraysse, B., Ferry, A., Lainé, J., Romero, N.B., et al. (2010). A centronuclear myopathy-dynamin 2 mutation impairs skeletal muscle structure and function in mice. *Hum. Mol. Genet.* 19, 4820–4836.
- Duteil, S., Wary, C., Raynaud, J.S., Lebon, V., Lesage, D., Leroy-Willig, A., and Carlier, P.G. (2006). Influence of vascular filling and perfusion on BOLD contrast during reactive hyperemia in human skeletal muscle. *Magn. Reson. Med.* 55, 450–454.
- Emery, A.E. (2002). The muscular dystrophies. *The Lancet* 359, 687–695.
- Engel, W.K. (1967). Muscle biopsies in neuromuscular diseases. *Pediatr. Clin. North Am.* 14, 963.
- Engel, W.K., and Hawley, R.J. (1977). Focal lesions of muscle in peripheral vascular disease. *J. Neurol.* 215, 161–168.
- Ennen, J.P., Verma, M., and Asakura, A. (2013). Vascular-targeted therapies for Duchenne muscular dystrophy. *Skelet Muscle* 3, 9.
- Ervasti, J.M., and Campbell, K.P. (1991). Membrane organization of the dystrophin-glycoprotein complex. *Cell* 66, 1121–1131.
- Ervasti, J.M., and Campbell, K.P. (1993). A role for the dystrophin-glycoprotein complex as a transmembrane linker between laminin and actin. *J. Cell Biol.* 122, 809–823.
- Fan, Z., Wang, J., Ahn, M., Shiloh-Malawsky, Y., Chahin, N., Elmore, S., Bagnell Jr, C.R., Wilber, K., An, H., Lin, W., et al. (2014). Characteristics of magnetic resonance imaging biomarkers in a natural history study of golden retriever muscular dystrophy. *Neuromuscul. Disord.* 24, 178–191.
- Fidziańska, A., Glinka, Z., and Walski, M. (1986). An ultrastructural study of the vascular and muscular basement membrane in Duchenne-type dystrophy. *Clin. Neuropathol.* 6, 257–261.
- Finanger, E.L., Russman, B., Forbes, S.C., Rooney, W.D., Walter, G.A., and Vandenborne, K. (2012). Use of skeletal muscle MRI in diagnosis and monitoring disease progression in Duchenne muscular dystrophy. *Phys. Med. Rehabil. Clin. N. Am.* 23, 1–10.
- Fischmann, A., Hafner, P., Fasler, S., Gloor, M., Bieri, O., Studler, U., and Fischer, D. (2012). Quantitative MRI can detect subclinical disease progression in muscular dystrophy. *J. Neurol.* 259, 1648–1654.
- Fischmann, A., Hafner, P., Gloor, M., Schmid, M., Klein, A., Pohlman, U., Waltz, T., Gonzalez, R., Haas, T., Bieri, O., et al. (2013). Quantitative MRI and loss of free ambulation in Duchenne muscular dystrophy. *J. Neurol.* 260, 969–974.

- Fugier, C., Klein, A.F., Hammer, C., Vassilopoulos, S., Ivarsson, Y., Toussaint, A., Tosch, V., Vignaud, A., Ferry, A., Messaddeq, N., et al. (2011). Misregulated alternative splicing of BIN1 is associated with T tubule alterations and muscle weakness in myotonic dystrophy. *Nat. Med.* 17, 720–725.
- Fujii, J., Otsu, K., Zorzato, F., de Leon, S., Khanna, V.K., Weiler, J.E., O'Brien, P.J., and MacLennan, D.H. (1991). Identification of a mutation in porcine ryanodine receptor associated with malignant hyperthermia. *Science* 253, 448–451.
- Gaeta, M., Messina, S., Mileto, A., Vita, G.L., Ascenti, G., Vinci, S., Bottari, A., Vita, G., Settineri, N., Bruschetta, D., et al. (2012). Muscle fat-fraction and mapping in Duchenne muscular dystrophy: evaluation of disease distribution and correlation with clinical assessments. *Skeletal Radiol.* 41, 955–961.
- Gatehouse, P.D., and Bydder, G.M. (2003). Magnetic Resonance Imaging of Short T₂ Components in Tissue. *Clin. Radiol.* 58, 1–19.
- Gineste, C., Le Fur, Y., Vilmen, C., Le Troter, A., Pecchi, E., Cozzone, P.J., Hardeman, E.C., Bendahan, D., and Gondin, J. (2013a). Combined MRI and 31P-MRS investigations of the ACTA1 (H40Y) mouse model of nemaline myopathy show impaired muscle function and altered energy metabolism. *PloS One* 8, e61517.
- Gineste, C., Duhamel, G., Le Fur, Y., Vilmen, C., Cozzone, P.J., Nowak, K.J., Bendahan, D., and Gondin, J. (2013b). Multimodal MRI and 31P-MRS Investigations of the ACTA1 (Asp286Gly) Mouse Model of Nemaline Myopathy Provide Evidence of Impaired In Vivo Muscle Function, Altered Muscle Structure and Disturbed Energy Metabolism. *PloS One* 8, e72294.
- Gineste, C., De Winter, J.M., Kohl, C., Witt, C.C., Giannesini, B., Brohm, K., Le Fur, Y., Gretz, N., Vilmen, C., Pecchi, E., et al. (2013c). *In vivo* and *in vitro* investigations of heterozygous nebulin knock-out mice disclose a mild skeletal muscle phenotype. *Neuromuscul. Disord.* 23, 357–369.
- Goodpaster, B.H., Carlson, C.L., Visser, M., Kelley, D.E., Scherzinger, A., Harris, T.B., Stamm, E., and Newman, A.B. (2001). Attenuation of skeletal muscle and strength in the elderly: The Health ABC Study. *J. Appl. Physiol.* 90, 2157–2165.
- Grady, R.M., Teng, H., Nichol, M.C., Cunningham, J.C., Wilkinson, R.S., and Sanes, J.R. (1997). Skeletal and cardiac myopathies in mice lacking utrophin and dystrophin: a model for Duchenne muscular dystrophy. *Cell* 90, 729–738.
- Gray, S.K., McGee-Lawrence, M.E., Sanders, J.L., Condon, K.W., Tsai, C.-J., and Donahue, S.W. (2012). Black bear parathyroid hormone has greater anabolic effects on trabecular bone in dystrophin-deficient mice than in wild type mice. *Bone* 51, 578–585.
- Grewal, P.K., and Hewitt, J.E. (2002). Mutation of *Large*, which encodes a putative glycosyltransferase, in an animal model of muscular dystrophy. *Biochim. Biophys. Acta BBA-Gen. Subj.* 1573, 216–224.

- Grewal, P.K., Holzfeind, P.J., Bittner, R.E., and Hewitt, J.E. (2001). Mutant glycosyltransferase and altered glycosylation of α -dystroglycan in the myodystrophy mouse. *Nat. Genet.* 28, 151–154.
- Griffin, J.L., Williams, H.J., Sang, E., Clarke, K., Rae, C., and Nicholson, J.K. (2001). Metabolic Profiling of Genetic Disorders: A Multitissue ^1H Nuclear Magnetic Resonance Spectroscopic and Pattern Recognition Study into Dystrophic Tissue. *Anal. Biochem.* 293, 16–21.
- Grindrod, S., Tofts, P., and Edwards, R. (1983). Investigation of human skeletal muscle structure and composition by X-ray computerised tomography. *Eur. J. Clin. Invest.* 13, 465–468.
- Grounds, M.D., Radley, H.G., Lynch, G.S., Nagaraju, K., and De Luca, A. (2008). Towards developing standard operating procedures for pre-clinical testing in the mdx mouse model of Duchenne muscular dystrophy. *Neurobiol. Dis.* 31, 1–19.
- Gudrun, B., Andrew, G.E., Boysen, G., and Engel, A.G. (1975). Effects of microembolization on the skeletal muscle blood flow. A critique of the microvascular occlusion model of Duchenne dystrophy. *Acta Neurol. Scand.* 52, 71–80.
- Gumerson, J.D., and Michele, D.E. (2011). The dystrophin-glycoprotein complex in the prevention of muscle damage. *BioMed Res. Int.* 2011, 210797.
- Gurniak, C.B., Chevessier, F., Jokwitz, M., Jönsson, F., Perlas, E., Richter, H., Matern, G., Boyle, P.P., Chaponnier, C., Fürst, D., et al. (2014). Severe protein aggregate myopathy in a knockout mouse model points to an essential role of cofilin2 in sarcomeric actin exchange and muscle maintenance. *Eur. J. Cell Biol.* 93, 252–266.
- Hack, A.A., Ly, C.T., Jiang, F., Clendenin, C.J., Sigrist, K.S., Wollmann, R.L., and McNally, E.M. (1998). γ -Sarcoglycan deficiency leads to muscle membrane defects and apoptosis independent of dystrophin. *J. Cell Biol.* 142, 1279–1287.
- Hathaway, P.W., Engel, W.K., and Zellweger, H. (1970). Experimental myopathy after microarterial embolization: comparison with childhood X-linked pseudohypertrophic muscular dystrophy. *Arch. Neurol.* 22, 365–378.
- Heerschap, A., Bergman, A.H., Van Vaals, J.J., Wirtz, P., Loermans, H.M., and Veerkamp, J.H. (1988). Alterations in relative phosphocreatine concentrations in preclinical mouse muscular dystrophy revealed by in vivo NMR. *NMR Biomed.* 1, 27–31.
- Heier, C.R., Guerron, A.D., Korotcov, A., Lin, S., Gordish-Dressman, H., Fricke, S., Sze, R.W., Hoffman, E.P., Wang, P., and Nagaraju, K. (2014). Non-Invasive MRI and Spectroscopy of mdx Mice Reveal Temporal Changes in Dystrophic Muscle Imaging and in Energy Deficits. *PloS One* 9, e112477.
- Hepple, R.T. (1997). A new measurement of tissue capillarity: the capillary-to-fibre perimeter exchange index. *Can. J. Appl. Physiol.* 22, 11–22.

- Hoffman, E.P., Brown Jr, R.H., and Kunkel, L.M. (1987). Dystrophin: the protein product of the Duchenne muscular dystrophy locus. *Cell* 51, 919–928.
- Hsieh, T.-J., Jaw, T.-S., Chuang, H.-Y., Jong, Y.-J., Liu, G.-C., and Li, C.-W. (2009). Muscle metabolism in Duchenne muscular dystrophy assessed by in vivo proton magnetic resonance spectroscopy. *J. Comput. Assist. Tomogr.* 33, 150–154.
- Huang, Y., Majumdar, S., Genant, H.K., Chan, W.P., Sharma, K.R., Yu, P., Mynhier, M., and Miller, R.G. (1994). Quantitative MR relaxometry study of muscle composition and function in Duchenne muscular dystrophy. *J. Magn. Reson. Imaging* 4, 59–64.
- Ichioka, S., Shibata, M., Kosaki, K., Sato, Y., Harii, K., and Kamiya MD, A. (1997). Effects of shear stress on wound-healing angiogenesis in the rabbit ear chamber. *J. Surg. Res.* 72, 29–35.
- Ishigaki, K., Yoshikawa, Y., Kuwatsuru, R., Oda, E., Murakami, T., Sato, T., Saito, T., Umez, R., and Osawa, M. (2012). High-density CT of muscle and liver may allow early diagnosis of childhood-onset Pompe disease. *Brain Dev.* 34, 103–106.
- Jeffery, N.S., Stephenson, R.S., Gallagher, J.A., Jarvis, J.C., and Cox, P.G. (2011). Micro-computed tomography with iodine staining resolves the arrangement of muscle fibres. *J. Biomech.* 44, 189–192.
- Jiddane, M., Gastaut, J.L., Pellissier, J.F., Pouget, J., Serratrice, G., and Salamon, G. (1983). CT of primary muscle diseases. *Am. J. Neuroradiol.* 4, 773–776.
- Jungbluth, H., Wallgren-Pettersson, C., and Laporte, J. (2008). Centronuclear (myotubular) myopathy. *Orphanet J Rare Dis* 3, 26.
- Kabaeva, Z., Meekhof, K.E., and Michele, D.E. (2011). Sarcolemma instability during mechanical activity in Largemyd cardiac myocytes with loss of dystroglycan extracellular matrix receptor function. *Hum. Mol. Genet.* 20, 3346–3355.
- Kemp, G.J., Taylor, D.J., Dunn, J.F., Frostick, S.P., and Radda, G.K. (1993). Cellular energetics of dystrophic muscle. *J. Neurol. Sci.* 116, 201–206.
- Kim, H.K., Laor, T., Horn, P.S., Racadio, J.M., Wong, B., and Dardzinski, B.J. (2010). T2 Mapping in Duchenne Muscular Dystrophy: Distribution of Disease Activity and Correlation with Clinical Assessments 1. *Radiology* 255, 899–908.
- Kinali, M., Arechavala-Gomez, V., Cirak, S., Glover, A., Guglieri, M., Feng, L., Hollingsworth, K.G., Hunt, D., Jungbluth, H., Roper, H.P., et al. (2011). Muscle histology vs MRI in Duchenne muscular dystrophy. *Neurology* 76, 346–353.
- Kobzik, L., Reid, M.B., Bredt, D.S., and Stamler, J.S. (1994). Nitric oxide in skeletal muscle. *Nature* 372, 546–548.
- Koehler, J. (1977). Blood vessel structure in Duchenne muscular dystrophy. I. Light and electron microscopic observations in resting muscle. *Neurology* 27, 861–861.

- Kuang, W., Xu, H., Vachon, P.H., Liu, L., Loechel, F., Wewer, U.M., and Engvall, E. (1998). Merosin-deficient congenital muscular dystrophy. Partial genetic correction in two mouse models. *J. Clin. Invest.* 102, 844–852.
- Lamminen, A.E. (1990). Magnetic resonance imaging of primary skeletal muscle diseases: patterns of distribution and severity of involvement. *Br. J. Radiol.* 63, 946–950.
- Landisch, R.M., Kosir, A.M., Nelson, S.A., Baltgalvis, K.A., and Lowe, D.A. (2008). Adaptive and nonadaptive responses to voluntary wheel running by mdx mice. *Muscle Nerve* 38, 1290–1293.
- Lane, P.W., Beamer, T.C., and Myers, D.D. (1975). Myodystrophy, a new myopathy on chromosome 8 of the mouse. *J. Hered.* 67, 135–138.
- Lawlor, M.W., Alexander, M.S., Viola, M.G., Meng, H., Joubert, R., Gupta, V., Motohashi, N., Manfredy, R.A., Hsu, C.P., Huang, P., et al. (2012). Myotubularin-deficient myoblasts display increased apoptosis, delayed proliferation, and poor cell engraftment. *Am. J. Pathol.* 181, 961–968.
- Lederlin, M., Ozier, A., Dournes, G., Ousova, O., Girodet, P.-O., Begueret, H., Marthan, R., Montaudon, M., Laurent, F., and Berger, P. (2012). In vivo micro-CT assessment of airway remodeling in a flexible OVA-sensitized murine model of asthma. *PloS One* 7, e48493.
- Lee, K.H., Baek, M.Y., Moon, K.Y., Song, W.K., Chung, C.H., Ha, D.B., and Kang, M.-S. (1994). Nitric oxide as a messenger molecule for myoblast fusion. *J. Biol. Chem.* 269, 14371–14374.
- Leinonen, H., Juntunen, J., Somer, H., and Rapola, J. (1979). Capillary circulation and morphology in Duchenne muscular dystrophy. *Eur. Neurol.* 18, 249–255.
- Leroy-Willig, A., Willig, T.N., Henry-Feugeas, M.C., Frouin, V., Marinier, E., Boulrier, A., Barzic, F., Schouman-Claeys, E., and Syrota, A. (1997). Body composition determined with MR in patients with Duchenne muscular dystrophy, spinal muscular atrophy, and normal subjects. *Magn. Reson. Imaging* 15, 737–744.
- Liu, G.C., Jong, Y.J., Chiang, C.H., and Jaw, T.-S. (1993). Duchenne muscular dystrophy: MR grading system with functional correlation. *Radiology* 186, 475–480.
- Lodi, R., Muntoni, F., Taylor, J., Kumar, S., Sewry, C.A., Blamire, A., Styles, P., and Taylor, D.J. (1997). Correlative MR imaging and ³¹P-MR spectroscopy study in sarcoglycan deficient limb girdle muscular dystrophy. *Neuromuscul. Disord.* 7, 505–511.
- Lodi, R., Kemp, G.J., Muntoni, F., Thompson, C.H., Rae, C., Taylor, J., Styles, P., and Taylor, D.J. (1999). Reduced cytosolic acidification during exercise suggests defective glycolytic activity in skeletal muscle of patients with Becker muscular

dystrophy An in vivo ³¹P magnetic resonance spectroscopy study. *Brain* 122, 121–130.

Lopez, M.A., Pardo, P.S., Cox, G.A., and Boriek, A.M. (2008). Early mechanical dysfunction of the diaphragm in the muscular dystrophy with myositis (Ttnmdm) model. *Am. J. Physiol.-Cell Physiol.* 295, C1092–C1102.

Loufrani, L., Matrougui, K., Gorny, D., Duriez, M., Blanc, I., Lévy, B.I., and Henrion, D. (2001). Flow (shear stress)–induced endothelium-dependent dilation is altered in mice lacking the gene encoding for dystrophin. *Circulation* 103, 864–870.

Loufrani, L., Dubroca, C., You, D., Li, Z., Levy, B., Paulin, D., and Henrion, D. (2004). Absence of dystrophin in mice reduces NO-dependent vascular function and vascular density: total recovery after a treatment with the aminoglycoside gentamicin. *Arterioscler. Thromb. Vasc. Biol.* 24, 671–676.

Love, D.R., Byth, B.C., Tinsley, J.M., Blake, D.J., and Davies, K.E. (1993). Dystrophin and dystrophin-related proteins: a review of protein and RNA studies. *Neuromuscul. Disord.* 3, 5–21.

Mahmoud-Ghoneim, D., Cherel, Y., Lemaire, L., de Certaines, J.D., and Maniere, A. (2006). Texture analysis of magnetic resonance images of rat muscles during atrophy and regeneration. *Magn. Reson. Imaging* 24, 167–171.

Manske, S.L., Boyd, S.K., and Zernicke, R.F. (2010). Muscle and bone follow similar temporal patterns of recovery from muscle-induced disuse due to botulinum toxin injection. *Bone* 46, 24–31.

Manske, S.L., Good, C.A., Zernicke, R.F., and Boyd, S.K. (2012). High-frequency, low-magnitude vibration does not prevent bone loss resulting from muscle disuse in mice following botulinum toxin injection. *PloS One* 7, e36486.

Marden, F.A., Connolly, A.M., Siegel, M.J., and Rubin, D.A. (2005). Compositional analysis of muscle in boys with Duchenne muscular dystrophy using MR imaging. *Skeletal Radiol.* 34, 140–148.

Martins, P.C., Ayub-Guerrieri, D., Martins-Bach, A.B., Onofre-Oliveira, P., Malheiros, J.M., Tannus, A., de Sousa, P.L., Carlier, P.G., and Vainzof, M. (2013). Dmdmdx/Largemyd: a new mouse model of neuromuscular diseases useful for studying physiopathological mechanisms and testing therapies. *Dis. Model. Mech.* 6, 1167–1174.

Mathur, S., Vohra, R.S., Germain, S.A., Forbes, S., Bryant, N.D., Vandenborne, K., and Walter, G.A. (2011). Changes in muscle T2 and tissue damage after downhill running in mdx mice. *Muscle Nerve* 43, 878–886.

Matsakas, A., Yadav, V., Lorca, S., and Narkar, V. (2013). Muscle ERRγ mitigates Duchenne muscular dystrophy via metabolic and angiogenic reprogramming. *FASEB J.* 27, 4004–4016.

- Mavrogeni, S., Papavasiliou, A., Douskou, M., Kolovou, G., Papadopoulou, E., and Cokkinos, D.V. (2009). Effect of deflazacort on cardiac and sternocleidomastoid muscles in Duchenne muscular dystrophy: a magnetic resonance imaging study. *Eur. J. Paediatr. Neurol.* 13, 34–40.
- McIntosh, L., Granberg, K.-E., Brière, K.M., and Anderson, J.E. (1998a). Nuclear magnetic resonance spectroscopy study of muscle growth, mdx dystrophy and glucocorticoid treatments: correlation with repair. *NMR Biomed.* 11, 1–10.
- McIntosh, L.M., Baker, R.E., and Anderson, J.E. (1998b). Magnetic resonance imaging of regenerating and dystrophic mouse muscle. *Biochem. Cell Biol.* 76, 532–541.
- Mendell, J.R., Engel, W.K., and Derrer, E.C. (1971). Duchenne muscular dystrophy: functional ischemia reproduces its characteristic lesions. *Science* 172, 1143–1145.
- Mercuri, E., and Muntoni, F. (2012). The ever-expanding spectrum of congenital muscular dystrophies. *Ann. Neurol.* 72, 9–17.
- Mercuri, E., Pichiecchio, A., Allsop, J., Messina, S., Pane, M., and Muntoni, F. (2007). Muscle MRI in inherited neuromuscular disorders: past, present, and future. *J. Magn. Reson. Imaging* 25, 433–440.
- Messina, S., Mazzeo, A., Bitto, A., Aguenouz, M., Migliorato, A., De Pasquale, M.G., Minutoli, L., Altavilla, D., Zentilin, L., Giacca, M., et al. (2007). VEGF overexpression via adeno-associated virus gene transfer promotes skeletal muscle regeneration and enhances muscle function in mdx mice. *FASEB J.* 21, 3737–3746.
- Metscher, B.D. (2009). MicroCT for comparative morphology: simple staining methods allow high-contrast 3D imaging of diverse non-mineralized animal tissues. *BMC Physiol.* 9, 11.
- Miike, T. (1983). Maturational defect of regenerating muscle fibers in cases with Duchenne and congenital muscular dystrophies. *Muscle Nerve* 6, 545–552.
- Miike, T., Sugino, S., Ohtani, Y., Taku, K., and Yoshioka, K. (1987). Vascular endothelial cell injury and platelet embolism in Duchenne muscular dystrophy at the preclinical stage. *J. Neurol. Sci.* 82, 67–80.
- Mirabella, M., Servidei, S., Manfredi, G., Ricci, E., Frustaci, A., Bertini, E., Rana, M., and Tonali, P. (1993). Cardiomyopathy may be the only clinical manifestation in female carriers of Duchenne muscular dystrophy. *Neurology* 43, 2342–2342.
- Mitsuhashi, S., and Kang, P.B. (2012). Update on the genetics of limb girdle muscular dystrophy. *Semin. Pediatr. Neurol.* 19, 211–218.
- Miyagoe, Y., Hanaoka, K., Nonaka, I., Hayasaka, M., Nabeshima, Y., Arahata, K., Nabeshima, Y., and Takeda, S. (1997). Laminin $\alpha 2$ chain-null mutant mice by

targeted disruption of the *Lama2* gene: a new model of merosin (laminin 2)-deficient congenital muscular dystrophy. *FEBS Lett.* 415, 33–39.

Miyatake, M., Miike, T., Zhao, J., Yoshioka, K., Uchino, M., and Usuku, G. (1989). Possible systemic smooth muscle layer dysfunction due to a deficiency of dystrophin in Duchenne muscular dystrophy. *J. Neurol. Sci.* 93, 11–17.

Moore, C.J., and Winder, S.J. (2012). The inside and out of dystroglycan post-translational modification. *Neuromuscul. Disord.* 22, 959–965.

Muller, J., Vayssiere, N., Royuela, M., Leger, M.E., Muller, A., Bacou, F., Pons, F., Hugon, G., and Mornet, D. (2001). Comparative evolution of muscular dystrophy in diaphragm, gastrocnemius and masseter muscles from old male mdx mice. *J. Muscle Res. Cell Motil.* 22, 133–139.

Muntoni, F., Mateddu, A., Marchei, F., Clerk, A., and Serra, G. (1993). Muscular weakness in the *mdx* mouse. *J. Neurol. Sci.* 120, 71–77.

Muntoni, F., Torelli, S., and Brockington, M. (2008). Muscular dystrophies due to glycosylation defects. *Neurotherapeutics* 5, 627–632.

Nakayama, T., Kuru, S., Okura, M., Motoyoshi, Y., and Kawai, M. (2013a). Estimation of net muscle volume in patients with muscular dystrophy using muscle CT for prospective muscle volume analysis: an observational study. *BMJ Open* 3, e003603.

Nakayama, T., Kuru, S., and Kawai, M. (2013b). Analysis using histograms of muscle CT images in patients with Duchenne muscular dystrophy. *BMJ Case Rep.* 2013, bcr2013009301.

Nance, J.R., Dowling, J.J., Gibbs, E.M., and Bönnemann, C.G. (2012). Congenital myopathies: an update. *Curr. Neurol. Neurosci. Rep.* 12, 165–174.

Newman, R.J., Bore, P.J., Chan, L., Gadian, D.G., Styles, P., Taylor, D., and Radda, G.K. (1982). Nuclear magnetic resonance studies of forearm muscle in Duchenne dystrophy. *Br. Med. J. (Clin. Res. Ed.)* 284, 1072–1074.

Nguyen, F., Guigand, L., Goubault-Leroux, I., Wyers, M., and Cherel, Y. (2005). Microvessel density in muscles of dogs with golden retriever muscular dystrophy. *Neuromuscul. Disord.* 15, 154–163.

Nigro, G., Comi, L.I., Politano, L., and Bain, R.J.I. (1990). The incidence and evolution of cardiomyopathy in Duchenne muscular dystrophy. *Int. J. Cardiol.* 26, 271–277.

Nketiah, G., Savio, S., Dastidar, P., Nikander, R., Eskola, H., and Sievänen, H. (2014). Detection of exercise load-associated differences in hip muscles by texture analysis. *Scand. J. Med. Sci. Sports.* Epub ahead of print.

- Novotny, S.A., Warren, G.L., Lin, A.S., Guldberg, R.E., Baltgalvis, K.A., and Lowe, D.A. (2011). Bone is functionally impaired in dystrophic mice but less so than skeletal muscle. *Neuromuscul. Disord.* *21*, 183–193.
- Novotny, S.A., Warren, G.L., Lin, A.S., Guldberg, R.E., Baltgalvis, K.A., and Lowe, D.A. (2012). Prednisolone treatment and restricted physical activity further compromise bone of mdx mice. *J. Musculoskelet. Neuronal Interact.* *12*, 16–23.
- Novotny, S.A., Mader, T.L., Greising, A.G., Lin, A.S., Guldberg, R.E., Warren, G.L., and Lowe, D.A. (2014). Low intensity, high frequency vibration training to improve musculoskeletal function in a mouse model of duchenne muscular dystrophy. *PloS One* *9*, e104339.
- Odintsov, B., Chun, J.L., and Berry, S.E. (2013). Whole body MRI and fluorescent microscopy for detection of stem cells labeled with superparamagnetic iron oxide (SPIO) nanoparticles and DiI following intramuscular and systemic delivery. In *Imaging and Tracking Stem Cells*, (Springer), pp. 177–193.
- Ohlendieck, K., and Campbell, K.P. (1991). Dystrophin-associated proteins are greatly reduced in skeletal muscle from mdx mice. *J. Cell Biol.* *115*, 1685–1694.
- Ottenheijm, C.A., Buck, D., de Winter, J.M., Ferrara, C., Piroddi, N., Tesi, C., Jasper, J.R., Malik, F.I., Meng, H., Stienen, G.J., et al. (2013). Deleting exon 55 from the nebulin gene induces severe muscle weakness in a mouse model for nemaline myopathy. *Brain* *136*, 1718–1731.
- Pacak, C.A., Walter, G.A., Gaidosh, G., Bryant, N., Lewis, M.A., Germain, S., Mah, C.S., Campbell, K.P., and Byrne, B.J. (2007). Long-term skeletal muscle protection after gene transfer in a mouse model of LGMD-2D. *Mol. Ther.* *15*, 1775–1781.
- De Paepe, B., and De Bleecker, J.L. (2013). Cytokines and chemokines as regulators of skeletal muscle inflammation: presenting the case of Duchenne muscular dystrophy. *Mediators Inflamm.* *2013*, 540370.
- Paik, S.-H., Kim, W.-K., Park, J.-S., Park, C.-S., and Jin, G.-Y. (2014). A Quantitative Study of Airway Changes on Micro-CT in a Mouse Asthma Model: Comparison With Histopathological Findings. *Allergy Asthma Immunol. Res.* *6*, 75–82.
- Palladino, M., Gatto, I., Neri, V., Straino, S., Smith, R.C., Silver, M., Gaetani, E., Marcantoni, M., Giarretta, I., Stigliano, E., et al. (2013). Angiogenic Impairment of the Vascular Endothelium A Novel Mechanism and Potential Therapeutic Target in Muscular Dystrophy. *Arterioscler. Thromb. Vasc. Biol.* *33*, 2867–2876.
- Papoti, D. (2006). Transdutores de RF para experimentos de imagens de pequenos animais. Universidade de São Paulo.
- Paradas, C., Llauger, J., Diaz-Manera, J., Rojas-Garcia, R., De Luna, N., Iturriaga, C., Márquez, C., Usón, M., Hankiewicz, K., Gallardo, E., et al. (2010). Redefining

dysferlinopathy phenotypes based on clinical findings and muscle imaging studies. *Neurology* 75, 316–323.

Pastoret, C., and Sebillé, A. (1995). *mdx* mice show progressive weakness and muscle deterioration with age. *J. Neurol. Sci.* 129, 97–105.

Pelé, M., Tiret, L., Kessler, J.-L., Blot, S., and Panthier, J.-J. (2005). SINE exonic insertion in the PTPLA gene leads to multiple splicing defects and segregates with the autosomal recessive centronuclear myopathy in dogs. *Hum. Mol. Genet.* 14, 1417–1427.

Percival, J.M., Siegel, M.P., Knowels, G., and Marcinek, D.J. (2013). Defects in mitochondrial localization and ATP synthesis in the mdx mouse model of Duchenne muscular dystrophy are not alleviated by PDE5 inhibition. *Hum. Mol. Genet.* 22, 153–167.

Pichiecchio, A., Uggetti, C., Egitto, M., Berardinelli, A., Orcesi, S., Gorni, K., Zanardi, C., and Tagliabue, A. (2002). Quantitative MR evaluation of body composition in patients with Duchenne muscular dystrophy. *Eur. Radiol.* 12, 2704–2709.

Pierson, C.R., Dulin-Smith, A.N., Durban, A.N., Marshall, M.L., Marshall, J.T., Snyder, A.D., Naiyer, N., Gladman, J.T., Chandler, D.S., Lawlor, M.W., et al. (2012). Modeling the human MTM1 p. R69C mutation in murine Mtm1 results in exon 4 skipping and a less severe myotubular myopathy phenotype. *Hum. Mol. Genet.* 21, 811–825.

Poliachik, S.L., Friedman, S.D., Carter, G.T., Parnell, S.E., and Shaw, D.W. (2012). Skeletal muscle edema in muscular dystrophy: clinical and diagnostic implications. *Phys. Med. Rehabil. Clin. N. Am.* 23, 107–122.

Pratt, S.J., Xu, S., Mullins, R.J., and Lovering, R.M. (2013). Temporal changes in magnetic resonance imaging in the mdx mouse. *BMC Res. Notes* 6, 262.

Quijano-Roy, S., Carlier, R.Y., and Fischer, D. (2011). Muscle imaging in congenital myopathies. *Semin. Pediatr. Neurol.* 18, 221–229.

Quijano-Roy, S., Avila-Smirnow, D., and Carlier, R.Y. (2012). Whole body muscle MRI protocol: pattern recognition in early onset NM disorders. *Neuromuscul. Disord.* 22, S68–S84.

Rae, C., Scott, R.B., Thompson, C.H., Dixon, R.M., Dumughn, I., J Kemp, G., Male, A., Pike, M., Styles, P., and Radda, G.K. (1998). Brain biochemistry in Duchenne muscular dystrophy: A ¹H magnetic resonance and neuropsychological study. *J. Neurol. Sci.* 160, 148–157.

Rando, T.A. (2001a). The dystrophin–glycoprotein complex, cellular signaling, and the regulation of cell survival in the muscular dystrophies. *Muscle Nerve* 24, 1575–1594.

- Rando, T.A. (2001b). Role of nitric oxide in the pathogenesis of muscular dystrophies: a “two hit” hypothesis of the cause of muscle necrosis. *Microsc. Res. Tech.* 55, 223–235.
- Ravenscroft, G., Jackaman, C., Bringans, S., Papadimitriou, J.M., Griffiths, L.M., McNamara, E., Bakker, A.J., Davies, K.E., Laing, N.G., and Nowak, K.J. (2011). Mouse models of dominant ACTA1 disease recapitulate human disease and provide insight into therapies. *Brain* 134, 1101–1115.
- Raynaud, J.S., Duteil, S., Vaughan, J.T., Hennel, F., Wary, C., Leroy-Willig, A., and Carlier, P.G. (2001). Determination of skeletal muscle perfusion using arterial spin labeling NMRI: validation by comparison with venous occlusion plethysmography. *Magn. Reson. Med.* 46, 305–311.
- Razek, A.A., Kandell, A.Y., Elsorogy, L.G., Elmongy, A., and Basett, A.A. (2009). Disorders of cortical formation: MR imaging features. *Am. J. Neuroradiol.* 30, 4–11.
- Rederstorff, M., Castets, P., Arbogast, S., Lainé, J., Vassilopoulos, S., Beuvin, M., Dubourg, O., Vignaud, A., Ferry, A., Krol, A., et al. (2011). Increased muscle stress-sensitivity induced by selenoprotein N inactivation in mouse: a mammalian model for SEPNI-related myopathy. *PloS One* 6, e23094.
- Rickards, D., Isherwood, I., Hutchinson, R., Gibbs, A., and Cumming, W.J.K. (1982). Computed tomography in dystrophia myotonica. *Neuroradiology* 24, 27–31.
- Rittweger, J., Möller, K., Bareille, M.-P., Felsenberg, D., and Zange, J. (2013). Muscle X-ray attenuation is not decreased during experimental bed rest. *Muscle Nerve* 47, 722–730.
- Roberts, C.K., Barnard, R.J., Scheck, S.H., and Balon, T.W. (1997). Exercise-stimulated glucose transport in skeletal muscle is nitric oxide dependent. *Am. J. Physiol.-Endocrinol. Metab.* 36, E220–E225.
- Roberts, M.C., Mickelson, J.R., Patterson, E.E., Nelson, T.E., Armstrong, P.J., Brunson, D.B., and Hogan, K. (2001). Autosomal dominant canine malignant hyperthermia is caused by a mutation in the gene encoding the skeletal muscle calcium release channel (RYR1). *Anesthesiology* 95, 716–725.
- Romero, N.B., and Clarke, N.F. (2012). Congenital myopathies. *Handb. Clin. Neurol.* 113, 1321–1336.
- Rudroff, T., Weissman, J.A., Bucci, M., Seppänen, M., Kaskinoro, K., Heinonen, I., and Kalliokoski, K.K. (2014). Positron emission tomography detects greater blood flow and less blood flow heterogeneity in the exercising skeletal muscles of old compared with young men during fatiguing contractions. *J. Physiol.* 592, 337–349.
- Saab, G., Thompson, R.T., and Marsh, G.D. (1999). Multicomponent T2 relaxation of in vivo skeletal muscle. *Magn. Reson. Med.* 42, 150–157.

- Sacco, A., Mourkioti, F., Tran, R., Choi, J., Llewellyn, M., Kraft, P., Shkreli, M., Delp, S., Pomerantz, J.H., Artandi, S.E., et al. (2010). Short telomeres and stem cell exhaustion model Duchenne muscular dystrophy in mdx/mTR mice. *Cell* 143, 1059–1071.
- Salimena, M.C., Lagrota-Candido, J., and Quírico-Santos, T. (2000). Gender dimorphism influences extracellular matrix expression and regeneration of muscular tissue in mdx dystrophic mice. *Histochem. Cell Biol.* 122, 435–444.
- Sander, M., Chavoshan, B., Harris, S.A., Iannaccone, S.T., Stull, J.T., Thomas, G.D., and Victor, R.G. (2000). Functional muscle ischemia in neuronal nitric oxide synthase-deficient skeletal muscle of children with Duchenne muscular dystrophy. *Proc. Natl. Acad. Sci.* 97, 13818–13823.
- Schatzberg, S.J., Olby, N.J., Breen, M., Anderson, L.V., Langford, C.F., Dickens, H.F., Wilton, S.D., Zeiss, C.J., Binns, M.M., Kornegay, J.N., et al. (1999). Molecular analysis of a spontaneous dystrophinknockout dog. *Neuromuscul. Disord.* 9, 289–295.
- Schessler, J., Medne, L., Hu, Y., Zou, Y., Brown, M.J., Huse, J.T., Torigian, D.A., Jungbluth, H., Goebel, H.-H., and Bönnemann, C.G. (2007). MRI in *DNM2*-related centronuclear myopathy: Evidence for highly selective muscle involvement. *Neuromuscul. Disord.* 17, 28–32.
- Schmidt, S., Vieweger, A., Obst, M., Mueller, S., Gross, V., Gutberlet, M., Steinbrink, J., Taubert, S., Misselwitz, B., Luedemann, L., et al. (2009). Dysferlin-deficient Muscular Dystrophy: Gadofluorine M Suitability at MR Imaging in a Mouse Model 1. *Radiology* 250, 87–94.
- Schwartz, M.S., Swash, M., Ingram, D.A., Davis, G.R., Thompson, A.J., Thakkar, C., and Hart, G. (1988). Patterns of selective involvement of thigh muscles in neuromuscular disease. *Muscle Nerve* 11, 1240–1245.
- Schwenzer, N.F., Martirosian, P., Machann, J., Schraml, C., Steidle, G., Claussen, C.D., and Schick, F. (2009). Aging effects on human calf muscle properties assessed by MRI at 3 Tesla. *J. Magn. Reson. Imaging* 29, 1346–1354.
- Sewry, C.A., Jimenez-Mallebrera, C., and Muntoni, F. (2008). Congenital myopathies. *Curr. Opin. Neurol.* 21, 569–575.
- Shelton, G.D., and Engvall, E. (2005). Canine and feline models of human inherited muscle diseases. *Neuromuscul. Disord.* 15, 127–138.
- Shichiji, M., Biancalana, V., Fardeau, M., Hogrel, J.-Y., Osawa, M., Laporte, J., and Romero, N.B. (2013). Extensive morphological and immunohistochemical characterization in myotubular myopathy. *Brain Behav.* 3, 476–486.
- Shieh, P.B. (2013). Muscular dystrophies and other genetic myopathies. *Neurol. Clin.* 31, 1009–1029.

Shimatsu, Y., Katagiri, K., Furuta, T., Nakura, M., Tanioka, Y., Yuasa, K., Tomohiro, M., Kornegay, J.N., Nonaka, I., and Takeda, S. (2003). Canine X-linked muscular dystrophy in Japan (CXMDJ). *Exp. Anim.* 52, 93–97.

Shimizu-Motohashi, Y., and Asakura, A. (2014). Angiogenesis as a novel therapeutic strategy for Duchenne muscular dystrophy through decreased ischemia and increased satellite cells. *Front. Physiol.* 5, 50.

Sicinski, P., Geng, Y., Ryder-Cook, A.L., Barnard, E.A., Darlison, M.G., and Barnard, P.J. (1989). The molecular basis of muscular dystrophy in the mdx mouse: a point mutation. *Science* 244, 1578–1580.

Škoch, A., Jiráček, D., Vyhnanovská, P., Dezortová, M., Fendrych, P., Rolencová, E., and Hájek, M. (2004). Classification of calf muscle MR images by texture analysis. *Magn. Reson. Mater. Phys. Biol. Med.* 16, 259–267.

Stedman, H.H., Sweeney, H.L., Shrager, J.B., Maguire, H.C., Panettieri, R.A., Petrof, B., Narusawa, M., Leferovich, J.M., Sladky, J.T., and Kelly, A.M. (1991). The mdx mouse diaphragm reproduces the degenerative changes of Duchenne muscular dystrophy. *Nature* 352, 536–539.

Stern, L.M., Caudrey, D.J., Perrett, L.V., and Boldt, D.W. (1984). Progression of muscular dystrophy assessed by computed tomography. *Dev. Med. Child Neurol.* 26, 569–573.

Straino, S., Germani, A., Di Carlo, A., Porcelli, D., De Mori, R., Mangoni, A., Napolitano, M., Martelli, F., Biglioli, P., and Capogrossi, M.C. (2004). Enhanced arteriogenesis and wound repair in dystrophin-deficient mdx mice. *Circulation* 110, 3341–3348.

Straub, V., and Campbell, K.P. (1997). Muscular dystrophies and the dystrophin-glycoprotein complex. *Curr. Opin. Neurol.* 10, 168–175.

Straub, V., Rafael, J.A., Chamberlain, J.S., and Campbell, K.P. (1997). Animal models for muscular dystrophy show different patterns of sarcolemmal disruption. *J. Cell Biol.* 139, 375–385.

Straub, V., Duclos, F., Venzke, D.P., Lee, J.C., Cutshall, S., Leveille, C.J., and Campbell, K.P. (1998). Molecular pathogenesis of muscle degeneration in the δ -sarcoglycan-deficient hamster. *Am. J. Pathol.* 153, 1623–1630.

Straub, V., Donahue, K.M., Allamand, V., Davisson, R.L., Kim, Y.R., and Campbell, K.P. (2000). Contrast agent-enhanced magnetic resonance imaging of skeletal muscle damage in animal models of muscular dystrophy. *Magn. Reson. Med.* 44, 655–659.

Strzelecki, M., Szczypinski, P., Materka, A., and Klepaczko, A. (2013). A software tool for automatic classification and segmentation of 2D/3D medical images. *Nucl. Instrum. Methods Phys. Res. Sect. Accel. Spectrometers Detect. Assoc. Equip.* 702, 137–140.

- Susman, R.D., Quijano-Roy, S., Yang, N., Webster, R., Clarke, N.F., Dowling, J., Kennerson, M., Nicholson, G., Biancalana, V., Ilkovski, B., et al. (2010). Expanding the clinical, pathological and MRI phenotype of *DNM2*-related centronuclear myopathy. *Neuromuscul. Disord.* 20, 229–237.
- Swash, M., Brown, M.M., and Thakkar, C. (1995). CT muscle imaging and the clinical assessment of neuromuscular disease. *Muscle Nerve* 18, 708–714.
- Szczypinski, P.M., Strzelecki, M., and Materka, A. (2007). Mazda-a software for texture analysis. In 2007 International Symposium of Information Technology Convergence, (IEEE), pp. 245–249.
- Szczypiński, P.M., Strzelecki, M., Materka, A., and Klepaczko, A. (2009). MaZda—A software package for image texture analysis. *Comput. Methods Programs Biomed.* 94, 66–76.
- Tanabe, Y., Esaki, K., and Nomura, T. (1986). Skeletal muscle pathology in X chromosome-linked muscular dystrophy (mdx) mouse. *Acta Neuropathol. (Berl.)* 69, 91–95.
- Tardif-de Géry, S., Vilquin, J.-T., Carlier, P., Raynaud, J.-S., Wary, C., Schwartz, K., and Leroy-Willig, A. (2000). Muscular transverse relaxation time measurement by magnetic resonance imaging at 4 Tesla in normal and dystrophic *dy* and *dy2j* mice. *Neuromuscul. Disord.* 10, 507–513.
- Tasca, G., Monforte, M., Iannaccone, E., Laschena, F., Ottaviani, P., Silvestri, G., Masciullo, M., Mirabella, M., Servidei, S., and Ricci, E. (2012a). Muscle MRI in female carriers of dystrophinopathy. *Eur. J. Neurol.* 19, 1256–1260.
- Tasca, G., Iannaccone, E., Monforte, M., Masciullo, M., Bianco, F., Laschena, F., Ottaviani, P., Pelliccioni, M., Pane, M., Mercuri, E., et al. (2012b). Muscle MRI in Becker muscular dystrophy. *Neuromuscul. Disord.* 22, S100–S106.
- Taylor, D.J., Bore, P.J., Styles, P., Gadian, D.G., and Radda, G.K. (1983). Bioenergetics of intact human muscle. A ³¹P nuclear magnetic resonance study. *Mol. Biol. Med.* 1, 77–94.
- Termote, J.-L., Baert, A., Crolla, D., Palmers, Y., and Bulcke, J.A. (1980). Computed tomography of the normal and pathologic muscular system. *Radiology* 137, 439–444.
- Thibaud, J.-L., Monnet, A., Bertoldi, D., Barthelemy, I., Blot, S., and Carlier, P.G. (2007). Characterization of dystrophic muscle in golden retriever muscular dystrophy dogs by nuclear magnetic resonance imaging. *Neuromuscul. Disord.* 17, 575–584.
- Thibaud, J.-L., Azzabou, N., Barthelemy, I., Fleury, S., Cabrol, L., Blot, S., and Carlier, P.G. (2012). Comprehensive longitudinal characterization of canine muscular dystrophy by serial NMR imaging of GRMD dogs. *Neuromuscul. Disord.* 22, S85–S99.

Thomas, G.D. (2013). Functional muscle ischemia in Duchenne and Becker muscular dystrophy. *Front. Physiol.* 4, 381.

Torriani, M., Townsend, E., Thomas, B.J., Bredella, M.A., Ghomi, R.H., and Tseng, B.S. (2012). Lower leg muscle involvement in Duchenne muscular dystrophy: an MR imaging and spectroscopy study. *Skeletal Radiol.* 41, 437–445.

Tosch, V., Rohde, H.M., Tronchère, H., Zanoteli, E., Monroy, N., Kretz, C., Dondaine, N., Payrastre, B., Mandel, J.-L., and Laporte, J. (2006). A novel PtdIns3P and PtdIns (3, 5) P2 phosphatase with an inactivating variant in centronuclear myopathy. *Hum. Mol. Genet.* 15, 3098–3106.

Tosetti, M., Linsalata, S., Battini, R., Volpi, L., Cini, C., Presciutti, O., Muntoni, F., Cioni, G., and Siciliano, G. (2011). Muscle metabolic alterations assessed by 31-phosphorus magnetic resonance spectroscopy in mild becker muscular dystrophy. *Muscle Nerve* 44, 816–818.

Trinity, J.D., Layec, G., and Lee, J.F. (2014). Heterogeneity of blood flow: impact of age on muscle specific tissue perfusion during exercise. *J. Physiol.* 592, 1729–1730.

Tubridy, N., Fontaine, B., and Eymard, B. (2001). Congenital myopathies and congenital muscular dystrophies. *Curr. Opin. Neurol.* 14, 575–582.

Vainzof, M., Ayub-Guerrieri, D., Onofre, P.C., Martins, P.C., Lopes, V.F., Zilberztajn, D., Maia, L.S., Sell, K., and Yamamoto, L.U. (2008). Animal models for genetic neuromuscular diseases. *J. Mol. Neurosci.* 34, 241–248.

Vainzof, M., Almeida, C.F., Ishiba, R., Martins-Bach, A.B., Santos, A.L.F., and Nogueira, L. Using electroporation as a model of degeneration/regeneration to investigate the regenerative potential in neuromuscular disorders (NMD). (Abstract 2871T). Presented at the 64th Annual Meeting of The American Society of Human Genetics, October 21, 2014 in San Diego, CA.

Valentine, B.A., Winand, N.J., Pradhan, D., Moise, N., de Lahunta, A., Kornegay, J.N., and Cooper, B.J. (1992). Canine X-linked muscular dystrophy as an animal model of Duchenne muscular dystrophy: A review. *Am. J. Med. Genet.* 42, 352–356.

Verhaert, D., Richards, K., Rafael-Fortney, J.A., and Raman, S.V. (2011). Cardiac Involvement in Patients With Muscular Dystrophies Magnetic Resonance Imaging Phenotype and Genotypic Considerations. *Circ. Cardiovasc. Imaging* 4, 67–76.

Vidal, G.D., Wary, C., Giacomini, E., Emmanuel, F., and Carlier, P.G. (2002). A truly non-invasive set-up study of perfusion and energy metabolism in the rat calf in vivo: application to a model of peripheral arterial disease. *MAGMA* 15, 25.

De Visser, M., and Verbeeten, B. (1985). Computed tomography of the skeletal musculature in Becker-type muscular dystrophy and benign infantile spinal muscular atrophy. *Muscle Nerve* 8, 435–444.

- Vlak, M., van der Kooi, E., and Angelini, C. (2000). Correlation of clinical function and muscle CT scan images in limb-girdle muscular dystrophy. *Neurol. Sci.* *21*, S975–S977.
- Voisin, V., Sébrié, C., Matecki, S., Yu, H., Gillet, B., Ramonatxo, M., Israël, M., and De la Porte, S. (2005). l-arginine improves dystrophic phenotype in *mdx* mice. *Neurobiol. Dis.* *20*, 123–130.
- Walter, G., Cordier, L., Bloy, D., and Lee Sweeney, H. (2005). Noninvasive monitoring of gene correction in dystrophic muscle. *Magn. Reson. Med.* *54*, 1369–1376.
- Wang, J., Fan, Z., Vandenborne, K., Walter, G., Shiloh-Malawsky, Y., An, H., Kornegay, J.N., and Styner, M.A. (2013). Statistical texture analysis based MRI quantification of Duchenne muscular dystrophy in a canine model. In *SPIE Medical Imaging*, (International Society for Optics and Photonics), p. 86720F – 86720F.
- Wary, C., Jouvion, G., Baligand, C., and Carlier, P.G. (2011). Improved set-up for fully non-invasive electrostimulation in assessment of muscle perfusion and energy metabolism in mice using multiparametric functional NMR (poster). Presented at Myology 2011, 4th International Congress of Myology, May 9-13, 2011, in Lille, France.
- Wattjes, M.P., Kley, R.A., and Fischer, D. (2010). Neuromuscular imaging in inherited muscle diseases. *Eur. Radiol.* *20*, 2447–2460.
- Weber, H., Rauch, A., Adamski, S., Chakravarthy, K., Kulkarni, A., Dogdas, B., Bendtsen, C., Kath, G., Alves, S.E., Wilkinson, H.A., et al. (2012). Automated rodent in situ muscle contraction assay and myofiber organization analysis in sarcopenia animal models. *J. Appl. Physiol.* *112*, 2087–2098.
- Weber, M.-A., Nagel, A.M., Jurkat-Rott, K., and Lehmann-Horn, F. (2011). Sodium (²³Na) MRI detects elevated muscular sodium concentration in Duchenne muscular dystrophy. *Neurology* *77*, 2017–2024.
- Wehling, M., Spencer, M.J., and Tidball, J.G. (2001). A nitric oxide synthase transgene ameliorates muscular dystrophy in *mdx* mice. *J. Cell Biol.* *155*, 123–131.
- Wei, B., Lu, Y., and Jin, J.-P. (2014). Deficiency of slow skeletal muscle troponin T causes atrophy of type I slow fibres and decreases tolerance to fatigue. *J. Physiol.* *592*, 1367–1380.
- Willcocks, R.J., Arpan, I.A., Forbes, S.C., Lott, D.J., Senesac, C.R., Senesac, E., Deol, J., Triplett, W.T., Baligand, C., Daniels, M.J., et al. (2014). Longitudinal measurements of MRI-T₂ in boys with Duchenne muscular dystrophy: Effects of age and disease progression. *Neuromuscul. Disord.* *24*, 393–401.

Wilmshurst, J.M., Lillis, S., Zhou, H., Pillay, K., Henderson, H., Kress, W., Müller, C.R., Ndong, A., Cloke, V., Cullup, T., et al. (2010). RYR1 mutations are a common cause of congenital myopathies with central nuclei. *Ann. Neurol.* *68*, 717–726.

Winand, N., Pradham, D., Cooper, B. (1994). Molecular characterization of severe Duchenne-type muscular dystrophy in a family of rottweiler dogs. In: *Molecular mechanisms of neuromuscular disease*. Tucson: Muscular Dystrophy Association; 1994.

Wren, T.A., Bluml, S., Tseng-Ong, L., and Gilsanz, V. (2008). Three-point technique of fat quantification of muscle tissue as a marker of disease progression in Duchenne muscular dystrophy: preliminary study. *Am. J. Roentgenol.* *190*, W8–W12.

Yamamoto, D.L., Vitiello, C., Zhang, J., Gokhin, D.S., Castaldi, A., Coulis, G., Piasek, F., Filomena, M.C., Eggenhuizen, P.J., Kunderfranco, P., et al. (2013). The nebulin SH3 domain is dispensable for normal skeletal muscle structure but is required for effective active load bearing in mouse. *J. Cell Sci.* *126*, 5477–5489.

Yemisci, M., Gursay-Ozdemir, Y., Vural, A., Can, A., Topalkara, K., and Dalkara, T. (2009). Pericyte contraction induced by oxidative-nitrative stress impairs capillary reflow despite successful opening of an occluded cerebral artery. *Nat. Med.* *15*, 1031–1037.

Yokota, T., Lu, Q., Partridge, T., Kobayashi, M., Nakamura, A., Takeda, S., and Hoffman, E. (2009). Efficacy of systemic morpholino exon-skipping in duchenne dystrophy dogs. *Ann. Neurol.* *65*, 667–676.

Zvaritch, E., Kraeva, N., Bombardier, E., McCloy, R.A., Depreux, F., Holmyard, D., Kraev, A., Seidman, C.E., Seidman, J.G., Tupling, A.R., et al. (2009). Ca²⁺ dysregulation in Ryr1I4895T/wt mice causes congenital myopathy with progressive formation of minicores, cores, and nemaline rods. *Proc. Natl. Acad. Sci.* *106*, 21813–21818.